Skeletal muscles generate bioelectromagnetic fields that contain information about the neural control of motions and the function of the muscle. One distinguishes between electromyography (EMG), the measurement of the muscle-induced electric potential field, and magnetomyography (MMG), the recording of muscle-induced magnetic fields. EMG is a well-established methodology, and its limitations have been extensively discussed in the scientific literature. In contrast, MMG is an emerging methodology with the potential to overcome some of the inherent limitations of EMG. To unlock the full potential of MMG, it is essential to support empirical observations from experiments with a solid theoretical understanding of muscle-induced bioelectromagnetic fields. Therefore, this thesis derives a novel multiscale skeletal muscle model that can predict realistic EMG and MMG signals. This model is used to conduct the first systematic comparison between surface EMG and non-invasive MMG. By using simulations, all system parameters can be controlled precisely. This would not be possible experimentally. The fundamental properties of EMG and MMG are systematically explored using simulations comparable to electrically or reflex-evoked contractions. Notably, it is shown that non-invasive MMG data is spatially more selective than comparable high-density EMG data. This property, for example, is advantageous for decomposing signals of voluntary contractions into individual motor unit spike trains. Using a novel *in silico* trial framework, it is demonstrated that non-invasive MMG-based motor unit decomposition is superior to the well-established surface EMG-based motor unit decomposition.

ISBN 978-3-946412-11-3

CBM-12 (2023)

T. Klotz

EMG and MMG to Study Motions: Theoretical Background

Bioelectromagnetic Fields for Studying Neuromuscular Physiology: In Silico Investigations of EMG and MMG

Thomas Klotz

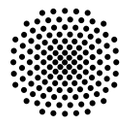

vorgelegt an der

Universität Stuttgart

Bioelectromagnetic Fields for Studying Neuromuscular Physiology: In-Silico Investigations of EMG and MMG

Von der Fakultät Bau- und Umweltingenieurwissenschaften
der Universität Stuttgart zur Erlangung der Würde
eines Doktor-Ingenieurs (Dr.-Ing.)
genehmigte Abhandlung

von

MSc. Thomas Klotz

aus

Schwäbisch Hall

Hauptberichter: Prof. Oliver Röhrle, PhD
Mitberichter: Prof. Francesco Negro, PhD
Tag der mündlichen Prüfung: 21. 04. 2023

Institut für Modellierung und Simulation Biomechanischer Systeme
der Universität Stuttgart

2023

Report No.: CBM-12 (2023)
Institute for Modelling and Simulation of Biomechanical Systems
Chair of Continuum Biomechanics and Mechanobiology
University of Stuttgart, Germany, 2023

Editor:
Prof. O. Röhrle, PhD

ISBN 978-3-946412-11-3

Acknowledgements

The presented work was conducted between 2016 and 2023 as an assistant researcher at the University of Stuttgart within the Research Group in Continuum Biomechanics and Mechanobiology. Many people contributed to this work in different ways. I am grateful for being surrounded by many incredible people and for every contribution to this work.

First, I would like to thank Professor Oliver Röhrle, who gave me the opportunity to do the presented research in his research group. This opened the door to explore the fascinating world of neuromuscular physiology. I am particularly grateful for Oliver's guidance, support and the freedom to follow my ideas throughout my whole time in his research group.

I am grateful to Professor Francesco Negro for making the effort to be a co-chair of the promotion examination. Moreover, I appreciated the shared research projects with Francesco; it was fun how he always pushed us to go one step further. Our work on the decomposition of EMG and MMG gave me new insights into neuromuscular physiology and bio-signal analysis.

Moreover, I want to thank all of my actual and former colleagues in the CBM research group. All of you were important in creating a fun and constructive working environment. I enjoyed the scientific discussions and diverse group activities, from spontaneous after-work drinks to hut trips in the Alps. In particular, I am incredibly grateful for the mentorship of Thomas Heidlauf. He guided me through my first research projects in a fun and constructive atmosphere. One of the frequent discussions with my officemate, Christian Bleiler, culminated in developing the multi-domain model presented in this thesis. I am thankful for all his input on homogenisation and continuum mechanics. Moreover, I want to thank Leonardo Gizzi for sharing all his knowledge on EMG and physiology. This was essential for the verification of the proposed multi-domain model. The motor unit decomposition *in silico* trial framework presented in the last chapter of this monograph was developed in cooperation with my former colleague Lena Lehman. Her excellent work is part of this thesis, and her contribution is greatly acknowledged.

Advancing the understanding of the neuromuscular system requires exploring various research directions. In addition to the tiny scientific contribution presented in this thesis, I enjoy being involved in other exciting research projects. Particularly, I am grateful for the close collaborations with Laura Schmid, Jeroen Jeneson, Jana Disch and Justus Marquetand. I would also like to thank all my students who have conducted various cool research projects. Working with such talented people has always been a great experience.

Ultimately, I thank my family, especially my parents, Rüdiger and Dorothea, and all my siblings, Christina, Ann-Kathrin, Rike, Karen, and Andreas. It is a privilege to have a solid base to which you can come as you are and are always welcome. Moreover, I want to thank all my friends. It was also essential for the success of this work to temporarily escape the scientific world and explore the world from other perspectives in such great company.

Stuttgart, October 2023 Thomas Klotz

Deutsche Zusammenfassung

Die große Variabilität der menschlichen Bewegung erfordert ein koordiniertes Zusammenspiel von Nervensystem und Bewegungsapparat. Bis heute gibt es jedoch nur ein grobes Verständnis der physiologischen Prozesse die zu Bewegungen führen. Dies ist auch darauf zurückzuführen, dass nur wenige geeignete experimentelle Messmethoden existieren, um am lebenden Menschen die Funktionsweise des neuromuskulären Systems zu erforschen. Das Fehlen solcher Technologien erschwert zudem die Erforschung und Beurteilung von Behandlungsmethoden von neuromuskulären Erkrankungen. Folglich ist es notwendig die Entwicklung von nichtinvasiven Methoden zur Untersuchung des neuromuskulären Systems am lebenden Menschen voranzutreiben.

Die Ansteuerung von Skelettmuskeln erfolgt über elektrische Signale, welche als Muskelaktionspotentiale bezeichnet werden. Ein Aktionspotential beschreibt eine charakteristische, zeitlich kurze Abweichung des Membranpotentials. Folglich erzeugen Muskelaktionspotentiale bioelektromagnetische Felder, deren Messung Rückschlüsse auf die neuronale Ansteuerung der Muskulatur sowie auf das elektrophysiologische Verhalten des Muskels zulässt. Dabei kann zwischen Elektromyografie (EMG), d.h. der Messung des vom Muskel erzeugten elektrischen Potentialfeldes, und Magnetomyografie (MMG), d.h. der Messung des vom Muskel generierten Magnetfeldes, unterschieden werden.

In der Vergangenheit wurde jedoch fast ausschließlich die EMG zur Beobachtung der elektrophysiologischen Muskelaktivität verwendet. Bei der Messung von EMG-Signalen können entweder invasive Nadelelektroden oder nichtinvasive Oberflächenelektroden genutzt werden. Die Unterschiede beider Methoden ergeben sich hauptsächlich durch den Abstand zwischen den aktiven Muskelfasern und der Messelektrode sowie den elektrischen Eigenschaften des Körpers. Nadel-EMG erlaubt räumlich hoch sensitive Messungen, die hauptsächlich die Aktionspotentiale der Muskelfasern in unmittelbarer Nähe der Elektrode wieder spiegeln. Daher sind die zugehörigen Messdaten in der Regel relativ leicht zu interpretieren. Durch den schmerzhaften und invasiven Eingriff lassen sich jedoch ausschließlich kooperative Patienten oder Probanden untersuchen. Zudem besteht die Gefahr, dass die gewonnenen Erkenntnisse durch lokale Effekte verfälscht werden. Oberflächen-EMG unterscheidet sich hauptsächlich durch den größeren Abstand zwischen den aktiven Muskelfasern und den Messelektroden. Dies lässt sich durch einen Tiefpassfilter beschreiben, wodurch die räumliche Sensitivität der Messungen abnimmt, d.h. das Oberflächen-EMG bietet einen globaleren Blick auf die elektrophysiologische Aktivität des Muskels. Jedoch ist die Interpretation des Oberflächen-EMG schwieriger. Dies ist insbesondere darauf zurückzuführen, dass die exakten Eigenschaften des Tiefpassfilters von üblicherweise unbekannten Körpereigenschaften abhängen und Untersuchungsergebnisse infolgedessen erheblichen Unsicherheiten aufweisen können.

Die MMG wurde erstmals in den 1970er Jahren beschrieben. Jedoch haben technische Einschränkungen den Einsatz der MMG bisher großteils verhindert. Dabei ist insbesondere zu berücksichtigen, dass das vom Muskel erzeugt Magnetfeld um mehrere Größenordnungen kleiner ist als das Erdmagnetfeld. Daher erfordert die MMG hoch empfindliche Magnetfeldsensoren und eine gezielte Abschirmung oder Unterdrückung des elektromagnetisches Hintergrundrauschen.

Nichtsdestotrotz existieren eine Reihe physikalischer Überlegungen, welche die Aufzeichnung von MMG-Signalen als Alternative zur EMG motivieren. Insbesondere ist hervorzuheben, dass sich Magnetfelder im menschlichen Körper wie im Vakuum ausbreiten können. Daher lassen sich MMG-Signale kontaktfrei messen, was beispielsweise die Anwendung im klinischen Alltag erleichtert, oder stabile Langzeitmessungen über implantierte MMG Sensoren ermöglicht. In den letzten Jahren konnten die technischen Einschränkungen von Magnetometern soweit gelöst werden, dass es jetzt möglich ist die Nutzung von MMG-Messungen in biomedizinischen Anwendungen zu erforschen. Dabei müssen empirischen Beobachtungen, d.h. aus Experimenten, durch ein fundiertes theoretisches Verständnis von EMG-Signalen und MMG-Signalen unterstützt werden.

Das übergeordnete Ziel dieser Arbeit ist es daher eine Simulationsumgebung zu schaffen, die es erlaubt vom Muskel generierte bioelektromagnetischer Felder systematisch zu untersuchen. Da bei Experimenten am lebenden Menschen viele relevante Einflussfaktoren nicht exakt kontrollierbar sind, erlauben mathematischen Modelle Studien die sonst nur schwierig umsetzbar wären. Mathematische Modelle sind eine wichtige Säule der Naturwissenschaften und Simulationen haben in der Vergangenheit schon einen wichtigen Beitrag zum Verständnis von EMG-Signalen geleistet. Jedoch sind Modelle zur Berechnung von MMG-Signalen noch kaum verbreitet und die wenigen existierenden Simulationsmethoden haben signifikante Einschränkungen. Daher wird in dieser Arbeit ein neuartiges Skelettmuskelmodell hergeleitet, dass in der Lage ist muskelinduzierte bioelektomagnetische Felder zu simulieren. Die relevante Zeitskala der vom Muskel erzeugten bioelektromagnetischen Feldern liegt in der Größenordnung von Millisekunden. Daher können für die Modellierung die Näherungen der Elektrostatik und der Magnetostatik benutzt werden. Folglich ist es möglich zunächst die elektrischen Potentialfelder im Muskel zu berechnen und in einem zweiten Schritt das vom Muskel erzeugte Magnetfeld zu bestimmen. Die Beschreibung des elektrischen Verhaltens des Muskels beruht auf einem Mehrskalenmodellierungsansatz, d.h. ein etabliertes (mikroskopisches) Modell zur Beschreibung der elektrischen Ströme in den Muskelfasermembranen wird in ein makroskpoisches Kontinuumsmodell integriert. Die verschiedenen Längenskalen lassen sich dabei unter Berücksichtigung des funktionalen Aufbaus der Skelettmuskulatur konsistent zusammenführen. Um das vom Muskel erzeugte elektrische Potentialfeld im ganzen Körper zu berechnen, kann das hergeleitete Skelettmuskelmodell an ein Volumenleitermodell gekoppelt werden. Basierend auf der Lösung des elektrischen Modells kann nun das (quasi-statische) muskelinduzierte Magnetfeld berechnet werden. Im Bezug auf das Gesamtmodell ist hervorzuheben, dass die simulierten bioelektomagnetischen Felder mechanistisch mit der elektrophysiologischen Funktionsweise des Skelettmuskels verknüpft sind und somit prädiktive Modellvorhersagen möglich sind. Mathematisch repräsentiert das Gesamtmodell ein System gekoppelter Differenzialgleichungen. Jedoch existiert hierfür keine allgemeingültige analytische Lösung. Daher wird in der vorgestellten Arbeit ein Lösungsverfahren hergeleitet, welches es erlaubt die Modellgleichungen numerisch anzunähern. Die Konsistenz des Berechnungsalgorithmus wird durch eine Reihe von Konvergenzstudien nachgewiesen.

Der letzte Teil der vorgestellten Arbeit nutzt die hergeleitete Simulationsumgebung, um zu untersuchen ob die MMG als neue oder alternative elektrophysiologische Untersuchungsmethode eingesetzt werden kann. Dafür werden zunächst einige Simulationen betrachtet die grundlegenden Zusammenhänge zwischen den Vorgängen im Körper und den messbaren EMG-Signalen oder MMG-Signalen herstellen. Elektrisch ooder Reflexinduzierte Muskelkontraktionen erzeugen Summensignale die einfacher zu verstehen sind als Signale von wilkürlichen Kontraktionen. Daher vergleicht diese Arbeit zunächst Summensignale, die entstehen wenn ein

Teil der Muskelfasern stimuliert wird. Dabei kann gezeigt werden, dass sowohl EMG-Signale als auch MMG-Signale von der Anzahl der aktiven Muskelfasern, der räumlichen Anordnung der aktiven Muskelfasern, den Eigenschaften der aktiven Muskelfasern, den elektrischen Eigenschaften des Gewebes sowie der räumlichen Positionierung des Messsystems abhängen. Insbesondere zeigen die Simulationen, dass EMG und MMG komplementäre Signale darstellen. Jedoch zeigt sich dass für die MMG der Informationsgehalt der Signale auf weniger Messkanäle verteilt ist. Folglich ist die nichtinvasive MMG eine attraktive Alternative zur Messung von Oberflächen-EMG. Beispielsweise um genauere Rückschlüsse auf die Vorgänge im Körper ziehen zu können oder um neuartige elektrophysiologische Bildgebungsmethoden zu entwickeln. Eine weiter Vorteil des vorgestellten Computermodells ergibt sich durch die Möglichkeit das messbare Magnetfeld in die Anteile verschiedener elektrischer Ströme zu zerlegen. Dabei kann beispielsweise gezeigt werden, dass die zu den Muskelfasern senkrecht orientierten Magnetfeldkomponenten hauptsächlich auf intrazelluläre Ströme zurückzuführen sind. Außerdem zeigen die Simulationen, dass auch die nicht aktiven Muskelfasern einen relevanten Beitrag zu MMG-Signalen leisten.

Eine wichtige Anwendung der EMG befasst sich mit der Entschlüsselung der neuronalen Ansteuerung der Muskulatur. Jedoch haben entsprechende Methoden zahlreiche Einschränkungen, die oft eng mit den physikalischen Eigenschaften vom EMG-Signalen verknüpft sind. Daher untersucht die vorgestellte Arbeit den Einsatz von MMG um die Steuersignale des Nervensystems zu Entschlüsseln. Dafür werden zunächst die grundlegenden Interferenzmuster von EMG-Signalen und MMG-Signalen vorgestellt und verglichen. Dabei kann gezeigt werden, dass beide Signale durch dasselbe Systemmodell angenähert werden können, d.h. EMG-Signale oder MMG-Signale lasses sich als lineare Überlagerung der von den einzelnen motorischen Einheiten generiert Teilsignalen beschreiben. Daher hängen bioelektromagnetische Felder die bei willentlichen Kontraktionen entstehen, sowohl vom neuronalen Stimulationsmuster als auch von den Muskeleigenschaften selbst ab. Beide Effekte lassen sich jedoch nicht ohne Weiteres trennen. Folglich existiert keine eindeutige Beziehung zwischen der EMG-Amplitude oder MMG-Amplitude und der Stärke des neuronalen Steuersignals. Jedoch ist es möglich ein gemessenes Interferenzsignal in seine Einzelkomponenten zu zerlegen und somit die Aktivität von einzelnen Motoneuronen zu beobachten. Wird dafür jedoch Oberflächen-EMG genutzt beschränken die räumlichen Tiefpassfiltereigenschaften die Anzahl an motorischen Einheiten die zuverlässig extrahiert werden können. In dieser Arbeit wird gezeigt, dass bei nichtinvasiven Messungen die MMG der EMG überlegen ist um verschiedene Quellen, d.h. motorische Einheiten, voneinander zu unterscheiden. Diese Beobachtung macht die MMG zu einer vielversprechenden Methode um die Aktivität einzelner Motoneuronen am lebenden Menschen zu untersuchen. Um das Potential dieses Ansatzes zu testen, wird eine simulationsbasierte Testumgebung vorgestellt. Diese ermöglicht es eine obere Schranke der trennbaren motorischen Einheiten vorherzusagen. Dabei werden die vorgestellten Simulationsmodelle direkt in das Lösungsverfahren existierende Signaltrennmethoden integriert. Hierbei kann gezeigt werden, dass nichtinvasiv gemessene MMG-Signale der Oberflächen-EMG überlegen sind um die Aktivität einzelner Motoneuronen zu entschlüsseln, d.h. die Anzahl der motorischen Einheiten die zuverlässig aus dem Interferenzsignal extrahiert werden kann, erhöht sich annähernd um einen Faktor von zwei. Insbesondere ist es mittels MMG auch möglich das verhalten motorischer Einheiten mit tief liegenden Fasern zu beobachten. Darüber hinaus wird gezeigt, dass die gute Trennbarkeit von MMG-Signalen hauptsächlich darauf zurückzuführen ist, dass ein dreidimensionales Vektorfeld gemessen wird.

Abstract

The impressive variability of human motion requires the coordinated interplay of the nervous system and the musculoskeletal system. However, only a crude understanding of the mechanisms enabling motions exists. A fundamental challenge for investigating the neuromuscular system *in vivo* is the lack of sophisticated experimental methodologies that can measure the performance of muscles and the biophysical function of the body. This shortcoming also limits the development and assessment of therapies to tackle diverse neuromuscular disorders. Hence, novel methods for studying neuromuscular physiology *in vivo* are desperately needed.

Skeletal muscles are the actuators of the body, and their activity is controlled by electric signals, i.e., action potentials. An action potential can be described as the coordinated change of the polarity of an excitable cell's membrane and, thus, causes bioelectromagnetic fields. Hence, measuring muscle-induced bioelectromagnetic fields can provide information on the neural control signals to the muscle and the electrophysiological function of the muscle itself. One distinguishes electromyography (EMG), i.e., measuring the muscle-induced electric potential field, and magnetomyography (MMG), i.e., recording the magnetic field generated by skeletal muscles.

In the past, however, almost exclusively, EMG was used to study neuromuscular physiology. EMG can be recorded invasively via needle electrodes or with non-invasive surface electrodes. The most relevant difference between both signals is determined by the distance between the active muscle fibres and the electrode, as well as the electric properties of the body. In short, needle EMG is spatially highly sensitive and mainly reflects the behaviour of the muscle fibres close to the electrode. Thus, signals obtained from needle EMG recordings are typically easy to interpret. However, the painful and invasive nature of the measurements limits the application of needle EMG to collaborative patients or subjects. Further, the results may be biased by local tissue properties. Due to the increased distance between the electrodes and the sources, surface EMG exhibits a spatial low-pass filtering effect that depends on the body's anatomy and properties. Hence, the signal provides a more global view of the muscle. However, as many relevant properties of the tissues are unknown, the interpretation of surface EMG is challenging, and the results of surface EMG-based studies are often subject to considerable uncertainties.

Although MMG was first described in the 1970s, several (technological) challenges have limited its practical relevance. Most importantly, the amplitude of the magnetic field generated by skeletal muscles is significantly lower than the earth's magnetic field. Hence, MMG requires sensitive magnetic field sensors and shielding or suppression from electromagnetic noise. Nevertheless, a set of physical arguments makes MMG an attractive alternative to well-established EMG recordings. Most importantly, the magnetic permeability of biological tissues is close to the magnetic permeability in free space. Thus, MMG can be measured contact-free, which facilitates, for example, their use in everyday clinical practice or enables stable long-term measurements using implanted MMG sensors. In recent years, the technical limitations of magnetometers have been solved to such an extent that it is now possible to explore the use of MMG signals in biomedical applications. Therefore, supporting empirical observations from experiments with a solid theoretical understanding of bioelectromagnetic fields generated by skeletal muscles is essential.

Hence, this thesis aims to establish a simulation framework enabling systematic investigations of muscle-induced bioelectromagnetic fields. Since many relevant factors affecting muscle-induced bioelectromagnetic fields cannot be precisely controlled during *in vivo* experiments, mathematical models allow investigations that would otherwise be difficult to implement. In the past, simulations have made relevant contributions to understanding EMG signals. However, models for predicting MMG signals are still rare, and the few existing methods have significant limitations for simulating the magnetic fields induced by whole muscles. Therefore, after introducing the basics of neuromuscular physiology and the fundamentals for modelling bioelectromagnetic fields, this thesis derives a novel multiscale bioelectromagnetic skeletal muscle model. The characteristic time scale of muscle-induced bioelectromagnetic fields is in the range of milliseconds. Accordingly, the modelling framework uses the quasi-static approximation of Maxwell's equations. This assumption allows us to decouple the electric and magnetic field equations. Hence, for describing the electric potential fields in the muscle, the proposed simulation framework consistently integrates a (microscale) description of the electric behaviour of the muscle fibre membranes, i.e., the source of EMG and MMG, as well as the most important (microscale and mesoscale) structural features of skeletal muscle tissue into a multiphase macroscopic continuum model. This multi-domain model of skeletal muscle tissue can be coupled to a volume conductor model describing electrically inactive tissues surrounding the muscle. Having solved the electric field problem, we know the current distribution in the body. Within the limits of the quasi-static approximation, this fully determines the muscle-induced magnetic field. Notably, the multiscale approach links the well-studied microscopic behaviour of the muscle fibres to the macroscopic bioelectromagnetic fields and allows for predictive simulations. The overall mathematical model yields a set of coupled differential equations which cannot be solved analytically. Hence, a staggered numerical solution scheme for approximating the model equations is derived in this work. A set of convergence studies demonstrates the consistency of the computational model.

Using EMG or MMG for *in vivo* investigations of the neuromuscular system requires a mechanistic understanding of the relation between the spatiotemporal patterns of the bioelectromagnetic fields and the biophysical state of the body. Electrically or reflex-evoked muscle contractions generate compound muscle responses that are easier to understand than signals from voluntary contractions. Yet, even for artificially evoked contractions, it is not possible to control all system parameters. Hence, to study the fundamentals of muscle-induced bioelectromagnetic fields, this work compares simulated EMG and MMG compound muscle responses in fusiform skeletal muscles. In summary, both EMG and MMG depend on the number of active muscle fibres, the spatial configuration of the recruited muscle fibres, the properties of the muscle fibres, the electric properties of the tissues, and the spatial position of the detection system. Notably, it is shown that EMG and MMG are complementary signals with many common characteristics. Yet, it is shown that compared with surface EMG, the sparsity of non-invasive MMG is less affected by the body's properties and anatomy. This property is beneficial for applications such as the reconstruction of bioelectric sources. Moreover, the *in silico* environment also allows us to predict the contribution of currents in different structural components of the muscle to the MMG signal. For example, the simulations demonstrate that the MMG's normal-to-the-surface component strongly reflects currents inside the muscle fibres. Further, it is shown that the non-recruited muscle fibres considerably contribute to MMG signals.

Finally, this work investigates the use of muscle-induced bioelectromagnetic fields for decoding the voluntary neural drive to the muscle. First, it is demonstrated that – just as EMG signals

– MMG exhibits both positive and destructive interference. In detail, muscle-induced bioelectromagnetic fields can be described as the (linear) superposition of the motor unit responses, i.e., the EMG or MMG signal generated by the activity of an individual motor unit, convoluted by the discharge times of the motor neurons. Hence, EMG and MMG signals observed during voluntary contractions depend on the neural stimulation pattern and the muscle's properties. Both effects cannot be separated straightforwardly. Accordingly, it is well reported that no univocal relation exists between the EMG amplitude and the strength of the neural drive to the muscle. Hence, the current gold standard for decoding the neural drive to a muscle is to decompose interference EMG signals into the spike rains of individual motor units. However, when recording non-invasive surface EMG, the spatial low-pass filtering of the observable signals limits the number of reliably decomposable motor units. This work shows that motor units are more uniquely represented in non-invasively measured high-density MMG data than in comparable high-density surface EMG data. This property of the magnetic field generated by a skeletal muscle motivates us to consider non-invasive MMG-based motor unit decomposition as an alternative to surface EMG-based motor unit decompositions. Hence, this work introduces an *in silico* trial framework for predicting upper-bound accuracy estimates of motor unit decompositions. In short, the *in silico* trial platform integrates the presented EMG and MMG models into state-of-the-art (blind source separation-based) motor unit decomposition methods. Thereby, it is demonstrated that non-invasive MMG-based motor unit decomposition is superior over the well-established surface EMG-based motor unit decomposition, i.e., the number of motor units that can be reliably decomposed nearly increases by a factor of two. Notably, MMG exhibits a less pronounced bias for detecting superficial motor units. Further, it is demonstrated that the most relevant feature explaining the MMG's superior separability is that it represents a three-dimensional vector field.

Contents

1 Introduction

1.1 Motivation, Clinical Relevance and Impact

Motions are a defining feature of human life, i.e., allowing us to perform various tasks, actively interact with the outside world and enable essential bodily functions such as breathing. Therefore, the human body consists of more than 600 skeletal muscles controlled by the nervous system. The amazing variability of human motion relies on the coordinated interplay of the nervous and musculoskeletal systems. Yet, despite more than a century of scientific efforts, only a crude understanding of the mechanisms enabling motions has been established. This is further manifested by the fact that the pathophysiology of various and typically complex neuromuscular disorders – ranging from motor neuron diseases, peripheral neuropathies, muscular dystrophies, multiple types of myopathies, metabolic disorders to diseases affecting the neuromuscular junctions – is often only partially understood. Importantly, this also limits the development of efficient treatment strategies. A fundamental challenge for studying the neuromuscular system *in vivo* is the lack of sophisticated experimental methodologies that can measure the performance of muscles and the biophysical function of the body. For example, motion capture systems allow the study of the kinematics of the body. However, they provide limited insights on the mechanisms involved in performing the motion [e.g., 4, 54, 156, 266]. Imaging techniques, for example, magnetic resonance imaging or ultrasound, allow the study of the morphology of muscles but can only incompletely assess the quality of the tissue [e.g., 102, 146, 173, 209]. Electromyography (EMG), i.e., recorded via needle electrodes or non-invasively from the skin, contains information on the neural drive to the muscle as well as the state of the muscle itself [e.g., 45, 175]. However, needle EMG has limitations due to its invasive nature and surface EMG recordings are associated with high levels of uncertainty caused by the unknown properties of the body. Hence, novel non-invasive techniques for obtaining an integrated view of neuromuscular physiology are desperately needed.

1.2 State-of-the-Art and Objectives

Excitable cells use electric signals, i.e., action potentials, to communicate with other cells or to activate other physiological processes [136]. The most prominent examples of tissues or organs consisting of excitable cells are the brain, the heart and skeletal muscles. An action potential can be described as the coordinated change of a membrane's polarity and thus causes both a time-dependent electric field and a magnetic field. The measurement of bioelectromagnetic fields induced by excitable cells can, therefore, be used to gain insights about the function of the body [163]. Hence, different types of bioelectromagnetic field measurements have been developed for specific tissues and organs [e.g., 45, 77, 175, 183, 198, 247, 249]. For example, the electrocardiogram (ECG) is routinely used to monitor the heart's function. Further, the electroencephalogram (EEG) and the magnetoencephalogram (MEG) are well-established as neuro-imaging techniques for obtaining a (spatial) mapping of brain activity. In skeletal muscle, action potentials control the active contractile behaviour of the muscle fibres [160]. Hence, the activity of skeletal muscles can be measured via electromyography (EMG), i.e., recording the electric potential field caused by the muscle fibre action potentials, or magnetomyography

(MMG), i.e., measuring the magnetic field induced by the muscle fibre action potentials. Both signals contain information on the neural drive to the muscle and the state of the muscle itself and can, therefore, be used to gain insights into the neuromuscular system.

Historically, almost exclusively, EMG has been used to study neuromuscular physiology [cf. e.g., 45, 175]. EMG can be either recorded by utilising invasive needle electrodes [174] or via non-invasive surface electrodes [70]. The most relevant difference between both measurement techniques is the modulation of the signals caused by the distance between the EMG electrode and the sources, as well as the electric properties of the body. In short, needle EMG dominantly records the electric potential field caused by the muscle fibres close to the electrode. This minimises the effect of the electric tissue properties, making signals obtained from needle EMG recordings relatively easy to interpret. For example, individual motor unit action potentials and, hence, the activity of single motor units can often be identified visually [e.g., 1, 34, 50]. Further, needle EMG allows the detection of different classes of pathological spontaneous muscle activity representing hallmarks of neuromuscular diseases. For example, fibrillation potentials, i.e., caused by the involuntary activity of isolated muscle fibres, are associated with muscle denervation, or repeated muscle fibre action potentials that wax and wane in amplitude, as well as frequency, are caused by myotonic disorders, i.e., the delayed relaxation of muscles. Due to these properties, needle EMG represents a well-established clinical diagnostic tool [e.g., 26, 43, 226]. However, the invasiveness of the measurements limits the applicability of needle EMG to collaborative patients or subjects. For example, examining children or conducting longitudinal studies is often difficult. In contrast, surface EMG exhibits a spatial low-pass filter effect due to the increased distance between the electrodes and the sources, which depends on the anatomy and the property of the body [e.g., 66, 159, 219]. Accordingly, surface EMG has a higher detection volume and provides a more global view of muscle activity. However, due to the unknown tissue properties and the spatial location of the bioelectrical sources, the correlation between surface EMG signals and the function of the neuromuscular system is usually associated with a high level of uncertainty. Hence, surface EMG measurements often fail to provide sufficient reliability for biomedical applications. Yet, in the last decade, the combination of high-density surface EMG [11, 177], i.e., utilising dense arrays of electrodes, and sophisticated blind source separation methods have proven to be a valuable methodology to observe the behaviour of individual motor units non-invasively and *in vivo* [e.g., 30, 70, 124, 192, 194].

Although MMG was first described by Cohen & Givler in 1972, several challenges still exist that limit its practical use. Most importantly, the amplitude of the magnetic field induced by skeletal muscles is very low, i.e., in the range of nano-Tesla to pico-Tesla, and thus, significantly lower than the earth's magnetic field. This yields high technical demands for MMG recording systems [270], for example, regarding the sensitivity, the detection range, the sampling rate, the shielding from magnetic noise, the size and portability of the sensor device as well as the cost of such measurements. Nevertheless, several physical considerations regarding the properties of muscle-induced bioelectromagnetic fields motivate the development and investigation of the MMG methodology. Most importantly, the magnetic permeability of biological tissues is close to the magnetic permeability in free space [163, 206]. Thus, compared to surface EMG, MMG is expected to show a higher spatial selectivity. Further, unlike EMG, MMG recordings do not rely on sensor-tissue contacts. This facilitates measurements in everyday clinical practice and increases the reliability of longitudinal studies. Moreover, this means MMG sensors can be encapsulated to guarantee biocompatibility with the body. MMG is therefore appealing for long-term (invasive) measurements, such as prosthesis control via implanted

sensors. Recently, advances in sensor technology [e.g., 14, 103, 188, 233, 270] has enabled a few proof-of-concept studies illustrating the feasibility of measuring MMG for biomedical applications [e.g., 18, 20, 154, 217]. Consequently, MMG can now be considered a promising, rapidly developing method to study the neuromuscular system *in vivo*.

However, the full potential of MMG has yet to be explored. Therefore, it is particularly relevant to investigate how MMG compares to other methodologies, most importantly EMG. This requires combining empirical observations from experiments with a solid theoretical understanding of muscle-induced bioelectromagnetic fields through mathematical modelling. Hence, this work aims to establish a mechanistic understanding of EMG and MMG signals by performing *in silico* experiments. This includes:

- Investigation of the influence of the tissue properties and the detection system on EMG or MMG signals.
- The first detailed comparison of compound muscle responses, i.e., characterising signals from electrically or reflex-evoked contractions.
- Predicting the relevance of intracellular and extracellular currents to the measurable magnetic field.
- Examining the basic properties of interference signals observable during voluntary contractions.
- Testing the potential use of MMG for performing non-invasive motor unit decompositions.

Maxwell's equations are the universal basis for describing electromagnetic fields. Modelling bioelectromagnetic fields induced by the human body requires suitable constitutive assumptions. For the simulation of EMG signals, skeletal muscle tissue is typically considered a volume conductor, i.e., describing the extracellular space, interacting with a source (volume) current field [cf. e.g., 179, 242], i.e., representing the transmembrane currents associated with the muscle fibre action potentials. Depending on the complexity of the tissue geometry, the applied boundary conditions, the muscle architecture and spatial heterogeneities, volume conductor models can be either solved analytically [e.g., 68, 178] or need to be approximated numerically [e.g., 58, 72, 158, 159, 181, 185]. Volume conductor EMG models have, for example, been used to study the relation between the tissue properties and the signal shape [58, 158, 159], to investigate the influence of the detection system [66, 68], to assist the interpretation of experimental data [57, 176, 219] or to examine the influence of motion [181, 185]. The accuracy of volume conductor models depends on the precise estimation of electric tissue properties and the description of the source current field. Currently, it is extremely challenging to perform subject-specific EMG simulations.

Modelling predictions of MMG signals are still rare. All models that aim to predict the muscle-induced magnetic field have in common that they assume quasi-static conditions, i.e., decoupling of the electric and magnetic fields. Hence, one can first calculate the current field in the body, which fully determines the magnetic field. For example, in [20], a finite wire model, i.e., describing the current field in the muscle fibres, was used for explaining the MMG signal triggered by an electrical stimulus of the motor nerve. However, this model could only partially explain the observed data. This is most likely because volume currents in the extracellular space are neglected. Further, in [270, 272] a full-field continuum model, i.e., the muscle fibres and the extracellular connective tissue are modelled as spatially separated region [cf. 264], was used to predict both the electric potential field and the magnetic field in a small muscle tissue sample.

However, the computational demands of this approach limit its usability for simulating bioelectromagnetic fields of whole muscles. Hence, performing *in silico* investigations of EMG and MMG requires new modelling frameworks. Since knowledge about MMG and experimental data is sparse, simulations must have high predictive capabilities. Thus, this work aims

- to introduce a multiscale model of muscle-induced bioelectromagnetic fields,
- identify suitable model parameters enabling reliable *in silico* predictions,
- derive a numerical solution scheme for solving the proposed equations.

1.3 Outline of This Thesis

This thesis aims to establish the theoretical basis for using bioelectromagnetic fields in biomedical applications. This is achieved by performing *in silico* investigations of EMG and MMG signals. Therefore, the presented work is structured as follows:

Part I introduces the fundamental basics for modelling muscle-induced bioelectromagnetic fields. Performing predictive EMG and MMG simulations requires solid knowledge of the underlying physiological processes. Hence, Chapter 2 briefly introduces the anatomy and physiology of the neuromuscular system. Representing the source of bioelectromagnetic fields, a particular focus is dedicated to the function of excitable cells. Further, to guarantee consistency with the laws of physics, the basics of electromagnetism are presented in Chapter 3. Finally, Chapter 4 provides an overview of existing mathematical models currently used for modelling the behaviour of excitable cells and bioelectromagnetic fields.

Part II describes a novel modelling framework for simulating EMG and MMG signals. Therefore, in Chapter 5, a multiscale model consistently integrating a microscopic description of the transmembrane currents in the muscle fibres as well as the functional organisation of skeletal muscles in motor units into a macroscopic continuum model is derived. This so-called multi-domain model is coupled to a model of electrically inactive tissues surrounding the muscle. Further, suitable boundary conditions, as well as model parameters, are introduced. The overall mathematical model can only be solved numerically. Hence, in Chapter 6, a staggered solution scheme for approximating the model equations is introduced. The consistency of the resulting computational model is shown by conducting a set of convergence studies.

Part III comprises specific *in silico* experiments for obtaining theoretical insights on muscle-induced bioelectromagnetic fields that would currently not be easily feasible using experiments. First, in Chapter 7, the fundamental properties of EMG and MMG are examined by simulating compound muscle responses. That is the EMG or MMG signals caused by the synchronous activity of multiple muscle fibres, which is comparable to signals from artificially evoked contractions (e.g., electric stimulation or reflex pathways). In particular, it is demonstrated how the spatiotemporal patterns of EMG and MMG signals relate to a skeletal muscle's properties. Hence, the presented results represent the theoretical basis for interpreting EMG and MMG signals within specific biomedical applications. Chapter 8 investigates EMG and MMG of voluntary contractions. A particular focus is dedicated to methods estimating the neural control of muscles. First, the fundamental interference patterns of EMG and MMG signals are examined, followed by a discussion of the associated challenges. The current gold standard for non-invasively decoding the voluntary drive to the muscle is the decomposition of high-density surface EMG signals into the spike trains of individual motor units. However, the electric tissue

properties typically limit the number of motor unit sources that can be reliably identified. Hence, this work investigates the potential of using non-invasive high-density MMG recordings for observing individual motor units *in vivo*. This is achieved by introducing a novel *in silico* trial framework for predicting upper bound accuracy estimates of motor unit decompositions. The performance of MMG-based motor unit decompositions is compared to the performance of EMG-based motor unit decompositions.

Finally, Chapter 9 concludes the presented work by discussing the limitations of the presented results, contextualising the proposed methods and providing an outlook on further applications of EMG and MMG. Thereby, a particular focus is dedicated to the need for mathematical modelling.

Part I

Basics for Modelling Muscle-Induced Bioelectromagnetic Fields

2 Anatomy and Physiology of the Neuromuscular System

This chapter introduces the anatomical and physiological basics for modelling muscle-induced bioelectromagnetic fields. With the overall scope of this work in mind, only a short and incomplete overview is provided. Numerous specialised textbooks exist to get deeply into the fascinating world of the neuromuscular system. For example, the textbook of Kandel, Schwartz, Jessell, Siegelbaum, Hudspeth, Mack et al. [136] provides an excellent overview of the structure and function of the nervous system. The physiology of skeletal muscles is extensively described in the textbook of MacIntosh, Gardiner & McComas [160]. Further, the works of Heckman & Enoka [100, 101] focus on the tightly coupled functional organisation of the nervous system and skeletal muscles.

2.1 Neuromuscular Physiology in a Nutshell

Skeletal muscles allow the central nervous system to interact with the outside world. Hence, one considers all the muscles in the body and the nerves serving them as one physiological system, i.e., the neuromuscular system. The smallest functional unit of the neuromuscular system is the motor unit. A motor unit consists of a motor neuron and all the muscle fibres it innervates. The fact that a muscle consists of up to several hundreds of motor units allows a fine modulation of a muscle's force output, enabling the great variability of human motions. Motor neurons are the ultimate control elements of the neuromuscular system. Therefore, the motor neurons integrate signals from the brain, i.e., where motions are planned and initiated, as well as sensory pathways that provide feedback on the state of the body. Once a motor neuron reaches its depolarization threshold, an action potential is triggered (see Section 2.2.2) and travels along the axon towards the neuromuscular junctions of the associated muscle fibres. Each stimulus arriving at a neuromuscular junction causes an action potential that spreads along the entire length of the muscle fibre. The muscle fibre action potential controls cellular force production (see Section 2.3.2). The overall muscle force is the sum of the contributions of the individual motor units. The latter depends on the frequency of the motor neuron discharges, the number of muscle fibres per motor unit and the properties of the muscle fibres (see Section 2.3.3). Ultimately, the active muscle force is transmitted to the skeleton via tendons. Since skeletal muscles can only contract actively, the coordinated interplay between agonistic and antagonistic muscles is required to control the movement of whole joints. A schematic illustration of the basic physiological processes involved in the generation of motion is shown in Figure 2.1.

2.2 Excitable Cells

The nervous system encodes information through a temporal series of impulses. Biophysically, each impulse corresponds to an action potential. Action potentials are characterised by a rapid rise, i.e., known as depolarisation, and fall, i.e., known as repolarisation, of a cell's membrane potential [117], cf. Figure 2.2. Cells generating action potentials are called excitable cells, such

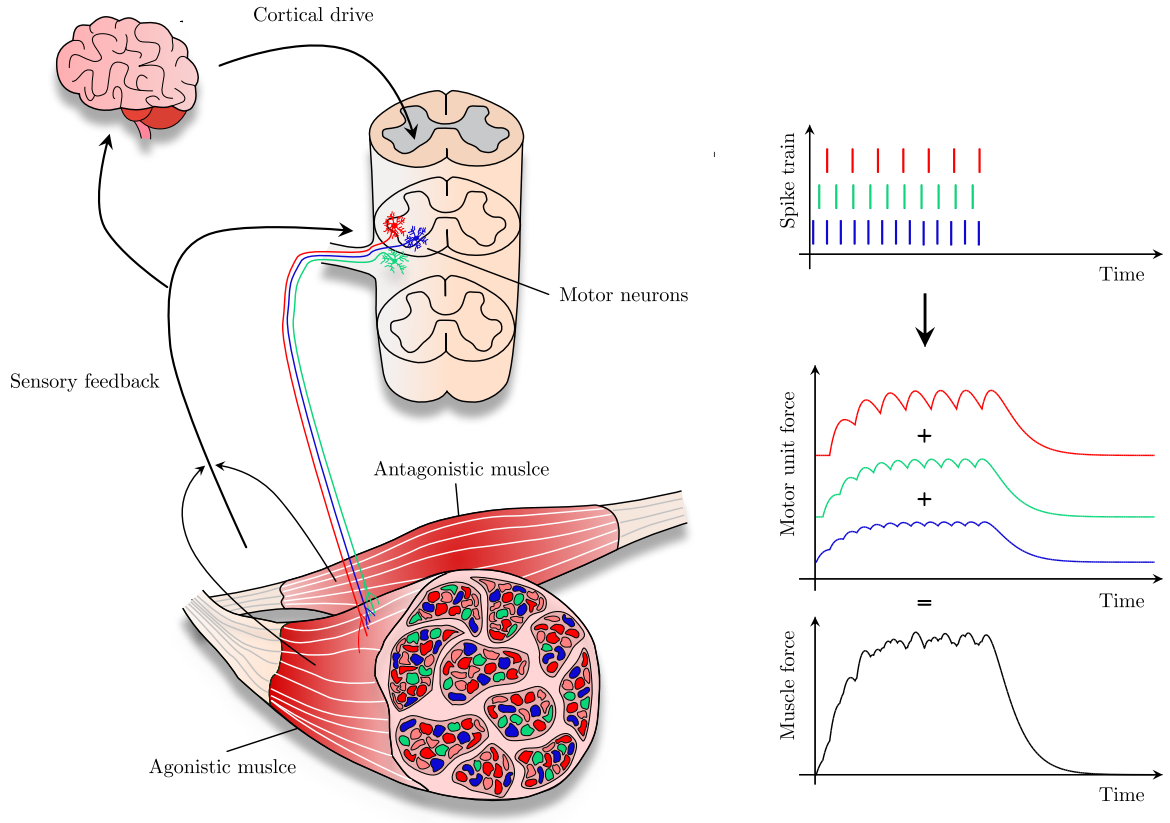

Figure 2.1: Left: Schematic drawing showing the basic physiological pathway of motion. The colours (blue, green and red) indicate different motor units. Right: Exemplary illustration of how neural stimuli are translated into a muscle's mechanical force output.

as nerve and muscle cells. The membranes of all excitable cells share the same basic structure and function [121, 216]. Given the scope of this work, a skeletal muscle fibre is used as a representative example to explain the structure and function of the membrane of an excitable cell. Notably, these fundamental principles are equally valid for other excitable cells.

2.2.1 The Structure of the Muscle Fibre Membrane

The function of an excitable cell's membrane is closely linked to its structure [3, 136, 251]. Phospholipid molecules are the main components of the cell membrane. The phospholipids are organised as a lipid double layer. Thereby, the hydrophilic heads create the inner and outer surface of the membrane, and the hydrophobic tails form the inner part. Further, the lipid double layer is approximately 10 nm thick and nearly impermeable for dissolved molecules. Hence, the cell membrane is a boundary between the intracellular environment, i.e., the cytoplasm, and the extracellular fluid. In this way, a specific electrolyte solution can be maintained inside the cell, which may differ considerably from the biochemical composition of the extracellular fluid. At the same time, highly specialised protein complexes are embedded in the membrane, forming transport systems, for example, for ions, signalling molecules or metabolites. For the function of excitable cells, the exchange of ions between the cytoplasm and the extracellular environment is essential. Therefore, ion-specific channels can be opened and closed, for example, driven by the membrane potential. Ion channels enable the (passive) flux of ions driven by the electrochemical gradient of the ionic species [e.g., 8, 115]. Further, active pumps allow the transport of ions

against their electrochemical gradient by the cost of energy, which is typically provided by the hydrolysis of ATP (adenosine triphosphate) [e.g., 85, 239]. The most prominent example is the sodium-potassium pump, which transports sodium from the cell in exchange for potassium ions.

2.2.2 The Function of the Muscle Fibre Membrane

The rapid time course of an action potential requires the resting cell to keep the membrane in an electrically polarised state (see Figure 2.2A). That is, the concentration of ions – most importantly sodium and potassium – is different in the cytoplasm and the extracellular fluid. In detail, the extracellular sodium concentration is one magnitude higher than the intracellular sodium concentration. Further, the concentration of potassium ions is one magnitude higher inside the cell than in the extracellular space. Hence, the resting potential is typically in the range of $-70\,\mathrm{mV}$ to $-80\,\mathrm{mV}$. External stimuli can modulate the membrane potential. In detail, an excitatory stimulus will depolarise the transmembrane potential, while an inhibitory stimulus will hyperpolarise the membrane potential. If the membrane potential reaches a depolarisation threshold, i.e., approximately $-55\,\mathrm{mV}$, voltage-gated sodium channels [265] open and cause a strong sodium influx into the cell, cf. Figure 2.2B. This yields the rapid depolarisation of the membrane potential. The increase of the transmembrane potential also activates voltage-dependent potassium channels [161], causing a potassium flux from the cell into the extracellular space, cf. Figure 2.2C. Initially, the sodium current dominates the potassium current, and the transmembrane potential is further depolarised. Once the transmembrane potential reaches its peak value, the sodium channels close while the potassium channels remain open. This behaviour causes the transmembrane potential to return to its resting potential (see Figure 2.2D). Hence, the action potential is an all-or-nothing event. After returning to the resting potential, the sodium channels remain inactivated for several milliseconds. This causes a refractory period, during which triggering a new action potential is impossible. Notably, only a few ions must flow across the membrane to considerably change the membrane potential. Hence, hundreds of action potentials can be generated without the immediate need for restoring the concentration gradient through the sodium-potassium pump.

Action potentials can be triggered locally on each membrane patch. A reaction-diffusion process achieves the spatial propagation of action potentials within the cell (see Figure 2.3). If the membrane potential is depolarised at one point of a membrane, the electric potential gradient causes electric currents. The diffusion of ions towards their electric equilibrium state yields a depolarisation of the membrane potential on neighbouring membrane patches. The action potential is regenerated locally if the membrane potential reaches the depolarization threshold. Notably, the axons of some neurons are surrounded by an insulating molecule named myelin. The latter increases the distance over which an action potential can be propagated without the need to be regenerated. Hence, myelinated axons show higher conduction velocities [e.g., 262].

2.2.3 Communication Between Excitable Cells

Cell-to-cell communication is based on functional structures known as synapses. While there exist several specialised forms of synaptic transmission [e.g., 40, 60, 189], synapses are typically classified into two basic forms, i.e., electric synapses and chemical synapses. The latter is particularly relevant for the physiology of the neuromuscular system. Thus, only the function of chemical synapses is introduced briefly within this work. Chemical synapses enable the unidirectional transmission of information, i.e., from a presynaptic neuron to a postsynaptic cell. In short, when an action potential reaches the (axon) terminal in the pre-synaptic cell,

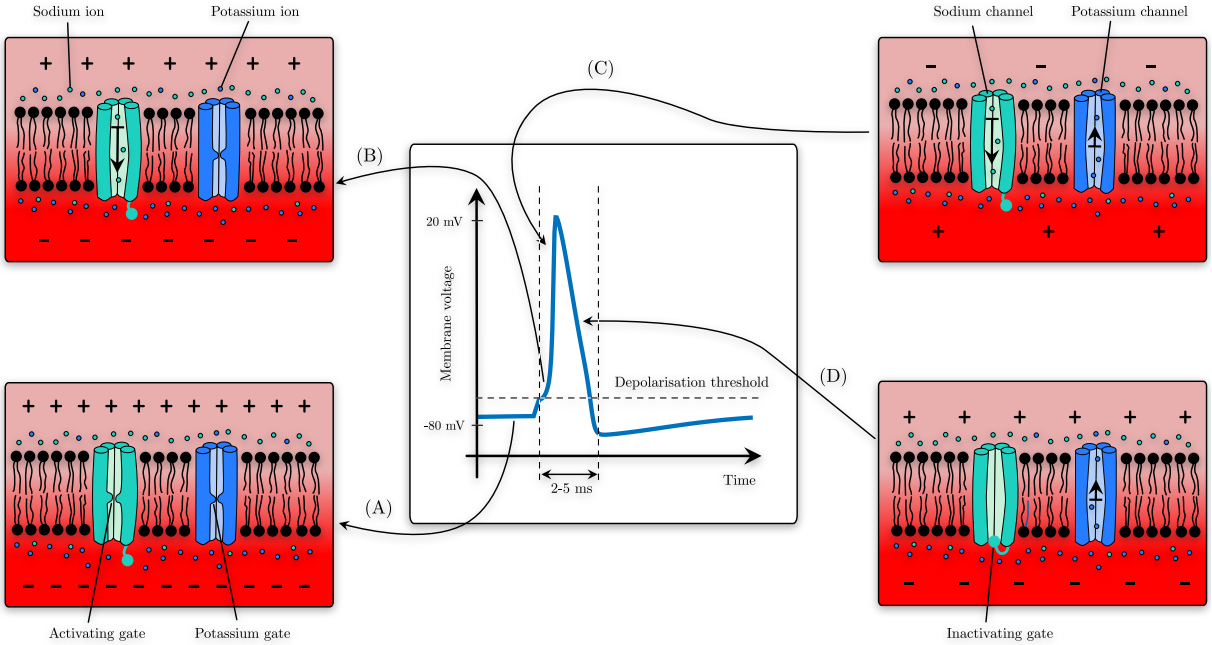

Figure 2.2: Schematic illustration of the function of an excitable cell's membrane: (A) In the resting state, the membrane is polarised and nearly impermeable to ions. (B) If an excitatory stimulus reaches the depolarization threshold, voltage-gated sodium channels open and cause a strong sodium influx into the cell. (C) The shift in the membrane potential successively activates voltage-gated potassium channels, causing a potassium current outside the cell. (D) The sodium channel's inactivating gate closes when the membrane voltage reaches its maximum value. This causes the membrane potential to return to its resting potential. Note that the inactivating gate of the sodium channels remains closed for a few milliseconds after the membrane potential has returned to its resting value, causing a refractory period.

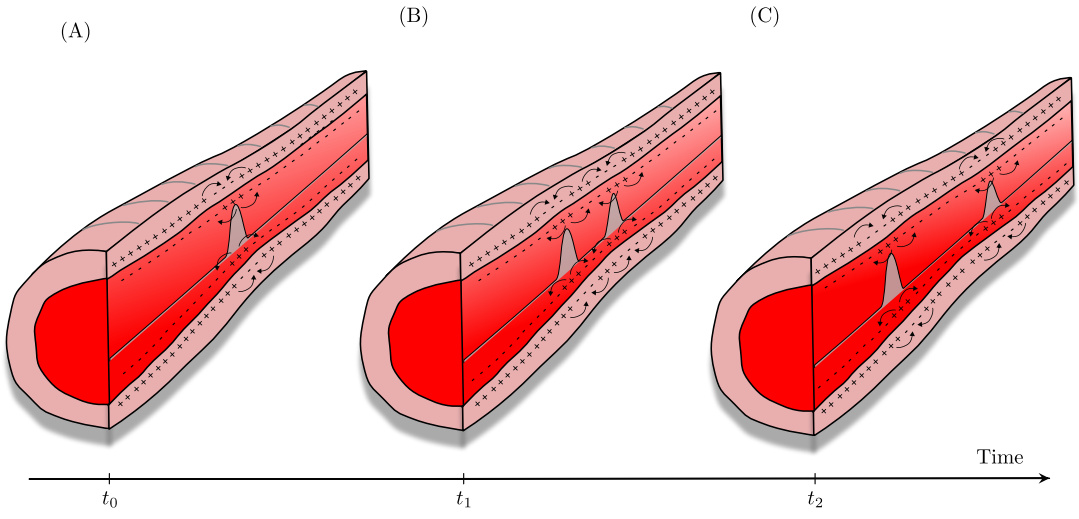

Figure 2.3: Schematic drawing illustrating how an action potential is propagated along a muscle fibre. (A) The local depolarisation of the membrane potential at t_0 causes a potential gradient and, hence, electric currents, i.e., illustrated by the arrows. (B) and (C): The induced currents trigger action potentials on neighbouring sites of the muscle fibre membrane. Hence, the action potential is propagated through a reaction-diffusion process.

neurotransmitters, e.g., acetylcholine or different amino acids, are released via synaptic vesicles and transported through synaptic cleft towards the membrane of the post-synaptic cell. The membrane of the postsynaptic cell contains specialised receptor channels. In the presence of a neurotransmitter, the receptor channels open and modulate the ionic permeability of the postsynaptic membrane. Depending on the equilibrium potential of the ionic species that can pass through the receptor channel, an excitatory postsynaptic potential or an inhibitory postsynaptic potential is generated. The postsynaptic potentials generated by all synapses are summed up. This allows the post-synaptic cell to integrate different inputs.

The neuromuscular junction (see Figure 2.4) is a specific synapse linking the motor neurons and the muscle fibres [41, 135]. Once the motor neuron's axon reaches its target muscle, it is split into nerve branches. These nerve endings contain the presynaptic terminals, which form connections to the motor end plates, i.e., the post-synaptic parts of the associated muscle fibres. At the neuromuscular junction, acetylcholine is used as a neurotransmitter binding to nicotinic receptors at the motor end plate. This opens sodium channels in the muscle fibre membrane and, thus, depolarises the transmembrane potential. Notably, the neuromuscular junction is a strong synapse. Thus, in a healthy neuromuscular system, each presynaptic action potential in the motor axon triggers a post-synaptic action potential in the connected muscle fibre.

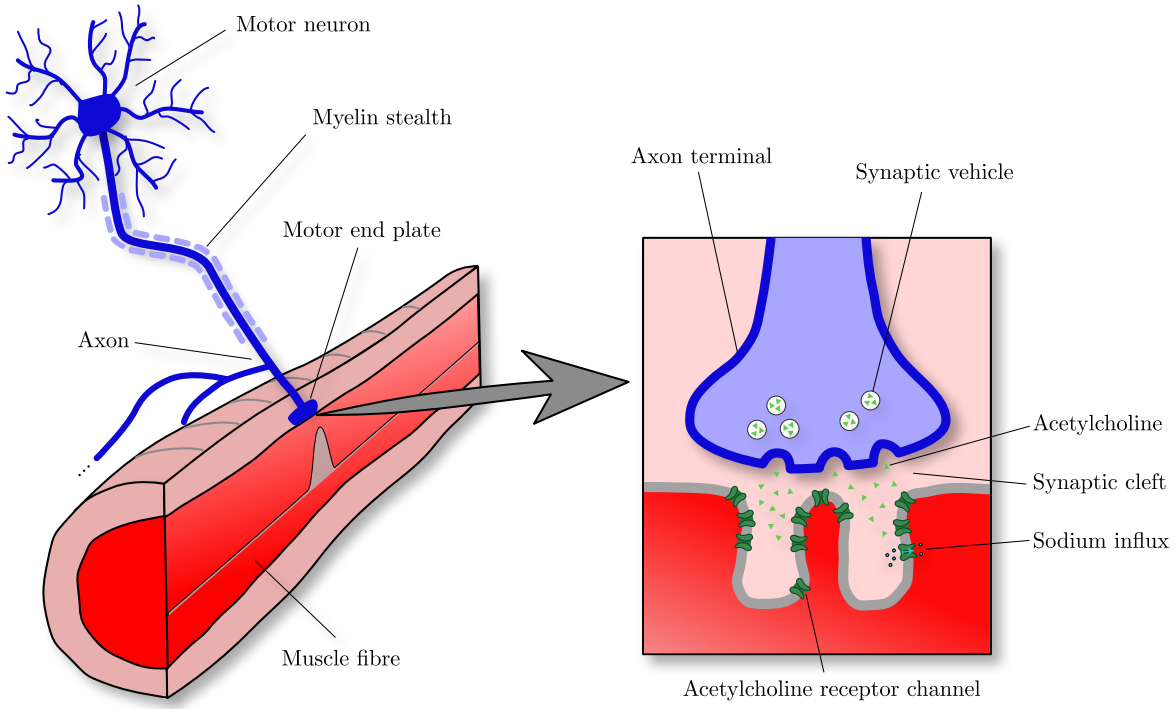

Figure 2.4: Schematic drawing of the neuromuscular junction as an example of a chemical synapse.

2.3 Skeletal Muscles

Muscles are the actuators of the human body. Thereby, one distinguishes cardiac muscles, smooth muscles and skeletal muscles. Skeletal muscles enable voluntary motions and translate the commands of the central nervous system into mechanical work. This section provides a brief overview of the structure and function of skeletal muscles.

2.3.1 The Anatomy of Skeletal Muscles

The most striking property of a skeletal muscle is its ability to contract actively. Muscle contraction relies on a complex interplay of cellular processes, which are closely related to the structure of a skeletal muscle. That is, skeletal muscle tissue is hierarchically organised, cf. Figure 2.5, mainly consisting of muscle fibres, i.e., the muscle cells, and extracellular connective tissue. The connective tissue dominantly consists of collagen. Forming direct connections to the muscle fibres, the connective tissue is the structural scaffold of the muscle. Further, the connective tissue subdivides the muscle into muscle fibre bundles called fascicles. Besides providing mechanical support [e.g., 128, 184, 244], the extracellular connective tissue is important for embedding other structures and cells into the muscle, for example, nerves and blood vessels.

The muscle fibres themselves are long, cylindrically shaped, multi-nucleated cells. The most dominant structures in a muscle fibre are the myofibrils. Myofibrils are arranged in parallel and comprise thousands of sarcomeres, i.e., the basic contractile unit of the muscle fibre. Sarcomeres are constructed by a periodic lattice of thin actin and thick myosin filaments that can slide relatively to each other without changing their length [99, 133]. Further, the actin filaments are connected to the myosin filaments via a giant protein named titin [165, 166, 260]. The sarcolemma surrounds the muscle fibre, i.e., a lipid double layer showing all properties of an excitable cell's membrane (cf. Section 2.2) and a basement membrane, for example, providing mechanical support. One specific feature of the muscle fibre membrane is that it includes a channel-like network known as T-tubules. The T-tubules penetrate towards the

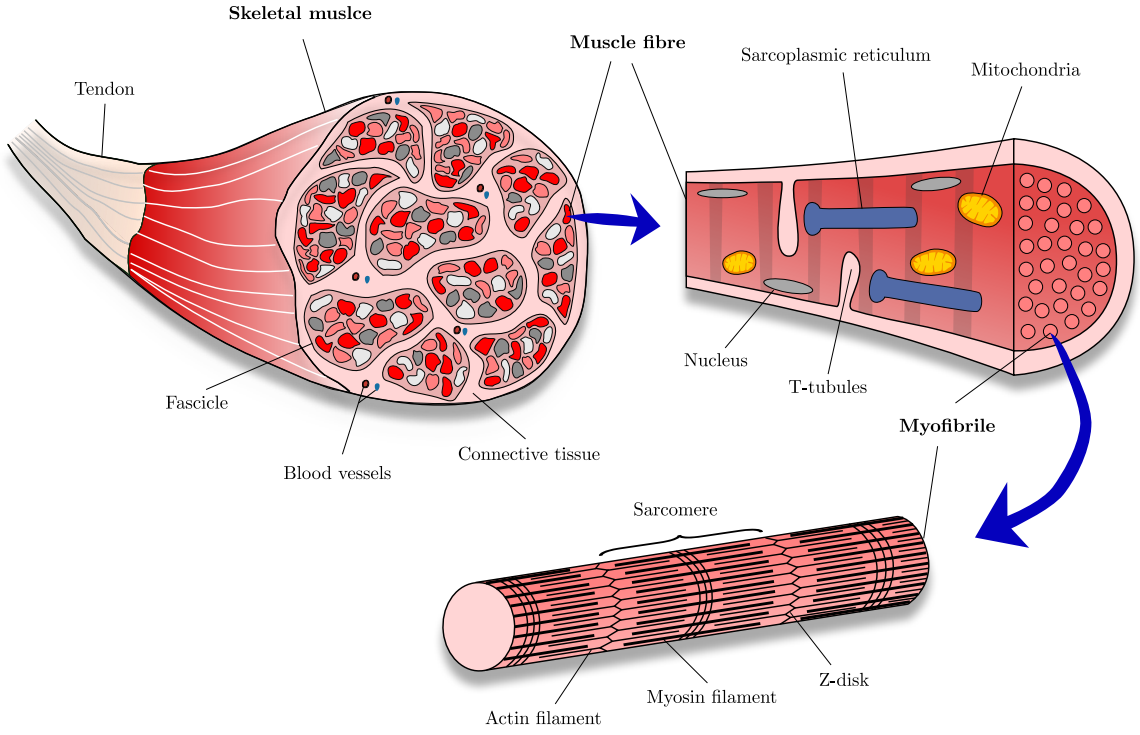

Figure 2.5: Schematic drawing of the basic architecture of a skeletal muscle.

centre of the muscle fibres and are essential for transmitting the stimulus delivered by the action potential to the whole cell. The muscle cell includes another tubular structure known as the sarcoplasmic reticulum, which serves as calcium storage for intracellular signalling [e.g., 224]. Further, a network of mitochondria enables oxidative ATP synthesis within the muscle fibre [88].

Skeletal muscles do exist in different sizes and shapes [e.g., 150]. The human body has skeletal muscles with only a few hundred fibres and muscles with more than a million fibres. Further, skeletal muscles are often classified based on their primary facile direction. The most prominent example is the class of fusiform skeletal muscles, where the fibres span from tendon to tendon, i.e., longitudinally to the muscle's line of action. For pinnated muscles, the fibres are obliquely arranged concerning the muscle's line of action. One further distinguishes uni-pinnated and multi-pinnated muscles, i.e., where the pinnation angle is variable within different muscle compartments. Internally, pinnated muscles include tendinous structures named aponeurosis, which are essential for transmitting the active stresses generated by the individual muscle fibres. Pinnation maximizes muscle force for a given volume [151].

2.3.2 The Function of a Muscle Fibre

The active contractile behaviour of muscle fibres can be explained by the sliding filament theory pioneered by the works of Huxley & Hanson [132] and Huxley & Niedergerke [131] as well as the cross-bridge theory proposed by Huxley [130]. In summary, in the presence of calcium ions, the catalytic domain of the myosin heads can bind to specialised binding sites on the thin filament. The resulting bound, which consists of a myosin head and an actin-binding site, is denoted as a cross-bridge. A conformational change, which myosin heads can undergo, represents the molecular motor's working stroke. Depending on the mechanical constraints, the working stroke yields a relative motion between the thin and the thick filaments, i.e., muscle contraction, or an elongation of the myosin heads' molecular spring, i.e., active force. After the working stroke, the cross-bridge can detach from the thin filament and return to its initial state. The repeated process of attachment, working stroke and detachment is known as the cross-bridge cycle. Through cross-bridge cycling, skeletal muscles convert chemically stored energy into mechanical work. The mechanical stress a muscle fibre generates depends on the contraction velocity [114] and the length of the muscle [92]. While the classical two-filament model captures many features of active force generation, it should be noted that further cellular structures are crucial for the physiological function of muscle tissue. For example, the identification of an additional myofilament named titin [165, 166, 260] within the sarcomeres of skeletal muscles advanced the understanding of the active contractile behaviour of the fibres [112].

In normal conditions, putting muscle fibres into action requires an external stimulus. When a muscle fibre is stimulated at its neuromuscular junction, an action potential is triggered and propagated towards the end of the muscle fibre (cf. Section 2.2.2). The action potential is conducted along the muscle fibre and transmitted towards the centre of the fibre via the T-tubules system. Within the T-tubules, the depolarisation of the membrane potential stimulates voltage-sensitive dihydropyridine receptors (DHPR). The DHRP sensor is a voltage-gated calcium channel and allosterically activates the ryanodine receptor (RyR1) of the sarcoplasmic reticulum [218]. Ryanodine receptors are calcium channels, and due to the concentration gradient of calcium ions between the sarcoplasmic reticulum and the cytoplasm, the action potential triggers the fast release of calcium ions into the cytoplasm. In the cytoplasm, calcium ions serve as a second messenger system, controlling the active mechanical behaviour of a muscle fibre. The Sarcoplasmic/Endoplasmic Reticulum Calcium ATPase (SERCA) is an

antagonistic system pumping calcium ions from the cytoplasm to the sarcoplasmic reticulum to remove the contractile stimulus.

Two proteins are particularly relevant for linking the intracellular calcium signalling system to the active mechanical behaviour of a muscle fibre [cf. e.g., 91]: troponin and tropomyosin. Both molecules are linked to the actin filament. In short, troponin has calcium binding sites controlling its conformation. Further, the tropomyosin filaments span the entire length of the actin filaments and, in the resting state, block the binding sites for the myosin heads on the thin filaments. Tropomyosin and troponin are mechanically linked. Hence, the conformational change of the troponin molecule moves the tropomyosin filaments, which uncovers the binding sites of the thin filaments. This enables cross-bridge cycling and, hence, muscle contraction. The whole physiological pathway from the action potential to the mechanical response of a muscle fibre is known as excitation-contraction coupling [232]. The fact that an electric stimulus directly controls the mechanical muscle output is the basis for using bioelectromagnetic fields to study a muscle's function.

2.3.3 The Motor Unit

A motor neuron and all the fibres it innervates are known as a motor unit. The motor unit is the basic functional unit for controlling voluntary motions. This fundamental physiological concept was pioneered by the works of Charles Sherrington [149, 235, 236] at the beginning of the 20th century and further refined in the last 100 years [cf. e.g., 74, 100, 101, 127]. Typically, each muscle is innervated by hundreds of motor neurons, forming a motor neuron pool. The somas of all motor neurons belonging to the same motor neuron pool are clustered in the spinal cord. The axons of the motor neurons exit the spinal cord through the ventral horn and are the connecting element between the central nervous system and the muscles. Each axon innervates a set of muscle fibres, i.e., a few to several thousand, via a specialised synapse called the neuromuscular junction. Once an action potential reaches the neuromuscular junction, acetylcholine is released as a neurotransmitter and travels through the synaptic cleft to activate the respective muscle fibre. Notably, in the healthy neuromuscular system, the induced post-synaptic potential is always strong enough to trigger an action potential in the muscle fibre [62]. Hence, the fact that a single motor neuron (simultaneously) activates multiple muscle fibres makes a muscle a natural amplifier of a motor neuron activity.

The properties of the motor units are distributed heterogeneously across the motor unit pool. This is essential for the function of the neuromuscular system [24]. First, the motor neurons vary in axon diameter, whereby a motor unit's depolarisation threshold decreases with its size [109]. Further, the attributes of the muscle fibres belonging to the same motor unit are closely linked to the properties of the innervating motor neuron [25, 108]. In detail, the motor neuron with the smallest axon diameter innervates the lowest number of muscle fibres. For all other motor units, the number of innervated fibres increases with the size of the motor neuron. The relation between motor unit size and its fibre load can be approximated with an exponential function. Hence, many small motor units and only a few large ones exist. Further, the ratio between the fibre load of the largest motor unit and the fibre load of the smallest motor unit is typically in the range of 10^2 [64]. Muscle fibres belonging to the same motor unit are distributed within a subset of the muscle cross-section, i.e., referred to as motor unit territory, and are intermingled with muscle fibres from other motor units [12, 22]. Notably, the size and the fibre density of a motor unit territory differs between muscles and subjects. Further, it is noted that small motor units are associated with slowly contracting and fatigue-resistant muscle fibres. In contrast, larger motor units have fibres showing faster contraction times but are more fatigable.

Based on the organisation of the neuromuscular system in motor units, the muscle force can be adjusted by modulating the number of active motor units and the firing frequency of each motor unit [59]. Theoretically, this allows infinite recruitment patterns to achieve the same motion. The dimensionality of the neuromuscular control problem is reduced as the neuromuscular system makes use of the previously described organisation of the motor unit pool [107]. For most conditions, the main parts of the neural drive to the individual motor neurons are shared across the entire motor neuron pool [74] or at least parts of it [127]. Hence, increasing the (common) voluntary drive to a motor neuron pool causes a recruitment order from the smallest motor unit to the largest motor unit. Thereby, the smallest motor neuron shows the highest firing frequency.

3 Electromagnetism

Predictive biological models need to be consistently derived from the fundamental laws of physics. Electromagnetism is the scientific discipline that deals with the electromagnetic force, which describes the interaction between electrically charged particles. Representing the theoretical backbone for simulating bioelectromagnetic fields, a brief overview of electromagnetism is provided in this chapter. The electromagnetic force introduced in Section 3.1 is a fundamental force of physics and responsible for all electromagnetic phenomena. It can be described through electromagnetic fields, which are determined by Maxwell's equations, see Section 3.2. For bioelectromagnetic fields, one can typically assume quasi-static conditions. This simplifies Maxwell's equations, and the resulting electrostatic and magnetostatic approximation is introduced in Section 3.3. Finally, in Section 3.4, the basics for constitutively describing electromagnetic fields in materials are introduced. A more detailed introduction to electromagnetism can, for example, be found in the textbook of Griffiths [93].

3.1 The Electromagnetic Force

The electromagnetic force is responsible for all electromagnetic phenomena. Mathematically, the electromagnetic force can be described by electromagnetic fields, i.e., the electric field $\boldsymbol{E}$ and the magnetic field $\boldsymbol{B}$. Lorentz force law[1] describes the effect of an electric field $\boldsymbol{E}$ and a magnetic field $\boldsymbol{B}$ on a particle with charge q and velocity $\boldsymbol{v}$, i.e.,

$$F \;=\; q\,(\boldsymbol{E} + \boldsymbol{v} \times \boldsymbol{B}) \;. \tag{3.1}$$

Therein, F is the electromagnetic force, which is one of physics's four (currently known) fundamental forces.

3.2 Maxwell's Equations

In classical physics, Maxwell's equations describe the evolution of the electric field and magnetic field. Maxwell's equations[2] were established in the 19th century and unified various experimental observations in a consistent theory. In summary, they state that all electromagnetic fields are ultimately caused by alternating electromagnetic fields, electric charges and electric currents.

3.2.1 Formulation in Terms of the Electric Field and the Magnetic Field

Maxwell's equations can be expressed in various equally valid formulations. In modern literature, the standard notation is often based on the vector calculus formalism introduced by Oliver

[1] The electromagnetic force is also referred to as Lorentz force named after the physicist Hendrik Lorentz. Parts of the force law were already included in earlier works by James Maxwell, which Oliver Heaviside and Hendrik Lorentz further elaborated.

[2] Maxwell's equations are named after the physicist James Maxwell, who proposed between 1861 and 1862 in a groundbreaking series of four articles entitled "On Physical Lines of Force" [168–171] a set of 20 equations, which are capable of explaining all known electromagnetic phenomena.

Heaviside. Thereby, the differential form of Maxwell's equations reads

$$\operatorname{div} \boldsymbol{E} = \frac{\rho}{\varepsilon_0} , \qquad \text{(Gauss's law)} \tag{3.2a}$$

$$\operatorname{div} \boldsymbol{B} = 0 , \qquad \text{(Gauss's law for magnetism)} \tag{3.2b}$$

$$\operatorname{curl} \boldsymbol{E} = -\frac{\partial \boldsymbol{B}}{\partial t} , \qquad \text{(Faraday's law)} \tag{3.2c}$$

$$\operatorname{curl} \boldsymbol{B} = \mu_0 \left(\boldsymbol{j} + \varepsilon_0 \frac{\partial \boldsymbol{E}}{\partial t} \right) . \qquad \text{(Ampère-Maxwell law)} \tag{3.2d}$$

Therein, $\operatorname{div}(\cdot)$ denotes the divergence operator, $\operatorname{curl}(\cdot)$ is the curl operator, ρ is the electric charge density, ε_0 is the vacuum permittivity, μ_0 is the vacuum permeability, and $\boldsymbol{j}$ is the total electric current density. Maxwell's equations, together with Lorentz force law, i.e., Equation (3.1), form the universal basis of electromagnetism. Other important physical relations, such as the conservation of electric charges, directly follow from Maxwell's equations. Hence, a continuity equation describing the local charge density can be derived by applying the div-curl identity, i.e., stating that the divergence of the curl for all vector fields is zero, to the Ampère-Maxwell law:

$$\begin{aligned} & 0 = \operatorname{div}\left[\operatorname{curl} \boldsymbol{B}\right] , \\ \Leftrightarrow \quad & 0 = \operatorname{div}\left[\mu_0 \left(\boldsymbol{j} + \varepsilon_0 \frac{\partial \boldsymbol{E}}{\partial t} \right)\right] , \\ \Leftrightarrow \quad & 0 = \mu_0 \left(\operatorname{div} \boldsymbol{j} + \varepsilon_0 \frac{\partial}{\partial t} \operatorname{div} \boldsymbol{E} \right) , \\ \Leftrightarrow \quad & 0 = \operatorname{div} \boldsymbol{j} + \frac{\partial \rho}{\partial t} . \end{aligned} \tag{3.3}$$

In short, Equation (3.3) states that the density of electric charges within an infinitesimal control volume is related to the flux of electric currents into and outside the control volume. Balance equations are essential to evaluate if a process conforms to the laws of physics. Hence, it is often convenient to use the charge balance as a starting point for describing the electromagnetic behaviour of materials.

3.2.2 Potential Formulation

For many applications, it is useful to express the electric field $\boldsymbol{E}$ and the magnetic field $\boldsymbol{B}$ in terms of a corresponding potential, i.e.,

$$\boldsymbol{E} = -\operatorname{grad} \phi - \frac{\partial \boldsymbol{A}}{\partial t} , \tag{3.4a}$$

$$\boldsymbol{B} = \operatorname{curl} \boldsymbol{A} . \tag{3.4b}$$

Therein, ϕ is the electric (scalar) potential, and $\boldsymbol{A}$ is the magnetic vector potential. Using Equations (3.4a) and (3.4b) Maxwell's equations can be rewritten to yield

$$\operatorname{div}(\operatorname{grad} \phi) + \frac{\partial}{\partial t}\left[\operatorname{div} \boldsymbol{A}\right] = -\frac{\rho}{\varepsilon_0} , \tag{3.5a}$$

$$\left(\operatorname{div}(\operatorname{grad} \boldsymbol{A}) + \frac{1}{\varepsilon_0 \mu_0} \frac{\partial^2 \boldsymbol{A}}{\partial t^2} \right) - \operatorname{grad}\left[\operatorname{div} \boldsymbol{A} + \frac{1}{\varepsilon_0 \mu_0} \frac{\partial^2 \phi}{\partial t^2} \right] = -\mu_0 \boldsymbol{j} . \tag{3.5b}$$

This exchange of variables reduces the number of independent state variables from six to four. Further, the electromagnetic field problem is fully described by only two equations as Gauss's

law for magnetism (3.2b) and Faraday's law (3.2c) reduce to identities.

While the electric field $\boldsymbol{E}$ and the magnetic field $\boldsymbol{B}$ are physical degrees of freedom, i.e., each mathematical degree of freedom has a uniquely quantifiable effect on a test charge (cf. Equation (3.1)), their corresponding potentials are not. This means that the electric field $\boldsymbol{E}$ and the magnetic field $\boldsymbol{B}$ are invariant with respect to the potential transformations

$$\phi' = \phi - \frac{\partial \lambda}{\partial t} \quad \text{and} \tag{3.6a}$$

$$\boldsymbol{A}' = \boldsymbol{A} + \operatorname{grad} \lambda \, . \tag{3.6b}$$

Therein, λ is an arbitrary twice-differentiable function (both in space and time). Hence, obtaining a unique mathematical solution requires the introduction of a gauge. While an infinite number of possible gauge choices exist, this additional degree of freedom can be beneficial to simplify Maxwell's equations further.

3.3 The Electrostatic and the Magnetostatic Approximation

When the electromagnetic fields, the electric charges and the electric currents are stationary, i.e., they do not change with time, electrostatics and magnetostatics provide a simplified framework to study the electric and magnetic fields, respectively. Even when charges and currents change relatively slowly, assuming quasi-static conditions (i.e., for each time frame, the physical quantities are considered stationary) can yield reasonable approximations for time-dependent problems. For bioelectromagnetic fields, the characteristic time scale is typically in the range of milliseconds. Hence, sufficient accuracy can be achieved within the limit of the quasi-static approximation.

3.3.1 Formulation in Terms of the Electric Field and the Magnetic Field

Using the vector calculus formalism, the differential form of the (quasi-)static Maxwell's equations is given by

$$\operatorname{div} \boldsymbol{E} = \frac{\rho}{\varepsilon_0} \, , \qquad \text{(Gauss's law)} \tag{3.7a}$$

$$\operatorname{div} \boldsymbol{B} = 0 \, , \qquad \text{(Gauss's law for magnetism)} \tag{3.7b}$$

$$\operatorname{curl} \boldsymbol{E} = \boldsymbol{0} \, , \qquad \text{(Faraday's law)} \tag{3.7c}$$

$$\operatorname{curl} \boldsymbol{B} = \mu_0 \boldsymbol{j} \, . \qquad \text{(Ampère's law)} \tag{3.7d}$$

Further, the conservation of the electric charges reads (cf. Equation (3.3))

$$\operatorname{div} \boldsymbol{j} = 0 \, . \tag{3.8}$$

Hence, within the limits of the quasi-static approximation, the charge density is locally conserved.

3.3.2 Potential Formulation

For quasi-static conditions the electric (scalar) potential ϕ and the magnetic vector potential $\boldsymbol{A}$ are defined as

$$\boldsymbol{E} = - \operatorname{grad} \phi \, , \tag{3.9a}$$

$$\boldsymbol{B} = \operatorname{curl} \boldsymbol{A} \, . \tag{3.9b}$$

Accordingly, the potential formulation of the quasi-static Maxwell's equations is as follows

$$\operatorname{div}(\operatorname{grad}\phi) \;=\; -\frac{\rho}{\varepsilon_0}\,, \tag{3.9c}$$

$$\operatorname{div}(\operatorname{grad}\boldsymbol{A}) \;-\; \operatorname{grad}\left[\operatorname{div}\boldsymbol{A}\right] \;=\; -\mu_0\,\boldsymbol{j}\,. \tag{3.9d}$$

For quasi-static problems, Coulomb gauge, i.e.,

$$\operatorname{div}\boldsymbol{A} \;=\; 0\,, \tag{3.10}$$

is a popular choice to yield:

$$\operatorname{div}(\operatorname{grad}\phi) \;=\; -\frac{v}{\varepsilon_0}\,, \tag{3.11a}$$

$$\operatorname{div}(\operatorname{grad}\boldsymbol{A}) \;=\; -\mu_0\,\boldsymbol{j}\,. \tag{3.11b}$$

Notably, Equation (3.11a) and Equation (3.11b) are Poisson equations for which various solution schemes exist.

3.4 Electromagnetic Fields in Matter

The previous sections, i.e., Section 3.2 and Section 3.3, showed that all electromagnetic fields are caused by alternating electromagnetic fields, electric charges and electric currents. On the atomic scale, charges and currents are associated with discrete particles, i.e., electrons and protons. Theoretically, it would be possible to solve Maxwell's equations by considering all charged particles and their trajectories. However, for obvious reasons, such an approach becomes quickly impractical. Therefore, on the macroscopic continuum scale, the charge density ρ and the current density $\boldsymbol{j}$ were introduced, representing an idealisation of the discrete nature of real materials. Nevertheless, for modelling materials, it is helpful to consider how those idealised continuum quantities relate to the atomic scale properties of matter. This allows us to reformulate Maxwell's equations in terms of the auxiliary fields, which are typically the basis for describing electromagnetic fields in matter.

3.4.1 The Concept of Free and Bound Charges

Materials can be classified into conductors and dielectrics (in a simplified view, also called insulators). Hence, it turns out useful to additively split up the total charge density into the free charge density ρ_f and the bound charge density ρ_b, i.e.,

$$\rho \;=\; \rho_\mathrm{f} \,+\, \rho_\mathrm{b}\,. \tag{3.12}$$

The free charge density ρ_f corresponds to charged particles that can move freely within a material, for example, electrons in metal crystals or ions in electrolyte solutions. In contrast, the bound charge density ρ_b describes charges attached to a specific atom or molecule. For example, the electrons that spin around an atom's positively charged nucleus. Hence, bound charges can undergo only tiny motions on the atomic scale. In the absence of an external electric field, the configurations of bound charges are uncorrelated. Thus, macroscopically bound charges cancel each other out. However, when a dielectric material is exposed to an external electric field, bound charges can be aligned to yield macroscopic electric dipoles. This effect is known as polarisation.

3.4.2 The Concept Free and Bound Currents

Analogously, the total electric current density $\boldsymbol{j}$ can be split up into the free current density $\boldsymbol{j}_\mathrm{f}$ and the bound current density $\boldsymbol{j}_\mathrm{b}$, i.e.,

$$\boldsymbol{j} \;=\; \boldsymbol{j}_\mathrm{f} + \boldsymbol{j}_\mathrm{b}\,. \tag{3.13}$$

The free current density $\boldsymbol{j}_\mathrm{f}$ corresponds to the net flux of unbounded charged particles and is often called conductive current density. The bound current density $\boldsymbol{j}_\mathrm{b}$ represents the net flux of bound charges on the atomic scale. Bound currents can be caused by the temporal change of the bound charge density, i.e., known as polarisation current density $\boldsymbol{j}_\mathrm{p}$. Further, other tiny currents on the atomic scale exist, for example, caused by electrons spinning around the nucleus of an atom or their axes. In non-magnetic materials, such currents are uncorrelated and cancel each other out. However, such tiny currents on the atomic scale can be aligned in magnetic materials. Macroscopically, this behaviour can be described by the magnetisation current density $\boldsymbol{j}_\mathrm{m}$, which can depend on various factors, for example, the magnetic field, the temperature or the pressure. Accordingly, the bound current density $\boldsymbol{j}_\mathrm{bound}$ is given by

$$\boldsymbol{j}_\mathrm{b} \;=\; \boldsymbol{j}_\mathrm{p} + \boldsymbol{j}_\mathrm{m}\,. \tag{3.14}$$

In summary, modelling electromagnetic fields in matter requires knowledge of the underlying material's conductive, dielectric, and magnetic properties.

3.4.3 Maxwell's Equations in Terms of the Auxiliary Fields

Experimentally, only the free charge density and the free current density can be explicitly controlled. In contrast, the bound charge density and the bound current density depend on the (fixed) material properties. By introducing the auxiliary fields $\boldsymbol{D}$ and $\boldsymbol{H}$ one can reformulate the right-hand side of Maxwell's equations to purely depend on the free charge density and the free current density, i.e.,

$$\operatorname{div}\boldsymbol{D} \;=\; \frac{\rho_\mathrm{f}}{\varepsilon_0}\,, \qquad \text{(Gauss's law)} \tag{3.15a}$$

$$\operatorname{div}\boldsymbol{B} \;=\; 0\,, \qquad \text{(Gauss's law for magnetism)} \tag{3.15b}$$

$$\operatorname{curl}\boldsymbol{E} \;=\; -\frac{\partial \boldsymbol{B}}{\partial t}\,, \qquad \text{(Faraday's law)} \tag{3.15c}$$

$$\operatorname{curl}\boldsymbol{H} \;=\; \mu_0\left(\boldsymbol{j}_\mathrm{f} + \varepsilon_0\frac{\partial \boldsymbol{E}}{\partial t}\right)\,. \qquad \text{(Ampère-Maxwell law)} \tag{3.15d}$$

Therein, the displacement field $\boldsymbol{D}$ is defined as

$$\boldsymbol{D} \;=\; \varepsilon_0\boldsymbol{E} + \boldsymbol{P}\,, \tag{3.16}$$

with $\boldsymbol{P}$ denoting the polarisation field. The latter is related to the bound charge density via

$$\rho_\mathrm{b} \;=\; -\operatorname{div}\boldsymbol{P}\,. \tag{3.17}$$

Further, the magnetic $\boldsymbol{H}$ field is given by

$$\boldsymbol{H} \;=\; \frac{1}{\mu_0}\boldsymbol{B} - \boldsymbol{M}\,, \tag{3.18}$$

where the magnetisation field $\boldsymbol{M}$ is related to the bound current density by

$$\boldsymbol{j}_{\mathrm{b}} \;=\; \operatorname{curl} \boldsymbol{M} \;+\; \frac{\partial \boldsymbol{P}}{\partial t} \;. \tag{3.19}$$

Hence, the auxiliary fields $\boldsymbol{D}$ and $\boldsymbol{M}$ fully describe the influence of bound charges and bound currents. However, this approach comes with the cost that one needs to introduce (phenomenological) constitutive assumptions relating the auxiliary fields to the electric field $\boldsymbol{E}$ and the magnetic field $\boldsymbol{B}$ as well as all other relevant physical quantities. Further, for solving a specific electromagnetic field problem, a constitutive description of the free current density is required. The most prominent choice is Ohm's law, i.e.,

$$\boldsymbol{j}_{\mathrm{f}} \;=\; \boldsymbol{\sigma} \boldsymbol{E} \;, \tag{3.20}$$

where $\boldsymbol{\sigma}$ is the conductivity tensor.

4 Mathematical Models for Simulating Bioelectromagnetic Fields

Mathematical models are essential for obtaining a mechanistic understanding of biological systems or for augmenting experimentally acquired data with state variables that are not directly measurable. This chapter aims to provide an overview of existing mathematical models that are particularly relevant for describing muscle-induced bioelectromagnetic fields. Hence, Section 4.1 considers quantitative methods for describing the electric behaviour of the muscle fibre membrane, i.e., the source of EMG and MMG. Further, in Section 4.2, modelling approaches for simulating bioelectromagnetic fields in the body are described. A general overview of mathematical models for simulating physiological systems can be found, for example, in the textbook of Keener & Sneyd [138]. Further, a more focused description of methods for simulating bioelectromagnetic phenomena is provided in the textbooks of Malmivuo, Plonsey et al. [163] or Plonsey & Barr [212]. A review of models specifically describing skeletal muscles and the neuromuscular system can be found in the work of Röhrle, Yavuz, Klotz, Negro & Heidlauf [222].

4.1 Biophysical Modelling of Excitable Cells

The discovery of the mechanisms responsible for generating action potentials as described in Section 2.2 represents one of the major achievements in computational biology. That is, in 1952 Alan Hodgkin and Andrew Huxley proposed a mathematical model [121] providing a mechanistic explanation of an action potential's generation as well as propagation and earning them the 1963 Nobel Prize in Physiology or Medicine[1]. Their original 1952 paper remains a scientific masterpiece worth reading. As the framework described therein is still the most important theoretical tool for describing the function of an excitable cell's membrane, a summary of their work is provided within this section.

4.1.1 The Electrochemical Gradient

In Section 2.2, it was described that excitable cells make an effort to preserve specialised electrolyte compositions in the intracellular and extracellular environments. This yields for each ionic species an electrochemical potential, i.e., describing both the concentration gradient and the electric gradient across the membrane, which is the driving force for all ionic currents through the channels of an excitable cell's membrane. The electrochemical potential for an ion of species X can be quantified by computing the difference between the transmembrane potential and the ionic species's equilibrium potential. Based on fundamental thermodynamics, the equilibrium potential of an ionic species can be computed by the Nernst equation [196], i.e.,

$$E_{\mathrm{X}} \;=\; \frac{RT}{zF} \ln\left(\frac{[\mathrm{X}]_{\mathrm{o}}}{[\mathrm{X}]_{\mathrm{i}}}\right) \;. \tag{4.1}$$

[1] The Noble Prize was shared in three equal parts between Alan Hodgkin, Andrew Huxley and John Eccles for their discoveries concerning the ionic mechanisms involved in excitation and inhibition in the peripheral and central portions of the nerve cell membrane. Eccles was awarded for his studies showing how nerve pulses are transmitted between cells.

Therein, R is the gas constant, T is the absolute temperature in Kelvin, and F is the Faraday constant. Further, z is the charge of the ionic specie, $[\mathrm{X}]_\mathrm{o}$ is the concentration of the ionic specie outside the cell, and $[\mathrm{X}]_\mathrm{i}$ is the concentration of the ionic specie inside the cell. Hence, if the membrane voltage is smaller than the equilibrium potential, ions from species X will flow from the extracellular space into the cell. Given a membrane voltage larger than the equilibrium potential, ions of specie X will flow outside the cell.

4.1.2 The Hodgkin-Huxley Model

In 1939, Alan Hodgkin and Andrew Huxley measured for the first time an action potential between an intracellular electrode and an extracellular electrode in the squid's giant axon [117]. Their experiment proved that an action potential originates at the membrane level. About the same time Cole & Curtis [39] were capable of showing that the ionic permeability of an excitable cell's membrane changes during the time course of an action potential. To unlock the biophysical mechanisms responsible for generating an action potential, in the late 1940s, Alan Hodgkin and Andrew Huxley, together with Bernard Katz, conducted a series of voltage-clamp experiments on the squid's giant axon [118–120, 122]. Their experiments revealed that in the squid's giant axon – as in many other excitable cells – the transmembrane currents are mainly caused by sodium and potassium ions and a rather small leakage current. Note that the leakage current summarises the effect of additional ionic species, for example, chloride ions. Hence, a patch of the membrane can be represented by an equivalent electrical circuit[2] consisting of a capacitor, i.e., reflecting that the membrane is electrically polarised, in parallel with a sodium channel, a potassium channel and a leakage channel (see Figure 4.1A). Using Kirchhoff's current law, the transmembrane current density is given by

$$I_\mathrm{m} \;=\; C_\mathrm{m}\frac{\partial V_\mathrm{m}}{\partial t} \;+\; I_\mathrm{ion} \;=\; 0\;. \tag{4.2}$$

Therein, C_m is the capacitance-per-unit area of the membrane patch. Further, the overall ionic current across the membrane is additively split up, i.e.,

$$I_\mathrm{ion} \;=\; I_\mathrm{Na} \;+\; I_\mathrm{K} \;+\; I_\mathrm{L}\;, \tag{4.3}$$

where I_Na, I_K and I_L are the sodium current density, the potassium current density and the leakage current density, respectively. From a modern point of view, the ionic currents can be attributed to the lumped behaviour of all ion channels of an ionic species (cf. Section 2.2). However, when the Hodgkin-Huxley model was developed, the membrane structure had yet to be discovered. Nevertheless, Hodgkin and Huxley provided an explanatory hypothesis that the ions cross the membrane through tunnel-like structures. Thereby, the conductive current density through the ion channels is driven by the electrochemical potential of the respective ionic species, i.e.,

$$I_\mathrm{Na} \;=\; g_\mathrm{Na}\,(V_\mathrm{m} - E_\mathrm{Na})\;, \tag{4.4a}$$

$$I_\mathrm{K} \;=\; g_\mathrm{K}\,(V_\mathrm{m} - E_\mathrm{K})\;, \tag{4.4b}$$

$$I_\mathrm{L} \;=\; g_\mathrm{L}\,(V_\mathrm{m} - E_\mathrm{L})\;. \tag{4.4c}$$

[2] The work of Gustav Kirchhoff [139] pioneered electric circuit theory in the middle of the 19th century, even before Maxwell's equations had been established. Nevertheless, electric circuit theory can be considered a consistent simplification of Maxwell's equations that approximately holds in the low-frequency limit. That is, the wavelength of the electromagnetic fields is large compared to the length of the elements in an electric circuit. In particular, Kirchhoff's current law can be considered equivalent to the current balance given in Equation (3.8). Kirchhoff's voltage law is equivalent to Faraday's law, i.e., Equation (3.7c), stating that the electric field is a conservative vector field. Hence, integrating the electric field over an arbitrary closed loop is always zero.

Therein, g_{Na}, g_{K} as well g_{L} describe the conductivity of the membrane for the different ionic species. Further, a positive sign corresponds to an outward current[3].

For modelling an action potential, the key challenge remains to describe the membrane's dynamic and selective ionic permeability. This was possible as Hodgkin and Huxley could separate the sodium and potassium currents induced by step-wise perturbations of the transmembrane potential. Based on this data, Hodgkin and Huxley concluded that the sodium conductance g_{Na} and the potassium conductance g_{K} depend on the time t and the transmembrane potential V_{m}. However, the leakage conductance g_{L} as well as the sodium equilibrium potential E_{Na}, the potassium equilibrium potential E_{K} and the leakage equilibrium potential E_{L} are assumed to be constant. Having observed that the sodium conductance has a fast-activating component and a slower inactivating component, it can be empirically described by a system of differential-algebraic equations, i.e.,

$$g_{\mathrm{Na}} = m^3 h\, \bar{g}_{\mathrm{Na}} \,, \tag{4.5a}$$

$$\frac{\partial m}{\partial t} = \alpha_m (1-m) + \beta_m m \,, \tag{4.5b}$$

$$\frac{\partial h}{\partial t} = \alpha_h (1-h) + \beta_h h \,. \tag{4.5c}$$

Therein $m \in [0,\, 1]$ is the probability of the sodium channel's activating gate to be open, $h \in [0,\, 1]$ is the probability of the sodium channel's inactivating gate to be open and $\bar{g}_{\mathrm{Na}}$ is a constant. Further, the transition rates for the gates to close or open, i.e., α_m, β_m, α_h and β_h, are assumed to depend on the transmembrane potential, i.e.,

$$\alpha_m = \frac{-0.1 \cdot (V_{\mathrm{m}} + 50)}{\exp\left(-\frac{V_{\mathrm{m}}+50}{10} - 1\right)} \,, \tag{4.6a}$$

$$\beta_m = 4 \cdot \exp\left(-\frac{V_{\mathrm{m}} + 75}{18}\right) \,, \tag{4.6b}$$

$$\alpha_h = 0.07 \cdot \exp\left(-\frac{V_{\mathrm{m}} + 75}{20}\right) \,, \tag{4.6c}$$

$$\beta_h = \frac{1}{\exp\left(-\frac{V_{\mathrm{m}}+45}{10} + 1\right)} \,. \tag{4.6d}$$

A similar empirical model is used to describe the potassium conductance dynamics. Contrary to the sodium conductance, the potassium conductance does not show an inactivating component, yielding

$$g_{\mathrm{K}} = n^4\, \bar{g}_{\mathrm{K}} \,, \tag{4.7a}$$

$$\frac{\partial n}{\partial t} = \alpha_n (1-n) + \beta_n n \,. \tag{4.7b}$$

Therein, $n \in [0\,, 1]$ is the probability of the potassium channel's activating gate to be open, and $\bar{g}_{\mathrm{K}}$ is a constant. Further, the transition rates α_n and β_n can be calculated by

$$\alpha_n = \frac{-0.01 \cdot (V_{\mathrm{m}} + 65)}{\exp\left(-\frac{V_{\mathrm{m}}+65}{10} - 1\right)} \,, \tag{4.8a}$$

$$\beta_n = 0.125 \cdot \exp\left(\frac{V_{\mathrm{m}} + 75}{80}\right) \,. \tag{4.8b}$$

[3]Today, the transmembrane potential is defined as $V_{\mathrm{m}} = \phi_{\mathrm{i}} - \phi_{\mathrm{e}}$. Hodgkin and Huxley used the opposite, equally valid definition. Within this work, the modern definition of the transmembrane potential is used. The corresponding transformations of the equations are adopted from the model repository of the physiome project: https://models.physiomeproject.org/workspace/hodgkin_huxley_1952

Note that Hodgkin and Huxley had considered different, equally valid mathematical descriptions for modelling the dynamic behaviour of the membrane conductance. However, without an explicit physical motivation for any formulation, they chose the simplest model that could adequately describe the recorded action potential.

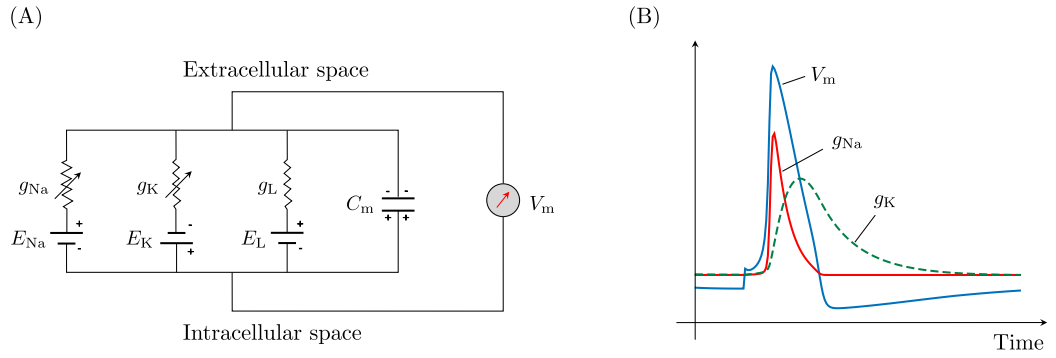

Figure 4.1: (A) Electric circuit model of the Hodgkin-Huxley model. (B) The action potential predicted by the Hodgkin-Model (blue). Further, the red and green curves show the time course of the sodium and potassium conductivities, respectively.

The mathematical model given by Equations (4.2) to (4.8b) was capable of (perfectly) replicating the measured action potential (see Figure 4.1B). Using a verbal description, the behaviour of the model can be described as follows: If the membrane potential reaches a depolarization threshold, i.e., approximately $-55\,\mathrm{mV}$, the activating gates of the sodium channels open and cause a strong sodium influx into the cell. This yields a rapid increase in the membrane potential. Increasing the transmembrane potential successively activates voltage-dependent potassium channels, causing a potassium flux from the cell into the extracellular space. Initially, the sodium current dominates the potassium current, so the transmembrane potential is depolarised. Once the transmembrane potential reaches its peak value, the inactivating gates of the sodium channels close while the potassium channels remain open. This behaviour causes the transmembrane potential to return to its resting potential. After the membrane potential has returned to its resting value, a tiny overshot known as afterhyperpolarisation can be observed. This is because the potassium channels remain open for a short period. Further, since the sodium inactivating gate has a similar (slow) time constant as the potassium channels, there is a refractory period during which the membrane is not excitable.

Mainly driven by the introduction of the patch-clamp technique[4] [195, 238] allowing to study the behaviour of individual ion channels, the knowledge on the behaviour of an excitable cell's membrane has been further refined. Notably, the channels predicted in the work of Hodgkin & Huxley [121] have been confirmed by patch-clamp recordings (as well as from the identification of their genes [202]). Further, the basic framework of the Hodgkin-Huxley model has proven great flexibility to describe various cell types consisting of different combinations of ion channels, for example, cortical neurons [191, 210, 261], spinal motor neurons [13, 32, 193, 213], cardiac myocytes [55, 197, 201] or skeletal muscle fibres [2, 27, 259].

[4] In 1991, Erwin Neher and Bert Sakmann jointly received The Nobel Prize in Physiology or Medicine for their discoveries concerning the function of single ion channels in cells.

4.2 Bioelectromagnetic Fields in the Body

Measuring and analysing bioelectromagnetic fields requires knowing how the source signals are propagated in space. In Chapter 3, Maxwell's equations were introduced as the universal basis for predicting the evolution of the electric field and the magnetic field. This section presents specific (material) models that can describe bioelectromagnetic fields in the human body.

4.2.1 Volume Conductor Models

When simulating bioelectromagnetic fields, the most common approach is to describe the body as an ideal volume conductor interacting with a bioelectric source field. This means that the impact of bound charges and currents is considered negligible. The main challenge in modelling lies in accurately describing the active electric behaviour of the tissue and its conductive properties. The following section provides a brief summary of the volume conductor model. The key modelling assumption is that the overall current density can be additively split up into a conductive current density $\boldsymbol{j}_\mathrm{c}$, i.e., representing extracellular currents, and a (non-conservative) source current density $\boldsymbol{j}_\mathrm{s}$, i.e., reflecting the bioelectric activity of the cells, yielding

$$\boldsymbol{j} \;=\; \boldsymbol{j}_\mathrm{c} + \boldsymbol{j}_\mathrm{s} \;. \tag{4.9}$$

The conductive current is described by Ohm's law, i.e.,

$$\boldsymbol{j}_\mathrm{c} \;=\; -\boldsymbol{\sigma}_\mathrm{b}\,\operatorname{grad}\phi_\mathrm{b} \;, \tag{4.10}$$

where $\boldsymbol{\sigma}_\mathrm{b}$ and ϕ_b are the conductivity tensor and the electric potential in the body, respectively. Assuming quasi-static conditions, the charge balance, i.e., Equation (3.8), is used to obtain for each material point in the body parametrised by a continuous region Ω_b the following partial differential equation:

$$\begin{aligned} \operatorname{div}[\,\boldsymbol{\sigma}_\mathrm{b}\operatorname{grad}\phi_\mathrm{b}] \;&=\; \operatorname{div}\boldsymbol{j}_\mathrm{s} \qquad \text{in } \Omega_\mathrm{b}\;, \\ \Leftrightarrow \operatorname{div}[\boldsymbol{\sigma}_\mathrm{b}\;\operatorname{grad}\phi_\mathrm{b}] \;&=\; I_\mathrm{s} \qquad \text{in } \Omega_\mathrm{b}\;. \end{aligned} \tag{4.11}$$

Equation (4.11) is a generalised Poisson equation, whereby the source term I_s is equivalent to the total transmembrane current flowing into an infinitesimal control volume of the tissue. The quasi-static approximation decouples the electric field problem from the magnetic field problem. Hence, for a known source current distribution, Equation (4.11) allows to predict the electric potential field in the body. Having solved for the electric potential field, the corresponding magnetic field can be calculated straightforwardly from Ampère's law, i.e.,

$$\operatorname{curl}\boldsymbol{B} \;=\; \mu_0\left(-\boldsymbol{\sigma}_\mathrm{b}\operatorname{grad}\phi_\mathrm{b} + \boldsymbol{j}_\mathrm{s}\right) \quad \text{in } \Omega_\mathrm{b}\;. \tag{4.12}$$

Assuming that the magnetic field vanishes at an infinite distance from the body, the Biot-Savard law [93] is a solution to the biomagnetic boundary value problem, i.e.,

$$\boldsymbol{B}(\boldsymbol{r}) \;=\; \frac{\mu_0}{4\pi}\iiint_V \frac{\boldsymbol{j}(\boldsymbol{r}')\times(\boldsymbol{r}-\boldsymbol{r}')}{|\boldsymbol{r}-\boldsymbol{r}'|^3}\,\mathrm{d}V\;. \tag{4.13}$$

Therein, $\boldsymbol{r}$ is an arbitrary observation point, $\boldsymbol{r}'$ is a source point and V parameterises the domain Ω_b.

The volume conductor modelling framework provides great flexibility for describing different bioelectromagnetic fields. For modelling a specific bioelectromagnetic field, for example, induced by the brain, the heart or skeletal muscles, the application-specific challenge is to describe the

bioelectric source field [cf. e.g., Section 8 in 163]. Notably, the source term vanishes when describing electrically inactive tissues, for example, bones, fat or the skin. The source field in skeletal muscles is typically modelled by considering idealised cylindrical fibres. In this case, the fibre radius is considerably smaller than the fibre's longitudinal dimension. Hence, the source current density is assumed to be one-dimensional and computed via Ohm's law:

$$j_{\mathrm{s}} \;=\; \sigma_{\mathrm{i}}^{\mathrm{f}} \frac{\partial \phi_{\mathrm{i}}}{\partial x_{\mathrm{f}}} \;. \tag{4.14}$$

Therein, $\sigma_{\mathrm{i}}^{\mathrm{f}}$ is the intracellular conductivity (along the fibre direction), ϕ_{i} is the intracellular potential, and x_{f} is the spatial coordinate along the fibre path. Further, when assuming that the extracellular potential ϕ_{e} is small compared to the transmembrane potential V_{m}, the source term can be approximated by calculating the second spatial derivative of the transmembrane potential [cf. e.g., 6, 211], i.e.,

$$I_{\mathrm{s}} \;=\; \frac{\partial}{\partial x_{\mathrm{f}}} \left(\sigma_{\mathrm{i}}^{\mathrm{f}} \frac{\partial \phi_{\mathrm{i}}}{\partial x_{\mathrm{f}}} \right) \;=\; \sigma_{\mathrm{i}}^{\mathrm{f}} \frac{\partial^2 (V_{\mathrm{m}} + \phi_{\mathrm{e}})}{\partial x_{\mathrm{f}}^2} \;\approx\; \sigma_{\mathrm{f}}^{\mathrm{l}} \frac{\partial^2 V_{\mathrm{m}}}{\partial x_{\mathrm{f}}^2} \;. \tag{4.15}$$

Note that there exist both analytical descriptions [e.g., 172, 190, 223] as well as numerical models [e.g., 86, 221] to compute the transmembrane potential along a muscle fibre.

Volume conductor models are routinely used for simulating bioelectromagnetic fields from various tissues. Depending on the volume conductor's geometry and the conductivity tensor's spatial heterogeneity, the corresponding model equations can be solved analytically or need to be approximated numerically. Specifically regarding skeletal muscle, volume conductor models [for reviews see 179, 242] have been used extensively for studying EMG signals, for example, for investigating the relation between the tissue properties and the signal shape [58, 158, 159], optimising the detection system [66, 68], assisting the interpretation of experimental findings [57, 176, 219], or studying the influence of motions [181, 185]. Further, volume conductor models are routinely used for reconstructing the bioelectric source field associated with an electroencephalogram (EEG) or magnetoencephalogram (MEG) [e.g., 98, 204, 228, 257], modelling the electrocardiogram (ECG) or the magnetocardiogram (MCG) in the torso [e.g., 31, 137] or for simulating the defibrillation of the heart [e.g., 36, 252].

4.2.2 The Bidomain Model

The forward solution of a volume conductor model requires that the bioelectric source field is known. However, for some tissues, the behaviour of the bioelectric sources is complexly coupled to the tissue properties and the applied boundary conditions. Hence, accurately describing the bioelectric sources in the body a priori can be highly challenging. For such cases, models mechanistically linking the biophysical behaviour of the body and the generated bioelectromagnetic fields are needed. Theoretically, this would be possible by simulating all cells in a tissue and their coupling. However, for obvious reasons, such an approach becomes quickly impractical. For example, the number of cells in the brain and the heart is in the order of 10^{10}, and the number of muscle fibres in the biceps is in the order of 10^6. Suppose one assumes that several cells behave similarly and only macroscopic effects are relevant. In that case, the complexity can be reduced by considering a tissue consisting of individual cells as a multiphase continuum body.

The bidomain model is a bioelectric multiscale continuum model proposed in the late 1970s [182, 254] and is currently accepted as the gold standard for simulating the electric behaviour of the heart [cf. e.g., 37, 110]. A brief description of the bidomain model is provided in the

following. The critical assumption of the bidomain model is that at each material point of an excitable tissue, i.e., $\mathcal{P} \in \Omega_\mathrm{m}$, an intracellular domain and an extracellular domain coexist. Hence, one can introduce for each domain an individual electric potential, which is related through the transmembrane potential V_m, i.e.,

$$V_\mathrm{m} \;=\; \phi_\mathrm{i} \,-\, \phi_\mathrm{e} \;. \tag{4.16}$$

Therein, ϕ_i denotes the electric potential in the intracellular domain, and ϕ_e is the electric potential in the extracellular domain. Further, the overall current density can be additively decomposed into

$$\boldsymbol{j} \;=\; \boldsymbol{j}_\mathrm{e} \,+\, \boldsymbol{j}_\mathrm{i} \;, \tag{4.17}$$

where $\boldsymbol{j}_\mathrm{e}$ is the current density in the extracellular domain and $\boldsymbol{j}_\mathrm{i}$ is the current density in the intracellular domain. The conservation of charges requires that

$$\operatorname{div}(\boldsymbol{j}_\mathrm{e} + \boldsymbol{j}_\mathrm{i}) \;=\; 0 \quad \text{in } \Omega_\mathrm{m} \;. \tag{4.18}$$

Hence, in the absence of additional current sources, the charge balance holds if any current leaving the intracellular domain via the cell membrane enters the extracellular domain. Mathematically, this assumption yields two (local) balance equations, i.e.,

$$-\operatorname{div} \boldsymbol{j}_\mathrm{i} \;=\; \operatorname{div} \boldsymbol{j}_\mathrm{e} \quad \text{in } \Omega_\mathrm{m} \;, \tag{4.19a}$$

$$-\operatorname{div} \boldsymbol{j}_\mathrm{i} \;=\; A_\mathrm{m} I_\mathrm{m} \quad \text{in } \Omega_\mathrm{m} \;. \tag{4.19b}$$

where I_m is the transmembrane current density and A_m is the surface-to-volume area of a representative cell. Notably, both the transmembrane current density and the surface-to-volume area of the cells represent microscopic properties. Hence, the bidomain model can be classified as a multiscale model, i.e., considering the most important microscopic tissue properties for predicting its macroscopic electric behaviour. Assuming that in each domain, the currents are purely conductive, the current densities are related to the electric potentials via Ohm's law:

$$\boldsymbol{j}_\mathrm{e} \;=\; -\boldsymbol{\sigma}_\mathrm{e} \operatorname{grad} \phi_\mathrm{e} \;, \tag{4.20a}$$

$$\boldsymbol{j}_\mathrm{i} \;=\; -\boldsymbol{\sigma}_\mathrm{i} \operatorname{grad} \phi_\mathrm{i} \;. \tag{4.20b}$$

Therein, $\boldsymbol{\sigma}_\mathrm{e}$ is the conductivity tensor in the extracellular domain, and $\boldsymbol{\sigma}_\mathrm{i}$ is the conductivity tensor in the intracellular domain. Hence, Equation (4.19a) can be rewritten to yield

$$\operatorname{div}\left[(\boldsymbol{\sigma}_\mathrm{e} + \boldsymbol{\sigma}_\mathrm{i}) \operatorname{grad} \phi_\mathrm{e}\right] \,+\, \operatorname{div}\left[\boldsymbol{\sigma}_\mathrm{i} \operatorname{grad} V_\mathrm{m}\right] \;=\; 0 \quad \text{in } \Omega_\mathrm{m} \;. \tag{4.21}$$

Further, Equation (4.19b) is used to obtain

$$\operatorname{div}\left[\boldsymbol{\sigma}_\mathrm{i} \operatorname{grad} V_\mathrm{m}\right] \,+\, \operatorname{div}\left[\boldsymbol{\sigma}_\mathrm{i} \operatorname{grad} \phi_\mathrm{e}\right] \;= A_\mathrm{m}\, I_\mathrm{m} \quad \text{in } \Omega_\mathrm{m} \;. \tag{4.22}$$

For solving Equation (4.22), a mathematical description of the transmembrane current density I_m is needed. This can be achieved by using the microscale electric circuit model of the Hodgkin-Huxley formalism (see Section 4.1.2). Thus, using Equation (4.2) yields for every material point $\mathcal{P} \in \Omega_\mathrm{m}$ the following set of coupled differential equations:

$$0 \;=\; \operatorname{div}\left[(\boldsymbol{\sigma}_\mathrm{e} + \boldsymbol{\sigma}_\mathrm{i}) \operatorname{grad} \phi_\mathrm{e}\right] \,+\, \operatorname{div}\left[\boldsymbol{\sigma}_\mathrm{i} \operatorname{grad} V_\mathrm{m}\right] \;, \tag{4.23a}$$

$$\frac{\partial V_\mathrm{m}}{\partial t} \;=\; \frac{1}{C_\mathrm{m} A_\mathrm{m}} \Big(\operatorname{div}\left[\boldsymbol{\sigma}_\mathrm{i} \operatorname{grad} V_\mathrm{m}\right] \,+\, \operatorname{div}\left[\boldsymbol{\sigma}_\mathrm{i} \operatorname{grad} \phi_\mathrm{e}\right] \,-\, A_\mathrm{m} I_\mathrm{ion}(\boldsymbol{y}, V_\mathrm{m}) \Big) \;, \tag{4.23b}$$

$$\dot{\boldsymbol{y}} \;=\; \boldsymbol{g}(\boldsymbol{y}, V_\mathrm{m}) \;. \tag{4.23c}$$

The vector $\boldsymbol{y}$ summarises all state variables required for calculating the ionic current flowing over the membrane, and $\boldsymbol{g}$ is a vector-valued function describing their evolution. Further, it is noted that the bidomain model can be coupled to a volume conductor model (see Section 4.2.1) to simulate the influence of surrounding electrically inactive tissues.

When a scalar can relate the intracellular conductivity tensor $\boldsymbol{\sigma}_\mathrm{i}$ and the extracellular conductivity tensor $\boldsymbol{\sigma}_\mathrm{e}$, the bidomain model can be simplified to yield the monodomain model [cf. e.g., Chapter 12 in 138]. The monodomain model has, for example, been used for predicting the propagation of action potentials in individual muscle fibres [106, 185, 221]. Further, the monodomain model is often applied as a computationally less demanding approximation of the bidomain model [e.g., 199]. For modelling the propagation of electrical waves in the gastrointestinal tract, there exist modifications of the bidomain model taking into account not only one but two different cell types [cf. 23, 42]. However, it is noted that none of the existing bidomain-type models can adequately describe bioelectromagnetic fields induced by (whole) skeletal muscles.

Part II

A Mathematical Modelling Framework for Simulating EMG and MMG

5 A Multiscale Model for Muscle-Induced Bioelectromagnetic Fields

This chapter aims to derive a mathematical model that enables systematic investigations of EMG and MMG signals. Since the temporal dynamics of the muscle-induced bioelectromagnetic fields are in the range of milliseconds, one can assume quasi-static conditions. The quasi-static approximation of Maxwell's equations allows us to decouple the electric field equations from the magnetic field equations. Hence, Section 5.1 introduces a modelling framework mechanistically linking the electrophysiological behaviour of skeletal muscles to the electric potential fields in the body. With the solution of the electric field problem at hand, Section 5.2 derives the equations for predicting the magnetic field generated by the muscle. Further, obtaining meaningful *in silico* predictions of muscle-induced bioelectromagnetic fields requires suitable model parameters specified in Section 5.3. Note that the presented simulation framework was previously published in Klotz et al. [140, 141].

5.1 Modelling the Muscle-Induced Electric Field

Section 5.1.1 presents a novel multiscale model for describing the electric behaviour of skeletal muscles. The latter consistently integrates a microscale description of the transmembrane currents across the muscle fibre membranes and skeletal muscle tissue's most important structural properties into a multiphase continuum model at the macroscale. To simulate the muscle-induced electric potential field in the entire body, the electrophysiological skeletal muscle model can be coupled to a volume conductor model (see Section 5.1.2), for example, resolving the influence of the subcutaneous fat or the skin. The overall model yields a set of coupled differential equations. Hence, in Section 5.1.3, the necessary interface and boundary conditions are derived.

5.1.1 A Multi-Domain Model for Skeletal Muscle Tissue

Skeletal muscle tissue is a heterogeneous material of muscle fibres associated with different motor units and extracellular matrix (see Figure 5.1). All muscle fibres in the same motor unit are activated synchronously during voluntary contractions. Further, all muscle fibres innervated by the same motor neuron show similar properties. Hence, instead of modelling each muscle fibre individually, it is possible to simulate the behaviour of all fibres belonging to one motor unit in an averaged sense. Within an idealised macroscopic continuum model, one can assume that there coexist at each skeletal muscle material point $\mathcal{P} \in \Omega_{\mathrm{m}}$ an extracellular space and N intracellular spaces, with N denoting the number of motor units. Given this homogenised tissue representation, an electric potential is introduced for each domain, i.e., ϕ_{e} and ϕ_{i}^{k}, $\forall\, k \in \mathcal{M}_{\mathrm{MU}} := \{1, 2, ..., N\}$. Thereby, the subscripts $(\cdot)_{\mathrm{e}}$ and $(\cdot)_{\mathrm{i}}$ denote extracellular and intracellular quantities, respectively. Further, a transmembrane potential V_{m}^{k} can be calculated for each motor unit, i.e.,

$$V_{\mathrm{m}}^{k} = \phi_{\mathrm{i}}^{k} - \phi_{\mathrm{e}} \ , \ \forall\, k \in \mathcal{M}_{\mathrm{MU}} \ . \tag{5.1}$$

The challenge is now to accurately model the electric properties of the individual domains and their coupling based on the biophysical function of skeletal muscles. The macroscopic electric

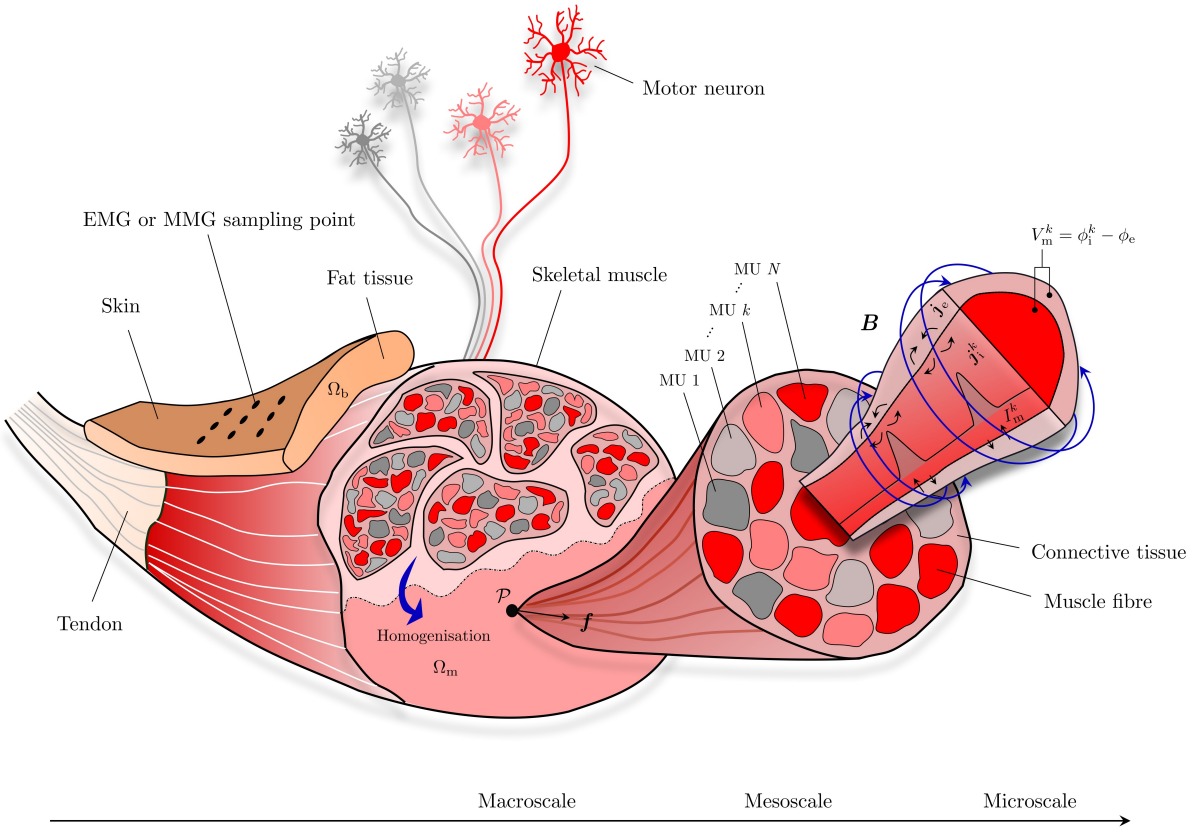

Figure 5.1: Schematic drawing illustrating the concept of the proposed multiscale skeletal muscle model. The heterogeneous muscle structure on the macroscale is homogenised and represented by an idealised, continuous multi-domain material. To couple the different domains, the multiscale model captures the most important features of the muscle's structure. That is the motor unit composition on the mesoscale and the (microscale) interaction of one representative muscle fibre per motor unit and the extracellular space via the muscle fibre membrane. For the illustrated muscle fibres, each colour represents a different motor unit. Based on those key assumptions, the continuum model predicts for each skeletal muscle material point $\mathcal{P} \in \Omega_m$ the muscle-induced electric potential fields, i.e., the transmembrane potentials V_m^k as well as the extracellular potential ϕ_e. Having described the electric field problem, the magnetostatic approximation allows us to compute the muscle-induced magnetic field $\boldsymbol{B}$ (blue arrows). To compute the bioelectromagnetic fields in the whole body, the multi-domain model can be coupled to a volume conductor describing surrounding electrically inactive tissues, for example, fat tissue or the skin. This is particularly relevant for investigating signals that can be measured non-invasively. Hence, the (virtual) measurement of surface EMG signals or non-invasive MMG signals is schematically illustrated by a grid of sampling points on the body surface.

behaviour of skeletal muscles is closely related to the tissue's microscopic properties. Hence, the coupling will be achieved through a multiscale approach, resolving the most important features of a muscle's mesostructure and microstructure and the microscale electric behaviour of the muscle fibre membranes. These basic assumptions lead to a multi-domain modelling framework for simulating the electric potential fields in skeletal muscles. This is explained in more detail below.

To guarantee consistency with the fundamental laws of physics, the starting point for modelling the electric behaviour of skeletal muscles is the conservation of electric charges, cf. Chapter 3.

For an idealised multi-domain material, the conservation of charges can be enforced if the outward volume fluxes of the current densities from all domains are balanced at each skeletal muscle material point $\mathcal{P}$. This corresponds to a set of balance equations. The muscle fibre membrane contains ion channels for selectively exchanging ions with its environment (see Section 2.2). Thus, it can be assumed that ions can flow between an intracellular domain and the extracellular space. However, there exist no current fluxes between the different intracellular domains. Further, it can be assumed that the muscle fibres of the same motor unit show similar biophysical properties (see Section 2.3.3). Hence, at each skeletal muscle material point, the coupling between an intracellular space k and the extracellular space is modelled by describing the interaction of one representative muscle fibre per motor unit with the extracellular space. Mathematically, this is achieved by relating the current density outward volume flux of an intracellular domain to the transmembrane current density I_{m}^{k}, i.e.,

$$\operatorname{div} \boldsymbol{j}_{\mathrm{i}}^{k} \;=\; A_{\mathrm{m}}^{k} I_{\mathrm{m}}^{k} \;,\; k \in \mathcal{M}_{\mathrm{MU}} \quad \text{in } \Omega_{\mathrm{m}} \,. \tag{5.2}$$

Therein, $\boldsymbol{j}_{\mathrm{i}}^{k}$ is the current density of an intracellular domain associated with motor unit k in a representative fibre-matrix cylinder and A_{m}^{k} is the surface-to-volume ratio of a muscle fibre belonging to motor unit k, i.e., representing the microscale geometry of the muscle fibres. Further note that the transmembrane current density I_{m}^{k} reflects the (microscale) dynamic ionic permeability of the muscle fibre membranes, i.e., the source of bioectromagnetic fields. The extracellular space's current density outward volume flux is the sum of the transmembrane current densities from all motor units. As the fibre density for each motor unit is variable in space, the transmembrane current densities are weighted by a mesoscale parameter f_{r}^{k}, reflecting the motor unit composition at each skeletal muscle material point. This yields

$$\operatorname{div} \boldsymbol{j}_{\mathrm{e}} \;=\; -\sum_{k=1}^{N} f_{\mathrm{r}}^{k} A_{\mathrm{m}}^{k} I_{\mathrm{m}}^{k} \quad \text{in } \Omega_{\mathrm{m}} \,, \tag{5.3}$$

where $\boldsymbol{j}_{\mathrm{e}}$ denotes the extracellular current density. Inserting Equation (5.2) into Equation (5.3) yields the total current balance, where the total current density is given by

$$\boldsymbol{j} \;=\; \boldsymbol{j}_{\mathrm{e}} + \sum_{k=1}^{N} f_{\mathrm{r}}^{k} \boldsymbol{j}_{\mathrm{i}}^{k} \,. \tag{5.4}$$

Thereby, it is evident that the electric charges are conserved if Equation (5.2) and Equation (5.3) hold. Notably, the domain-specific current densities are given in two different length scales, i.e., a representative fibre-matrix cylinder for the intracellular domains and a control volume including multiple muscle fibres for the extracellular domain. This is essential as the electric behaviour of the intracellular domains is dominantly determined by the microscopic single-fibre scale. However, the current density in the extracellular domain strongly depends on the mesoscale motor unit composition. The parameter f_{r}^{k} guarantees consistency across both scales. Note that f_{r}^{k} can be interpreted as the probability of finding a muscle fibre associated with motor unit k is a representative control volume and hence,

$$\sum_{k=1}^{N} f_{\mathrm{r}}^{k} \;=\; 1 \tag{5.5}$$

must hold for each skeletal muscle material point $\mathcal{P}$.

Constitutive relations are required to express the derived current balance equations in terms of the model's primary variables, i.e., the extracellular potential ϕ_{e} and the transmembrane

potentials V_m^k ($\forall\ k \in \mathcal{M}_\mathrm{MU}$). Within the limits of the quasi-static approximation, polarisation currents vanish, cf. Section 3.4. It is also assumed that the magnetising currents are negligible for skeletal muscle tissue. Hence, the current densities are purely conductive, and Ohm's law can be used to relate the electric potentials and the current densities, i.e.,

$$\begin{aligned} \boldsymbol{j}_\mathrm{e} &= -\boldsymbol{\sigma}_\mathrm{e} \operatorname{grad} \phi_\mathrm{e} \ , && \text{(5.6a)} \\ \boldsymbol{j}_\mathrm{i}^k &= -\boldsymbol{\sigma}_\mathrm{i}^k \operatorname{grad} \phi_\mathrm{i}^k \ , \ \forall\ k \in \mathcal{M}_\mathrm{MU} \ . && \text{(5.6b)} \end{aligned}$$

Therein, $\boldsymbol{\sigma}_\mathrm{e}$ and $\boldsymbol{\sigma}_\mathrm{i}^k$ ($\forall\ k \in \mathcal{M}_\mathrm{MU}$) denote the extracellular conductivity tensor and the intracellular conductivity tensors, respectively. Using Equations (5.6a) and (5.6b) the intracellular current balances, i.e., Equation (5.2), can be rewritten to yield

$$\begin{aligned} \operatorname{div} \boldsymbol{j}_\mathrm{i}^k &= A_\mathrm{m}^k\, I_\mathrm{m}^k \ , \ \forall\ k \in \mathcal{M}_\mathrm{MU} \quad \text{in } \Omega_\mathrm{m} \ , \\ \Leftrightarrow \operatorname{div} \left[\boldsymbol{\sigma}_\mathrm{i}^k \operatorname{grad} \phi_\mathrm{i}^k \right] &= A_\mathrm{m}^k\, I_\mathrm{m}^k \ , \ \forall\ k \in \mathcal{M}_\mathrm{MU} \quad \text{in } \Omega_\mathrm{m} \ , \\ \Leftrightarrow \operatorname{div} \left[\boldsymbol{\sigma}_\mathrm{i}^k \operatorname{grad} \left(V_\mathrm{m}^k + \phi_\mathrm{e} \right) \right] &= A_\mathrm{m}^k\, I_\mathrm{m}^k \ , \ \forall\ k \in \mathcal{M}_\mathrm{MU} \quad \text{in } \Omega_\mathrm{m} \ . \end{aligned} \tag{5.7}$$

In the same way, the extracellular current balance, i.e., Equation (5.3), is reformulated and one obtains:

$$\begin{aligned} \operatorname{div} \boldsymbol{j}_\mathrm{e} + \sum_{k=1}^{N} f_\mathrm{r}^k \operatorname{div} \boldsymbol{j}_\mathrm{i}^k &= 0 \quad \text{in } \Omega_\mathrm{m} \ , \\ \Leftrightarrow \ \operatorname{div} \left[\boldsymbol{\sigma}_\mathrm{e} \operatorname{grad} \phi_\mathrm{e} \right] + \sum_{k=1}^{N} f_\mathrm{r}^k \operatorname{div} \left[\boldsymbol{\sigma}_\mathrm{i}^k \operatorname{grad} \phi_\mathrm{i}^k \right] &= 0 \quad \text{in } \Omega_\mathrm{m} \ , \\ \Leftrightarrow \ \operatorname{div} \left[\boldsymbol{\sigma}_\mathrm{e} \operatorname{grad} \phi_\mathrm{e} \right] + \sum_{k=1}^{N} f_\mathrm{r}^k \operatorname{div} \left[\boldsymbol{\sigma}_\mathrm{i}^k \operatorname{grad} \left(V_\mathrm{m}^k + \phi_\mathrm{e} \right) \right] &= 0 \quad \text{in } \Omega_\mathrm{m} \ , \\ \Leftrightarrow \ \operatorname{div} \left[\left(\boldsymbol{\sigma}_\mathrm{e} + \sum_{k=1}^{N} f_\mathrm{r}^k \boldsymbol{\sigma}_\mathrm{i}^k \right) \operatorname{grad} \phi_\mathrm{e} \right] + \sum_{k=1}^{N} f_\mathrm{r}^k \operatorname{div} \left[\boldsymbol{\sigma}_\mathrm{i}^k \operatorname{grad} V_\mathrm{m}^k \right] &= 0 \quad \text{in } \Omega_\mathrm{m} \ . \end{aligned} \tag{5.8}$$

Completing the model equations requires a mathematical description for the microscale transmembrane current densities I_m^k. For this purpose, one can utilise an electrical circuit model of the muscle fibre membrane, i.e., using the Hodgkin-Huxley formalism as described in Section 4.1.2. For a generic electric circuit model of the muscle fibre membrane, the transmembrane current density across a representative membrane patch can be calculated from Kirchhoff's current law, i.e.,

$$I_\mathrm{m}^k = C_\mathrm{m}^k \frac{\partial V_\mathrm{m}^k}{\partial t} + I_\mathrm{ion}^k \left(\boldsymbol{y}^k, V_\mathrm{m}^k, I_\mathrm{stim}^k \right) \ , \ \forall\ k \in \mathcal{M}_\mathrm{MU} \ . \tag{5.9}$$

Therein, C_m^k is the membrane capacitance per unit area of a muscle fibre belonging to motor unit k, I_ion^k is the total conductive current density through a membrane patch associated with motor unit k and I_stim^k is an external stimulus that is used to describe the motor nerve stimuli of motor unit k at the neuromuscular junctions. Further, $\boldsymbol{y}^k$ ($\forall\ k \in \mathcal{M}_\mathrm{MU}$) is a vector of additional membrane state variables, for example, describing the probability of an ion channel's gate to be open or closed. This is required for modelling the dynamic ionic permeability of the membrane. Without introducing a specific membrane model, a generally valid description for the evolution of the membrane state vector $\boldsymbol{y}^k$ can be formulated as follows $\forall\ k \in \mathcal{M}_\mathrm{MU}$

$$\begin{aligned} \dot{\boldsymbol{y}}^k &= \boldsymbol{g}^k \left(\boldsymbol{y}^k, V_\mathrm{m}^k, I_\mathrm{stim}^k \right) \ , \ \text{with} \\ \boldsymbol{y}_0^k &= \boldsymbol{y}^k(t=0) \ . \end{aligned} \tag{5.10}$$

Therein, $\boldsymbol{g}^k(\boldsymbol{y}^k, V_\mathrm{m}^k, I_\mathrm{stim}^k)$ is a vector-valued function representing the right-hand side of the differential equations describing the dynamics of the membrane state vector $\boldsymbol{y}^k$.

Combing Equation (5.7), Equation (5.8), Equation (5.9) and Equation (5.10) yields for each skeletal muscle material point $\mathcal{P} \in \Omega_\mathrm{m}$ the following system of coupled differential equations:

$$0 \;=\; \operatorname{div}\left[\boldsymbol{\sigma}_\mathrm{e} \operatorname{grad} \phi_\mathrm{e}\right] + \sum_{k=1}^{N} f_\mathrm{r}^k \operatorname{div}\left[\boldsymbol{\sigma}_\mathrm{i}^k \operatorname{grad}\left(V_\mathrm{m}^k + \phi_\mathrm{e}\right)\right] \;, \tag{5.11a}$$

$$\frac{\partial V_\mathrm{m}^k}{\partial t} \;=\; \frac{1}{C_\mathrm{m}^k A_\mathrm{m}^k}\Big(\operatorname{div}\left[\boldsymbol{\sigma}_\mathrm{i}^k \operatorname{grad}\left(V_\mathrm{m}^k + \phi_\mathrm{e}\right)\right] \;-\; A_\mathrm{m}^k I_\mathrm{ion}^k(\boldsymbol{y}^k, V_\mathrm{m}^k, I_\mathrm{stim}^k)\Big) \;,\; \forall\; k \in \mathcal{M}_\mathrm{MU} \;, \tag{5.11b}$$

$$\dot{\boldsymbol{y}}^k \;=\; \boldsymbol{g}^k(\boldsymbol{y}^k, V_\mathrm{m}^k, I_\mathrm{stim}^k) \;,\; \forall\; k \in \mathcal{M}_\mathrm{MU} \;. \tag{5.11c}$$

Equations (5.11a) to (5.11c) are referred to as the multi-domain model of skeletal muscle tissue and relate the microscopic electrophysiological behaviour of skeletal muscles to the generated macroscopic electric potential fields.

5.1.2 The Electric Potential Field in the Body

Skeletal muscles are surrounded by electrically inactive tissues, for example, connective tissues, subcutaneous fat or the skin. Electrically inactive tissues considerably influence the electric potential field at the body surface. As described in Section 4.2.1, electrically inactive tissues can be modelled as ideal volume conductors. Accordingly, all currents are purely conductive and can be described by Ohm's law. Further, it is noted that in electrically inactive tissues, no current sources exist. Hence, from the charge balance one obtains

$$\begin{aligned} \operatorname{div} \boldsymbol{j}_\mathrm{b} \;&=\; 0 \quad \text{in } \Omega_\mathrm{b} \;, \\ \Leftrightarrow \operatorname{div}\left[\boldsymbol{\sigma}_\mathrm{b} \operatorname{grad} \phi_\mathrm{b}\right] \;&=\; 0 \quad \text{in } \Omega_\mathrm{b} \;, \end{aligned} \tag{5.12}$$

where the body region Ω_b summarises all electrically inactive tissues and $\boldsymbol{j}_\mathrm{b}$ is the current density in the body region. Further, ϕ_b and $\boldsymbol{\sigma}_\mathrm{b}$ are the body region's electric potential and conductivity tensor, respectively. Mathematically, Equation (5.12) represents a generalised Laplace equation.

5.1.3 Boundary Conditions for the Electric Field Problem

Boundary conditions and interface conditions are required to solve the coupled differential equations derived in Sections 5.1.1 to 5.1.2. A schematic drawing illustrating the different regions and their coupling is shown in Figure 5.2. First, it is noted that muscle fibres are electrically insulated by their membranes. Hence, it can be assumed that no charges can leave the intracellular domains at their boundary. This is modelled by applying zero Neumann boundary conditions to the intracellular potential, yielding $\forall\; k \in \mathcal{M}_\mathrm{MU}$

$$\begin{aligned} \left[\boldsymbol{\sigma}_\mathrm{i}^k \operatorname{grad} \phi_\mathrm{i}^k\right] \cdot \boldsymbol{n}_\mathrm{m} \;&=\; 0 && \text{on } \Gamma_\mathrm{m} \;, \\ \Leftrightarrow \left[\boldsymbol{\sigma}_\mathrm{i}^k \operatorname{grad} V_\mathrm{m}^k\right] \cdot \boldsymbol{n}_\mathrm{m} \;&=\; -\left[\boldsymbol{\sigma}_\mathrm{i}^k \operatorname{grad}\, \phi_\mathrm{e}\right] \cdot \boldsymbol{n}_\mathrm{m} && \text{on } \Gamma_\mathrm{m} \;. \end{aligned} \tag{5.13}$$

Therein, "$\cdot$" denotes the scalar product and $\boldsymbol{n}_\mathrm{m}$ is a unit outward normal vector at the muscle surface Γ_m, cf. Figure 5.2. Further, it is assumed that no charges can leave the body, yielding zero Neumann boundary conditions for the electric potential in the body region, i.e.,

$$\left[\boldsymbol{\sigma}_\mathrm{b} \operatorname{grad} \phi_\mathrm{b}\right] \cdot \boldsymbol{n}_\mathrm{b}^\mathrm{out} \;=\; 0 \quad \text{on } \Gamma_\mathrm{b}^\mathrm{out} \;. \tag{5.14}$$

Therein, $\boldsymbol{n}_\mathrm{b}^\mathrm{out}$ denotes a unit outward normal vector of the body surface $\Gamma_\mathrm{b}^\mathrm{out}$, cf. Figure 5.2. In case the outer surface of the simulated body is the muscle's boundary (or part thereof), the same assumption holds, but with zero Neumann boundary conditions for the extracellular potential, i.e.,

$$[\boldsymbol{\sigma}_\mathrm{e} \operatorname{grad} \phi_\mathrm{e}] \cdot \boldsymbol{n}_\mathrm{m} \;=\; 0 \quad \text{on } \Gamma_\mathrm{m} \setminus \Gamma_\mathrm{b} \;. \tag{5.15}$$

While this case does not correspond to conditions *in vivo*, this boundary condition is useful as most *in silico* experiments are restricted to a particular region of interest.

To couple the muscle region and the body region, it is assumed that at the muscle-body interface, the extracellular potential ϕ_e and the electric potential of the body region ϕ_b are continuous, i.e.,

$$\phi_\mathrm{e} \;=\; \phi_\mathrm{b} \qquad \text{on } \Gamma_\mathrm{m} \cap \Gamma_\mathrm{b} \;. \tag{5.16}$$

Further, the current flux between the extracellular space and the body region must be balanced, yielding

$$\left[\boldsymbol{\sigma}_\mathrm{e} \operatorname{grad} \phi_\mathrm{e} \;-\; \boldsymbol{\sigma}_\mathrm{b} \operatorname{grad} \phi_\mathrm{b}\right] \cdot \boldsymbol{n}_\mathrm{m} \;=\; 0 \quad \text{on } \Gamma_\mathrm{m} \cap \Gamma_\mathrm{b} \;. \tag{5.17}$$

Finally, it is noted that an electric potential field is not unique, i.e., the potential can be shifted by an arbitrary scalar value (cf. Chapter 3). To guarantee a unique solution for the mathematical problem, one can simulate a grounding electrode by prescribing the potential at the grounding electrode's location. This is equivalent to an additional Dirichlet boundary condition.

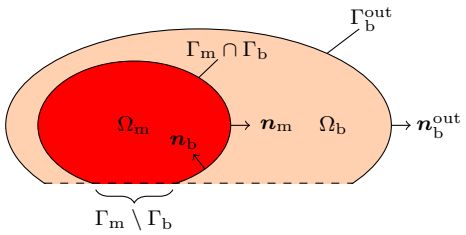

Figure 5.2: Schematic illustration of an arbitrary geometrical arrangement of muscle tissue Ω_m, the body region Ω_b and their interfaces. Thereby, Γ_m denotes the muscle boundary with unit outward normal vector $\boldsymbol{n}_\mathrm{m}$, $\Gamma_\mathrm{b}^\mathrm{out}$ is the body surface with unit outward normal vector $\boldsymbol{n}_\mathrm{b}^\mathrm{out}$ and Γ_b is an inner boundary of the body region with unit outward normal vector $\boldsymbol{n}_\mathrm{b}$.

5.2 Modelling the Muscle-Induced Magnetic Field

Section 5.1 established a mathematical model of the muscle-induced electric activity in the human body. Assuming quasi-static conditions, this fully determines the magnetic field generated by the muscle (see Chapter 3). The equations to describe the magnetic field in the muscle region as well as in the body region are presented in Section 5.2.1 and in Section 5.2.2, respectively. Further, in Section 5.2.3, a description of the magnetic field around the body is introduced. This is particularly relevant as MMG measurements do not rely on direct contact with the body. Finally, the boundary and interface conditions for the magnetic field problem are introduced in Section 5.2.4.

5.2.1 The Magnetic Field in Skeletal Muscles

Within the limits of the magnetostatic approximation, the magnetic field $\boldsymbol{B}$ is fully determined by the overall current density. To describe the electric behaviour of skeletal muscles, it was

assumed that the total current density is purely conductive (see Section 5.1.1). Since this assumption is crucial for modelling the magnetic field induced by the muscle, the arguments are revisited here:

i.) The characteristic time scale of the MMG is in the range of milliseconds. Hence, the quasi-static approximation holds, and polarisation currents are negligible.

ii.) The magnetic susceptibility of muscle tissue is approximately zero. Hence, skeletal muscles can be classified as non-magnetic material with negligible magnetisation currents.

Two types of conductive currents exist in the multi-domain skeletal muscle model, i.e., the macroscopic current densities in each domain and the microscopic transmembrane current densities. However, due to geometrical arguments, the microscopic transmembrane current densities can be eliminated to calculate the macroscopic magnetic field. The muscle fibres are (approximately) cylindrically shaped with a radius considerably smaller than the characteristic length scale of the macroscopic continuum model. Hence, when the transmembrane current density is uniformly distributed on the membrane surface, their contributions cancel each other out. In conclusion, the muscle-induced magnetic field can be predicted based on the total macroscopic current density given in Equation (5.4). Accordingly, the magnetic vector potential for every material point $\mathcal{P} \in \Omega_\mathrm{m}$ within the muscle region is determined by

$$\begin{aligned} \operatorname{div}(\operatorname{grad} \boldsymbol{A}) &= \mu_0 \left(\boldsymbol{j}_\mathrm{e} + \sum_{k=1}^{N} f_\mathrm{r}^k \boldsymbol{j}_\mathrm{i}^k \right) , \\ \Leftrightarrow \operatorname{div}(\operatorname{grad} \boldsymbol{A}) &= -\mu_0 \left(\boldsymbol{\sigma}_\mathrm{e} \operatorname{grad} \phi_\mathrm{e} + \sum_{k=1}^{N} f_\mathrm{r}^k \boldsymbol{\sigma}_\mathrm{i}^k \operatorname{grad} \phi_\mathrm{i}^k \right) , \\ \Leftrightarrow \operatorname{div}(\operatorname{grad} \boldsymbol{A}) &= -\mu_0 \left(\boldsymbol{\sigma}_\mathrm{e} \operatorname{grad} \phi_\mathrm{e} + \sum_{k=1}^{N} f_\mathrm{r}^k \boldsymbol{\sigma}_\mathrm{i}^k \operatorname{grad}(V_\mathrm{m}^k + \phi_\mathrm{e}) \right) . \end{aligned} \tag{5.18}$$

The potential formulation is chosen as this yields a Poisson-type equation for which various well-established solution methods exist. Having solved for the magnetic vector potential $\boldsymbol{A}$, the experimentally measurable magnetic field $\boldsymbol{B}$ can be calculated directly from Equation (3.9b). Notably, the linearity of the magnetostatic equations can be exploited to predict the contribution of each domain to the MMG signal. The total magnetic field is the superposition of the fields generated by the individual right-hand terms.

5.2.2 The Magnetic Field in the Body

For the body region, there are only conductive currents. Hence, the magnetic vector potential is described as follows

$$\begin{aligned} \operatorname{div}(\operatorname{grad} \boldsymbol{A}) &= \mu_0 \boldsymbol{j}_\mathrm{b} && \text{in } \Omega_\mathrm{b} , \\ \Leftrightarrow \operatorname{div}(\operatorname{grad} \boldsymbol{A}) &= -\mu_0 \left[\boldsymbol{\sigma}_\mathrm{b} \operatorname{grad} \phi_\mathrm{b} \right] && \text{in } \Omega_\mathrm{b} . \end{aligned} \tag{5.19}$$

5.2.3 The Magnetic Field Outside the Body

While EMG measurements rely on direct contact with the body, MMG can be recorded contact-free. Therefore, one also needs to model the environment of the body. Since air can be assumed to be free of electric currents, the source term vanishes, i.e.,

$$\operatorname{div}(\operatorname{grad} \boldsymbol{A}) = \boldsymbol{0} \quad \text{in } \Omega_\mathrm{f} , \tag{5.20}$$

where Ω_f refers to the region outside the body. Further, $\boldsymbol{0}$ is a vector of zeros.

5.2.4 Boundary Conditions for the Magnetic Field Problem

For the magnetic vector potential, it can be assumed that far away from the muscle, i.e., the bioelectric sources, the magnetic vector potential vanishes. Thus, zero Dirichlet boundary conditions are applied to all infinitely distant points Γ_∞ (see Figure 5.3), i.e.,

$$\boldsymbol{A} = \boldsymbol{0} \quad \text{on } \Gamma_\infty \, . \tag{5.21}$$

Further, the magnetic vector potential is continuous at the interface between two media [cf. e.g., 93]. This is accounted for through

$$\boldsymbol{A}_\mathrm{m} = \boldsymbol{A}_\mathrm{b} \quad \text{on } \Gamma_\mathrm{m} \cap \Gamma_\mathrm{b} \, , \tag{5.22a}$$
$$\boldsymbol{A}_\mathrm{m} = \boldsymbol{A}_\mathrm{f} \quad \text{on } \Gamma_\mathrm{m} \setminus \Gamma_\mathrm{b} \, , \tag{5.22b}$$
$$\boldsymbol{A}_\mathrm{b} = \boldsymbol{A}_\mathrm{f} \quad \text{on } \Gamma_\mathrm{b}^\mathrm{out} \, , \tag{5.22c}$$

where the subscripts refer to the medium contributing to the interface, cf. Figure 5.3. That is, $\boldsymbol{A}_\mathrm{m}$ is the magnetic vector potential in the muscle region, $\boldsymbol{A}_\mathrm{b}$ is the magnetic vector potential in the body region and $\boldsymbol{A}_\mathrm{f}$ is the magnetic vector potential outside the muscle. Further, surface currents are negligible for biological tissues, i.e., they only exhibit volume conduction. Accordingly, the fluxes of the magnetic vector potential across any boundary are balanced [cf. e.g., 93]:

$$\left[\operatorname{grad} \boldsymbol{A}_\mathrm{b} - \operatorname{grad} \boldsymbol{A}_\mathrm{m}\right] \cdot \boldsymbol{n}_\mathrm{m} = \boldsymbol{0} \quad \text{on } \Gamma_\mathrm{m} \cap \Gamma_\mathrm{b} \, , \tag{5.23a}$$
$$\left[\operatorname{grad} \boldsymbol{A}_\mathrm{f} - \operatorname{grad} \boldsymbol{A}_\mathrm{m}\right] \cdot \boldsymbol{n}_\mathrm{m} = \boldsymbol{0} \quad \text{on } \Gamma_\mathrm{m} \setminus \Gamma_\mathrm{b} \, , \tag{5.23b}$$
$$\left[\operatorname{grad} \boldsymbol{A}_\mathrm{f} - \operatorname{grad} \boldsymbol{A}_\mathrm{b}\right] \cdot \boldsymbol{n}_\mathrm{b}^\mathrm{out} = \boldsymbol{0} \quad \text{on } \Gamma_\mathrm{b}^\mathrm{out} \, . \tag{5.23c}$$

A schematic illustration of the different regions and their interfaces is shown in Figure 5.3.

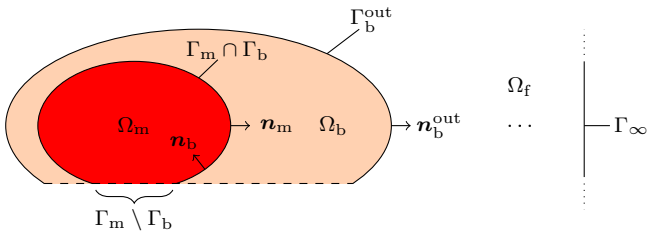

Figure 5.3: Schematic illustration of an arbitrary geometrical arrangement of muscle tissue Ω_m, the body region Ω_b, the surrounding space Ω_f, and its respective interfaces. Thereby, Γ_m denotes the muscle boundary with unit outward normal vector $\boldsymbol{n}_\mathrm{m}$, $\Gamma_\mathrm{b}^\mathrm{out}$ is the body surface with unit outward normal vector $\boldsymbol{n}_\mathrm{b}^\mathrm{out}$, Γ_b is an inner boundary of the body region with unit outward normal vector $\boldsymbol{n}_\mathrm{b}$ and Γ_∞ refers to the set of infinitely distant points.

5.3 Parameters for the Multi-Domain Model

The multi-domain model requires a set of parameters describing the electric tissue properties, the muscle's mesostructure, its microstructure, and the behaviour of the muscle fibre membranes. Measuring all model parameters for a single subject is currently impossible. However, the range of all parameters is well studied in the literature, and hence, one can expect meaningful predictions of EMG and MMG signals for virtual subjects closely approximating humans. A summary of all model parameters is given in Table 5.1.

Parameter	Symbol	Value	Reference
Longitudinal intracellular conductivity	$\sigma_\mathrm{i}^\mathrm{f}$	$8.93\,\mathrm{mS\,cm^{-1}}$	[21]
Transversal intracellular conductivity	$\sigma_\mathrm{i}^\mathrm{t}$	$0.0\,\mathrm{mS\,cm^{-1}}$	Assumption
Longitudinal extracellular conductivity	$\sigma_\mathrm{e}^\mathrm{f}$	$6.7\,\mathrm{mS\,cm^{-1}}$	[227]
Transversal extracellular conductivity	$\sigma_\mathrm{e}^\mathrm{t}$	$1.675\,\mathrm{mS\,cm^{-1}}$ to $3.35\,\mathrm{mS\,cm^{-1}}$	Assumption
Fat conductivity	σ_b	$0.4\,\mathrm{mS\,cm^{-1}}$	[227]
Membrane capacitance	C_m^k	$1\,\mathrm{\mu F\,cm^{-2}}$	[121]
Surface-to-volume ratio	A_m^k	Variable	
Motor unit density	f_r^k	Variable	
Magnetic permeability	μ_0	$4\pi \times 10^{-15}\,\mathrm{V\,s\,\mu A^{-1}\,cm^{-1}}$	Physical constant

Table 5.1: Summary of model parameters.

Macroscopically, muscle fibres can be considered as one-dimensional, cable-like objects. This implies ions can only flow along the muscle fibre direction within the intracellular domains. Accordingly, the longitudinal intracellular conductivity is chosen to be $\sigma_\mathrm{i}^\mathrm{f} = 8.93\,\mathrm{mS\,cm^{-1}}$ [cf. 21] and the transversal intracellular conductivity is set to $\sigma_\mathrm{i}^\mathrm{t} = 0.0\,\mathrm{mS\,cm^{-1}}$. Hence, the intracellular conductivity tensors for all motor units k (with $k \in \mathcal{M}_\mathrm{MU}$) are given by $\boldsymbol{\sigma}_\mathrm{i}^k = \sigma_\mathrm{i}^\mathrm{f}\, \boldsymbol{f} \otimes \boldsymbol{f}$. Thereby, $\boldsymbol{f}$ is a unit vector aligned with the muscle fibre direction in the actual configuration[1]. The conductivity of the extracellular domain is assumed to be in the same range as for the intracellular domains [227]. However, contrary to the intracellular domains, in the extracellular domain, ions can flow transverse to the muscle fibre direction [65] and the extracellular conductivity tensor is typically assumed to be anisotropic. Thereby, a wide range of anisotropy ratios has been reported in the literature [e.g., 84, 87]. This work assumes that the extracellular conductivity tensor is transversely isotropic and the anisotropy ratios are between 2 and 4. Following those assumption yields $\sigma_\mathrm{e}^\mathrm{f} = 6.7\,\mathrm{mS\,cm^{-1}}$ for the longitudinal extracellular conductivity and $\sigma_\mathrm{e}^\mathrm{t} = 1.675\,\mathrm{mS\,cm^{-1}}$ to $3.35\,\mathrm{mS\,cm^{-1}}$ for the transversal extracellular conductivity. Finally, the overall extracellular conductivity tensor can be summarised to read $\boldsymbol{\sigma}_\mathrm{e} = \sigma_\mathrm{e}^\mathrm{f}\, \boldsymbol{f} \otimes \boldsymbol{f} + \sigma_\mathrm{e}^\mathrm{t}\, (\boldsymbol{I} - \boldsymbol{f} \otimes \boldsymbol{f})$, where $\boldsymbol{I}$ is the second-order identity tensor. Further, the conductivity of fat tissue is assumed to be isotropic and much lower than the conductivity of the muscle tissue. Hence, the conductivity tensor in the body region is given by $\boldsymbol{\sigma}_\mathrm{b} = \sigma_\mathrm{b} \boldsymbol{I}$ with $\sigma_\mathrm{b} = 0.4\,\mathrm{mS\,cm^{-1}}$ [cf. 227].

To simulate the behaviour of the muscle fibre membranes, the electric circuit model of Hodgkin & Huxley [121] is utilised. Including a sodium conductance, a potassium conductance and a leakage conductance, it can be considered a basic model for describing the electric behaviour of the muscle fibre membranes. The implementation of the model equations was imported from the model repository of the Physiome Project[2] [155]. If another description of the skeletal muscle fibre membranes is desired, the membrane model can easily be replaced by any other suitable model. Depending on the desired application, a range of muscle fibre membrane models has incorporated different levels of detail [cf. e.g., 2, 27, 237].

[1] Especially when simulating muscle contractions, caution is required regarding the configuration in which physical quantities are described, i.e., in terms of referential or actual coordinates.

[2] https://models.physiomeproject.org/cellml

The fibre load of a motor unit and the area of a motor unit are determined by the mesoscale parameter f_{r}^{k}. Importantly, it is noted that those motor unit properties show considerable variability between different subjects as well as different muscles (see Section 2.3.3) and hence, the motor unit densities f_{r}^{k} ($\forall k \in \mathcal{M}_{\mathrm{MU}}$) need to be specified for each *in silico* experiment individually. Further, the radius of a muscle fibre is correlated to the properties of the innervating motor neuron [e.g., 53, 109]. Therefore, just as for the motor unit density parameter, the microscale membrane surface area per representative fibre-matrix cylinder volume A_{m}^{k} is specified for each simulation. Assuming that skeletal muscle tissue dominantly consists of muscle fibres and that the muscle fibres are ideal cylinders, the membrane surface per representative fibre-matrix cylinder volume can be approximated by $A_{\mathrm{m}}^{k} \approx 2/r^{k}$. Thereby, r^{k} is the average radius of a muscle fibre belonging to motor unit k. For example, given an average fibre radius of $r^{k} = 40\,\mu\mathrm{m}$ the corresponding membrane surface per representative fibre-matrix cylinder volume is $A_{\mathrm{m}}^{k} = 500\,\mathrm{cm}^{-1}$. Finally, it is noted that the vacuum permeability is given by $\mu_0 = 4\pi \times 10^{-15}\,\mathrm{V\,s\,\mu A^{-1}\,cm^{-1}}$.

6 Discretisation of the Multi-Domain Equations

No universal analytical solution exists for the mathematical model presented in Chapter 5. Hence, it is necessary to approximate the model equations numerically. Instead of solving all model equations monolithically, a staggered solution algorithm is derived in Section 6.1. This allows the application of specialised numerical methods to the individual sub-problems. Hence, in Section 6.2, the discretisation steps for approximating the muscle-induced electric potential fields are introduced. Further, in Section 6.3, the methods for predicting the corresponding magnetic field are derived. The resulting simulation framework is implemented in MATLAB (The MathWorks, Inc., Natick, Massachusetts, United States), and the code is hosted in a freely accessible git repository[1]. Section 6.4 demonstrates the convergence and consistency of the described computational model.

6.1 A Staggered Solution Scheme for Solving the Multi-Domain Model

One challenge for multiscale models is that the individual sub-models typically differ in their characteristic time and length scales. Hence, instead of solving all equations monolithically, using a staggered solution algorithm is often favourable. This enables one to use specialised solvers for each sub-problem. Specifically for the proposed multi-domain model, Equation (5.11b) includes a macroscopic diffusion term and a strongly non-linear microscopic reaction term, i.e., the ionic current I_{ion}^k. For reaction-diffusion equations, it is often convenient to first apply an operator splitting method before introducing a specific discretisation scheme [e.g., 215, 245, 263]. Hence, Equation (5.11b) is rewritten for obtaining

$$\frac{\partial V_{\text{m}}^k}{\partial t} \;=\; L_1 V_{\text{m}}^k \,+\, L_2 V_{\text{m}}^k \;,\; \forall k \in \mathcal{M}_{\text{MU}} \quad \text{in } \Omega_{\text{m}} \;. \tag{6.1}$$

Therein the differential operators L_1 and L_2 are defined such that

$$L_1 V_{\text{m}}^k = \; -\frac{1}{C_{\text{m}}^k}\, I_{\text{ion}}^k(\boldsymbol{y}^k, V_{\text{m}}^k, I_{\text{stim}}^k) \;, \tag{6.2a}$$

$$L_2 V_{\text{m}}^k = \; \frac{1}{C_{\text{m}}^k A_{\text{m}}^k}\, \text{div}\left[\boldsymbol{\sigma}_{\text{i}}^k \,\text{grad}\left(V_{\text{m}}^k + \phi_{\text{e}}\right)\right] \;. \tag{6.2b}$$

Now, an approximated solution for Equation (5.11b) can be obtained by subsequently integrating Equation (6.2a) and Equation (6.2b). Thereby, the transmembrane potential V_{m}^k ($\forall\, k \in \mathcal{M}_{\text{MU}}$) is iteratively updated after each integration step. This algorithm yields a splitting error acceptable for sufficiently small time steps. Employing a first-order accurate Godunov-type splitting [cf. e.g., 148, 243], the multi-domain model can be solved by the following multi-step solution scheme:

(i.) For $t_n < t \leq t_n + \Delta t$ solve for each motor unit $k \in \mathcal{M}_{\text{MU}}$ the system of ordinary differential

[1] https://bitbucket.org/klotz_t/multi_domain_fd_code

equations

$$\frac{\partial V_\mathrm{m}^k}{\partial t} = -\frac{1}{C_\mathrm{m}^k} I_\mathrm{ion}^k(\boldsymbol{y}^k, V_\mathrm{m}^k) \quad \text{in } \Omega_\mathrm{m} \ , \tag{6.3a}$$

$$\frac{\partial \boldsymbol{y}^k}{\partial t} = \boldsymbol{g}^k(\boldsymbol{y}^k, V_\mathrm{m}^k) \quad \text{in } \Omega_\mathrm{m} \ . \tag{6.3b}$$

(ii.) Using the approximated solution for V_m^k from step (i.) as an initial condition, solve for $t_n < t \leq t_n + \Delta t$ the coupled system of partial differential equations and corresponding boundary conditions given by

$$\frac{\partial V_\mathrm{m}^k}{\partial t} = \frac{1}{C_\mathrm{m}^k A_\mathrm{m}^k} \operatorname{div}\left[\boldsymbol{\sigma}_\mathrm{i}^k \operatorname{grad}\left(V_\mathrm{m}^k + \phi_\mathrm{e}\right)\right] \ , \ \forall k \in \mathcal{M}_\mathrm{MU} \quad \text{in } \Omega_\mathrm{m} \ , \tag{6.4a}$$

$$0 = \operatorname{div}\left[\boldsymbol{\sigma}_\mathrm{e} \operatorname{grad} \phi_\mathrm{e}\right] + \sum_{k=1}^{N} f_\mathrm{r}^k \operatorname{div}\left[\boldsymbol{\sigma}_\mathrm{i}^k \operatorname{grad}\left(V_\mathrm{m}^k + \phi_\mathrm{e}\right)\right] \quad \text{in } \Omega_\mathrm{m} \ , \tag{6.4b}$$

$$0 = \operatorname{div}\left[\boldsymbol{\sigma}_\mathrm{b} \operatorname{grad} \phi_\mathrm{b}\right] \quad \text{in } \Omega_\mathrm{b} \ , \tag{6.4c}$$

$$0 = \left[\boldsymbol{\sigma}_\mathrm{i}^k \operatorname{grad} V_\mathrm{m}^k + \boldsymbol{\sigma}_\mathrm{i}^k \operatorname{grad} \phi_\mathrm{e}\right] \cdot \boldsymbol{n}_\mathrm{m} \ , \ \forall k \in \mathcal{M}_\mathrm{MU} \quad \text{on } \Gamma_\mathrm{m} \ , \tag{6.4d}$$

$$0 = \left[\boldsymbol{\sigma}_\mathrm{e} \operatorname{grad} \phi_\mathrm{e}\right] \cdot \boldsymbol{n}_\mathrm{m} \quad \text{on } \Gamma_\mathrm{m} \setminus \Gamma_\mathrm{b} \ , \tag{6.4e}$$

$$0 = \left[\boldsymbol{\sigma}_\mathrm{b} \operatorname{grad} \phi_\mathrm{b}\right] \cdot \boldsymbol{n}_\mathrm{b}^\mathrm{out} \quad \text{on } \Gamma_\mathrm{b}^\mathrm{out} \ , \tag{6.4f}$$

$$0 = \left[\boldsymbol{\sigma}_\mathrm{e} \operatorname{grad} \phi_\mathrm{e} - \boldsymbol{\sigma}_\mathrm{b} \operatorname{grad} \phi_\mathrm{b}\right] \cdot \boldsymbol{n}_\mathrm{m} \quad \text{on } \Gamma_\mathrm{m} \cap \Gamma_\mathrm{b} \ , \tag{6.4g}$$

$$0 = \phi_\mathrm{e} - \phi_\mathrm{b} \quad \text{on } \Gamma_\mathrm{m} \cap \Gamma_\mathrm{b} \ . \tag{6.4h}$$

(iii.) The quasi-static approximation decouples the electric field problem from the magnetic field problem. Hence, for each global time step of the splitting scheme, the magnetic vector potential can be computed by solving

$$\operatorname{div}(\operatorname{grad} \boldsymbol{A}) = -\mu_0 \left(\boldsymbol{\sigma}_\mathrm{e} \operatorname{grad} \phi_\mathrm{e} + \sum_{k=1}^{N} f_\mathrm{r}^k \boldsymbol{\sigma}_\mathrm{i}^k \operatorname{grad}(V_\mathrm{m}^k + \phi_\mathrm{e})\right) \quad \text{in } \Omega_\mathrm{m} \ , \tag{6.5a}$$

$$\operatorname{div}(\operatorname{grad} \boldsymbol{A}) = -\mu_0 \left[\boldsymbol{\sigma}_\mathrm{b} \operatorname{grad} \phi_\mathrm{b}\right] \quad \text{in } \Omega_\mathrm{b} \ , \tag{6.5b}$$

$$\operatorname{div}(\operatorname{grad} \boldsymbol{A}) = \boldsymbol{0} \quad \text{in } \Omega_\mathrm{f} \ , \tag{6.5c}$$

$$\boldsymbol{A} = \boldsymbol{0} \quad \text{on } \Gamma_\infty \ , \tag{6.5d}$$

$$\boldsymbol{A}_\mathrm{m} - \boldsymbol{A}_\mathrm{b} = \boldsymbol{0} \quad \text{on } \Gamma_\mathrm{m} \cap \Gamma_\mathrm{b} \ , \tag{6.5e}$$

$$\boldsymbol{A}_\mathrm{m} - \boldsymbol{A}_\mathrm{f} = \boldsymbol{0} \quad \text{on } \Gamma_\mathrm{m} \setminus \Gamma_\mathrm{b} \ , \tag{6.5f}$$

$$\boldsymbol{A}_\mathrm{b} - \boldsymbol{A}_\mathrm{f} = \boldsymbol{0} \quad \text{on } \Gamma_\mathrm{b}^\mathrm{out} \ , \tag{6.5g}$$

$$\left[\operatorname{grad} \boldsymbol{A}_\mathrm{b} - \operatorname{grad} \boldsymbol{A}_\mathrm{m}\right] \cdot \boldsymbol{n}_\mathrm{m} = \boldsymbol{0} \ , \quad \text{on } \Gamma_\mathrm{m} \cap \Gamma_\mathrm{b} \ , \tag{6.5h}$$

$$\left[\operatorname{grad} \boldsymbol{A}_\mathrm{f} - \operatorname{grad} \boldsymbol{A}_\mathrm{m}\right] \cdot \boldsymbol{n}_\mathrm{m} = \boldsymbol{0} \ , \quad \text{on } \Gamma_\mathrm{m} \setminus \Gamma_\mathrm{b} \ , \tag{6.5i}$$

$$\left[\operatorname{grad} \boldsymbol{A}_\mathrm{f} - \operatorname{grad} \boldsymbol{A}_\mathrm{b}\right] \cdot \boldsymbol{n}_\mathrm{b}^\mathrm{out} = \boldsymbol{0} \ , \quad \text{on } \Gamma_\mathrm{b}^\mathrm{out} \ . \tag{6.5j}$$

(iv.) Calculate the magnetic field $\boldsymbol{B}$ for each time step via

$$\boldsymbol{B} = \operatorname{curl} \boldsymbol{A} \ . \tag{6.6}$$

Therein, Δt denotes the global time step size of the overall solution scheme. The specific methods for solving step (i.), as well as step (ii.), are introduced in Section 6.2 and the methods for solving step (iii.) as well as step (iv.) are described in Section 6.3. Notably, this general solution algorithm (see Figure 6.1) allows the utilisation of different temporal and spatial discretisations in each sub-step.

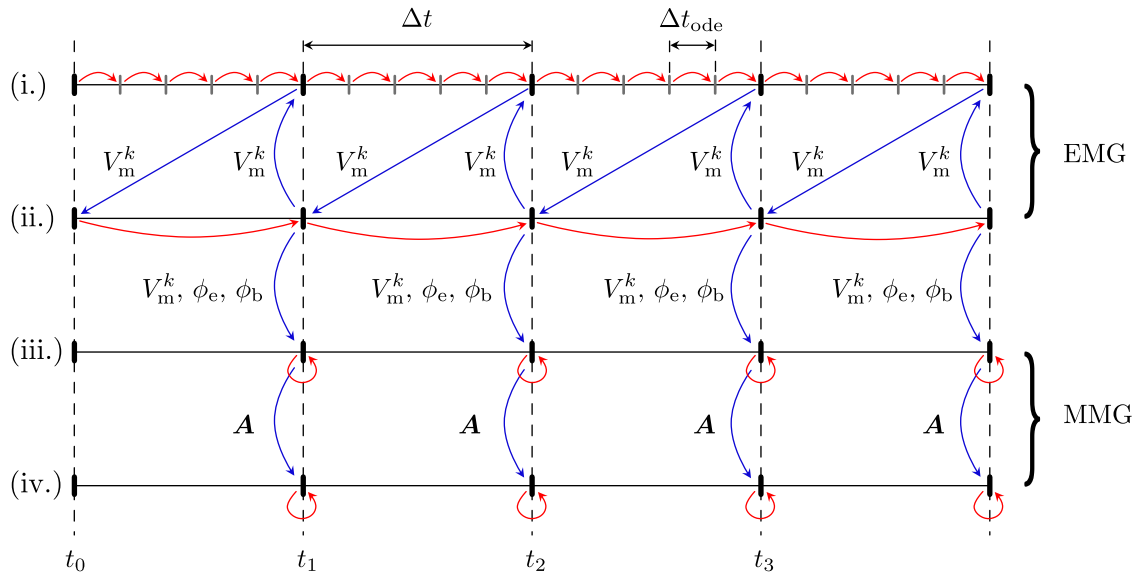

Figure 6.1: Schematic illustration of the utilised staggered solution scheme. Therein, red arrows represent solution steps, and blue arrows indicate variables exchanged between the sub-problems.

6.2 Solving for the Electric Potential Fields

Following the general solution scheme presented in Section 6.1, this section describes the numerical methods for solving the electric field problem, i.e., step (i.) and step (ii.). Therefore, the spatial derivatives are approximated by finite differences. Hence, the continuous body, i.e., the muscle region Ω_{m} and the body domain Ω_{b}, needs to be represented by a discrete set of points. Within this work, idealised cube-shaped tissue samples are simulated, which can be discretised by a rectangular grid of uniformly spaced discrete points.

6.2.1 Solving for the Membrane Dynamics

Step (i.) requires to solve the system of stiff ordinary equations given by Equation (6.3a) and Equation (6.3b) for $t_n < t \leq t_n + \Delta t$. This is achieved by utilising an improved Euler method [cf. e.g., 16] with a fixed time step size. Hence, for each discretisation point and each intracellular domain $k \in \mathcal{M}_{\mathrm{MU}}$ in the muscle region, the following explicit solution scheme is applied:

$$\begin{pmatrix} V_{\mathrm{m}}^k \\ \boldsymbol{y}^k \end{pmatrix}^{p+1} = \begin{pmatrix} V_{\mathrm{m}}^k \\ \boldsymbol{y}^k \end{pmatrix}^{p} + \frac{\Delta t_{\mathrm{ode}}}{2} \left[\begin{pmatrix} -\frac{I_{\mathrm{ion}}^k(\boldsymbol{y}^k, V_{\mathrm{m}}^k)}{C_{\mathrm{m}}^k} \\ \boldsymbol{g}^k(\boldsymbol{y}^k, V_{\mathrm{m}}^k) \end{pmatrix}^{p} + \begin{pmatrix} -\frac{I_{\mathrm{ion}}^k(\boldsymbol{y}^k, V_{\mathrm{m}}^k)}{C_{\mathrm{m}}^k} \\ \boldsymbol{g}^k(\boldsymbol{y}^k, V_{\mathrm{m}}^k) \end{pmatrix}^{q} \right] . \tag{6.7}$$

The superscript p refers to a (discrete) time frame in the interval $[t_n,\ t_n + \Delta t]$. Further, the superscript q refers to an intermediate time frame obtained from

$$\begin{pmatrix} V_{\mathrm{m}}^k \\ \boldsymbol{y}^k \end{pmatrix}^{q} = \begin{pmatrix} V_{\mathrm{m}}^k \\ \boldsymbol{y}^k \end{pmatrix}^{p} + \Delta t_{\mathrm{ode}} \begin{pmatrix} -\frac{I_{\mathrm{ion}}^k(\boldsymbol{y}^k, V_{\mathrm{m}}^k)}{C_{\mathrm{m}}^k} \\ \boldsymbol{g}^k(\boldsymbol{y}^k, V_{\mathrm{m}}^k) \end{pmatrix}^{p} . \tag{6.8}$$

Note that this is equivalent to a forward Euler step, which is used as an estimate for the temporal derivative at $t = t^p + \Delta t_{\mathrm{ode}}$. Further, it is noted that the time step sizes are chosen such that Δt and Δt_{ode} can be related by a natural number.

6.2.2 Solving for the Spatial Distribution of the Electric Potential Fields

Step (ii.) requires to approximate a solution for Equations (6.4a) to (6.4h), i.e., a coupled diffusion problem. Therefore, a first-order finite difference discretises the temporal derivative on the left-hand side of Equation (6.4a). The step size equals the global time step of the splitting scheme Δt. Further, the spatial derivatives on the right-hand side of Equation (6.4a) are approximated by second-order accurate central finite differences, which are evaluated at $t = t_n + \Delta t$. Hence, we use a backward Euler method. Analogously, the right-hand side terms of Equation (6.4b) to (6.4h) are also evaluated at $t = t_n + \Delta t$. Thereby, the second spatial derivatives in Equations (6.4b) and (6.4c) are approximated by second-order accurate central finite differences. The first spatial derivatives in Equations (6.4d) to (6.4g) are approximated with second-order accurate forward or backward finite differences. Following these discretisation steps yields a linear system, i.e.,

$$\left(\frac{1}{\Delta t}\boldsymbol{M} - \bar{\boldsymbol{K}}\right)\boldsymbol{u}_{\mathrm{e}}^{n+1} \;=\; \frac{1}{\Delta t}\boldsymbol{M}\boldsymbol{u}_{\mathrm{e}}^{n}\;. \tag{6.9}$$

Therein, $\boldsymbol{u}_{\mathrm{e}}^{n}$ is a vector summarising the electric potential fields in all domains at a discrete time frame $t = t_n$. Hence, it contains the transmembrane potentials as well as the extracellular potential for all discrete points within the muscle region and the body potential for every discrete point in the body region, i.e.,

$$\boldsymbol{u}_{\mathrm{e}}^{n} \;=\; \left[\boldsymbol{V}_{\mathrm{m}}^{1,n}, ..., \boldsymbol{V}_{\mathrm{m}}^{N,n}, \boldsymbol{\Phi}_{\mathrm{e}}^{n}, \boldsymbol{\Phi}_{\mathrm{b}}^{n}\right]^{T}\;. \tag{6.10}$$

Further, $\bar{\boldsymbol{K}}$ is a block matrix, i.e.,

$$\bar{\boldsymbol{K}} \;=\; \left(\begin{array}{ccc|c|c} \bar{\boldsymbol{K}}_{1,1} & & & \bar{\boldsymbol{K}}_{1}^{N+1} & \\ & \ddots & & \vdots & \\ & & \bar{\boldsymbol{K}}_{N,N} & \bar{\boldsymbol{K}}_{N}^{N+1} & \\ \hline \bar{\boldsymbol{K}}_{N+1,1} & \cdots & \bar{\boldsymbol{K}}_{N+1,N} & \bar{\boldsymbol{K}}_{N+1,N+1} & \bar{\boldsymbol{K}}_{N+1,N+2} \\ \hline & & & \bar{\boldsymbol{K}}_{N+2,N+1} & \bar{\boldsymbol{K}}_{N+2,N+2} \end{array}\right)\;, \tag{6.11}$$

where the sub-matrices $\bar{\boldsymbol{K}}_{i,j}$ correspond to the discrete differential operators given on the right-hand side of Equations (6.4a) to (6.4h). Finally, the block matrix

$$\boldsymbol{M} \;=\; \left(\begin{array}{ccc|c|c} \boldsymbol{M}_1 & & & & \\ & \ddots & & & \\ & & \boldsymbol{M}_N & & \\ \hline & & & \boldsymbol{0} & \\ \hline & & & & \boldsymbol{0} \end{array}\right) \tag{6.12}$$

is a linear operator equivalent to the discrete version of the left-hand sides of Equation (6.4a). The linear system specified by Equations (6.9) to (6.12) is solved with MATLAB's built-in GMRES function [229]. The linear system is preconditioned by an incomplete LU factorisation (crout version, drop tolerance: 10^{-6}), and the following solver options are applied: an absolute and relative tolerance of 10^{-10}, restart after 20 inner iterations and a maximum number of 20 outer iterations.

6.3 Solving for the Magnetic Field

Assuming quasi-static conditions, the magnetic field can be predicted for each time step based on the electric potential fields in the muscle and the body region. This is achieved by deriving a solution to compute the magnetic vector potential $\boldsymbol{A}$. The result is the basis for finally computing the magnetic field $\boldsymbol{B}$.

6.3.1 Solving for the Magnetic Vector Potential

The system of Equations given by (6.5a) to (6.5j) describes three independent Poisson equations with vanishing potential at infinite distance from the current source. This mathematical problem can be solved using Green's function [e.g., 7], i.e., the impulse response of a specific boundary value problem defined by an inhomogeneous linear differential operator. In short, let

$$Lu(\boldsymbol{x}) \;=\; f(\boldsymbol{x}) \;\text{ in } \Omega \tag{6.13}$$

describe an arbitrary differential equation defined on a region Ω. Therein, L is a linear differential operator, $u(\boldsymbol{x})$ is a solution to the given boundary value problem, and $f(\boldsymbol{x})$ is the right-hand side of the differential equation. A Green's function $G(\boldsymbol{r}, \boldsymbol{r}')$ is a solution of the differential equation

$$L\,G(\boldsymbol{r}, \boldsymbol{r}') \;=\; \delta(\boldsymbol{r} - \boldsymbol{r}')\;, \tag{6.14}$$

where $\delta(*)$ is the Dirac delta function. Thereby, coordinates $\boldsymbol{r}$ denote field points and $\boldsymbol{r}'$ denote source points. If a Green's function exists for a given boundary value problem, a solution can be computed by exploiting the linearity of the problem. In detail, the solution of the differential equation can be calculated by evaluating the volume integral of Green's function multiplied by the right-hand side of the equation, i.e.,

$$u(\boldsymbol{x}) \;=\; \iiint_V G(\boldsymbol{r}, \boldsymbol{r}') f(\boldsymbol{x}) \mathrm{d}V\;. \tag{6.15}$$

For a Poisson equation with vanishing potential at infinity, the Green's function is [cf. e.g., 7]

$$G(\boldsymbol{r}, \boldsymbol{r}') \;=\; \frac{1}{4\pi} \frac{1}{|\boldsymbol{r} - \boldsymbol{r}'|}\;. \tag{6.16}$$

Accordingly, the magnetic vector potential at an observation point $\boldsymbol{r}$ can be computed by [cf. e.g., 93]

$$\boldsymbol{A}(\boldsymbol{r}) \;=\; \iiint_V G(\boldsymbol{r}, \boldsymbol{r}') \Big(\mu_0 \boldsymbol{j}(\boldsymbol{r}')\Big)\, \mathrm{d}V \;=\; \frac{\mu_0}{4\pi} \iiint_V \frac{\boldsymbol{j}(\boldsymbol{r}')}{|\boldsymbol{r} - \boldsymbol{r}'|}\, \mathrm{d}V\;. \tag{6.17}$$

Thereby, the volume integral needs to be evaluated for the whole simulated tissue sample, i.e., $\Omega_\mathrm{m} \cup \Omega_\mathrm{b}$, for which the current density is given by

$$\boldsymbol{j} \;=\; \begin{cases} \boldsymbol{\sigma}_\mathrm{e} \operatorname{grad} \phi_\mathrm{e} \;+\; \displaystyle\sum_{k=1}^{N} f_\mathrm{r}^k \boldsymbol{\sigma}_\mathrm{i}^k \operatorname{grad}(V_\mathrm{m}^k + \phi_\mathrm{e}) & \text{in } \Omega_\mathrm{m} \\ \boldsymbol{\sigma}_\mathrm{b} \operatorname{grad} \phi_\mathrm{b} & \text{in } \Omega_\mathrm{b}\;. \end{cases} \tag{6.18}$$

6.3.2 Computing the Magnetic Field

Given the solution for the magnetic vector potential, i.e., Equation (6.17), the magnetic field $\boldsymbol{B}$ can be computed by a series of vector calculus operations:

$$\begin{aligned}
\boldsymbol{B}(\boldsymbol{r}) &= \operatorname{curl} \boldsymbol{A} \\
\Leftrightarrow \boldsymbol{B}(\boldsymbol{r}) &= \operatorname{curl}\left(\frac{\mu_0}{4\pi} \iiint_V \frac{\boldsymbol{j}(\boldsymbol{r}')}{|\boldsymbol{r}-\boldsymbol{r}'|}\,\mathrm{d}V\right) \\
\Leftrightarrow \boldsymbol{B}(\boldsymbol{r}) &= \frac{\mu_0}{4\pi} \iiint_V \operatorname{curl}\left(\frac{\boldsymbol{j}(\boldsymbol{r}')}{|\boldsymbol{r}-\boldsymbol{r}'|}\right)\mathrm{d}V \\
\Leftrightarrow \boldsymbol{B}(\boldsymbol{r}) &= \frac{\mu_0}{4\pi} \iiint_V \left[\frac{1}{|\boldsymbol{r}-\boldsymbol{r}'|}\operatorname{curl}\left(\boldsymbol{j}(\boldsymbol{r}')\right) - \boldsymbol{j}(\boldsymbol{r}') \times \operatorname{grad}\left(\frac{1}{|\boldsymbol{r}-\boldsymbol{r}'|}\right)\right]\mathrm{d}V \\
\Leftrightarrow \boldsymbol{B}(\boldsymbol{r}) &= \frac{\mu_0}{4\pi} \iiint_V -\boldsymbol{j}(\boldsymbol{r}') \times \operatorname{grad}\left(\frac{1}{|\boldsymbol{r}-\boldsymbol{r}'|}\right)\mathrm{d}V \\
\Leftrightarrow \boldsymbol{B}(\boldsymbol{r}) &= \frac{\mu_0}{4\pi} \iiint_V \frac{\boldsymbol{j}(\boldsymbol{r}') \times (\boldsymbol{r}-\boldsymbol{r}')}{|\boldsymbol{r}-\boldsymbol{r}'|^3}\,\mathrm{d}V\ .
\end{aligned} \tag{6.19}$$

Equation 6.19 is known as the Biot-Savard law [e.g., 93]. For the derivation, one makes use of the product rule of the curl operator, i.e.,

$$\operatorname{curl}(\varphi \boldsymbol{F}) = \varphi \operatorname{curl}(\boldsymbol{F}) - \boldsymbol{F} \times \operatorname{grad}(\varphi)\ . \tag{6.20}$$

Therein, φ denotes an arbitrary scalar field and $\boldsymbol{F}$ an arbitrary vector field. Moreover, it is utilised that the curl of the current density vector with respect to the source vector is zero [93]. The numerical solution of the Biot-Savard law requires computing the current densities given in Equation (6.18). Therefore, the spatial derivatives of the electric potentials are approximated utilising second-order accurate central finite differences. Moreover, the volume integral is approximated by the three-dimensional trapezoidal rule. This discretisation can be expressed in terms of a series of matrix-vector multiplications. In detail, component i ($i = 1, 2, 3$) of the current density at the discrete time frame n is given by

$$\boldsymbol{u}_{\mathrm{j}}^{i,n} = \left[\boldsymbol{D}_1^i \ \cdots \ \boldsymbol{D}_N^i \ \boldsymbol{D}_{N+1}^i \ \boldsymbol{D}_{N+2}^i\right]\boldsymbol{u}_{\mathrm{e}}^n\ , \tag{6.21}$$

where the matrices $\boldsymbol{D}_k^i$ are the discrete differential operators of Equation (6.18). Next, each magnetic field component i ($i = 1, 2, 3$) is computed by

$$\boldsymbol{u}_{\mathrm{b}}^{1,n} = \boldsymbol{L}^3 \boldsymbol{u}_{\mathrm{j}}^{2,n} - \boldsymbol{L}^2 \boldsymbol{u}_{\mathrm{j}}^{3,n}\ , \tag{6.22a}$$

$$\boldsymbol{u}_{\mathrm{b}}^{2,n} = \boldsymbol{L}^1 \boldsymbol{u}_{\mathrm{j}}^{3,n} - \boldsymbol{L}^3 \boldsymbol{u}_{\mathrm{j}}^{1,n}\ , \tag{6.22b}$$

$$\boldsymbol{u}_{\mathrm{b}}^{3,n} = \boldsymbol{L}^2 \boldsymbol{u}_{\mathrm{j}}^{1,n} - \boldsymbol{L}^1 \boldsymbol{u}_{\mathrm{j}}^{2,n}\ . \tag{6.22c}$$

Therein, the matrices $\boldsymbol{L}^i$ ($i = 1, 2, 3$) numerically evaluate the integral given in Equation 6.19. From a physical point of view, the matrices $\boldsymbol{L}^i$ relate the contribution of a unit source at location $\boldsymbol{r}'$ to the field observed at a point $\boldsymbol{r}$. Hence, the matrices $\boldsymbol{L}^i$ are also known as lead-field matrices [e.g., 163].

6.4 Convergence Analysis

To demonstrate the consistency of the numerical solution schemes presented in Sections 6.1 to 6.3, this section comprises a set of convergence studies.

6.4.1 The Temporal Discretisation Error Associated with the Membrane Models

First, the explicit method for solving the system of stiff ordinary equations describing the membrane dynamics, i.e., Equations (6.3a) and (6.3b), is investigated. Hence, an action potential is simulated for a single muscle fibre membrane model, cf. Section 4.1.2. This is achieved by perturbing the transmembrane potential from $-75\,\mathrm{mV}$ to $-60\,\mathrm{mV}$, i.e., representing the initial condition. Further, the duration of the simulated time interval is 20 ms. For testing the convergence of the numerical solution scheme, five different time step sizes are considered, i.e., 5×10^{-5} ms to 1×10^{-2} ms. The solution obtained from the finest discretisation is defined as the reference solution and used to estimate the error for all other time step sizes. Figure 6.2A shows that the relative discretisation error monotonically decreases with decreasing time step size. Applying a linear regression to the data points in the log-log plot yields a slope of 1.08.

6.4.2 The Spatial Discretisation Error of the Coupled Diffusion Problem

Second, the spatial discretisation error associated with solving the coupled diffusion problem given by Equation (6.4a) to (6.4h) is examined. Therefore, a cube-shaped muscle sample with edge lengths $L = 40\,\mathrm{mm}$, $W = 20\,\mathrm{mm}$ and $H = 20\,\mathrm{mm}$ is simulated. Further, the thickness of the subcutaneous fat is set to 4 mm. This tissue sample is discretised with four uniform grid spacings, i.e., 0.25 mm, 0.5 mm, 1 mm and 2 mm. The global time step size Δt is set to 0.1 ms, and the muscle is assumed to consist of a single motor unit. As a test scenario, the transmembrane potential at the centre point of the muscle is perturbed from $-75\,\mathrm{mV}$, i.e., the resting potential, to 0 mV. The solution vector is computed for each spatial discretisation for one isolated time step using this initial condition. As in the previous example, the solution obtained from the finest discretisation is the reference solution. Figure 6.2B shows that the relative discretisation error monotonically decreases with decreasing grid point spacing. In detail, for a linear regression model, the slope in the log-log plot is 2.90.

6.4.3 The Splitting Error

Third, the error introduced by the operator splitting method is estimated. Therefore, a cube-shaped muscle with edge lengths $L = 20\,\mathrm{mm}$, $W = 10\,\mathrm{mm}$ and $H = 10\,\mathrm{mm}$ as well as a 2 mm thick subcutaneous fat tissue layer is simulated. The muscle is assumed to consist of a single motor unit, and the intracellular domain is stimulated by applying a current pulse with an amplitude of $700\,\mathrm{mA\,cm^{-2}}$ and a duration of 0.1 ms to the centre point of the muscle. The spatial discretisation utilises equidistant grid points with a spacing of 0.5 mm. Further, the step size for solving the membrane models, i.e., Δt_{ode}, is set to 0.001 ms. The error associated with the splitting scheme is computed by varying the global time step size Δt, i.e., 0.005 ms, 0.01 ms, 0.05 ms and 0.1 ms. Thereby, the result obtained from the finest discretisation is defined as the reference solution. Figure 6.2C shows the relative splitting error when solving the described test problem in the interval $0\,\mathrm{ms} \leq t \leq 0.4\,\mathrm{ms}$ in dependence of the global time step size Δt. One can observe that the splitting error is negatively correlated with the time step size, and a linear regression with a slope of 1.13 can be fitted to all data points in the log-log plot.

6.4.4 The Spatial Discretisation Error of the Magnetic Field Problem

Finally, the error associated with predicting the magnetic field is computed. Therefore, a cube-shaped tissue geometry with edge lengths $L = 10\,\mathrm{mm}$, $W = 20\,\mathrm{mm}$ and $H = 20\,\mathrm{mm}$ is considered. It is assumed that the current density along a line parallel to the shortest edge of the sample and centred within the sample is $\boldsymbol{j} = 100\,\mu\mathrm{A\,cm^{-2}}\,\mathbf{f}$. Therein, $\mathbf{f}$ is a unit vector parallel to the shortest edge of the cuboid. Further, the current density is zero for all other discretisation

points. For estimating the spatial discretisation error, the described problem is simulated for four different grid spacings, i.e., 0.25 mm, 0.5 mm, 1 mm and 2 mm. It can be seen from Figure 6.2D that the discretisation error negatively correlates with the grid point spacing. That is, the slope of a linear regression in a log-log plot is 2.39.

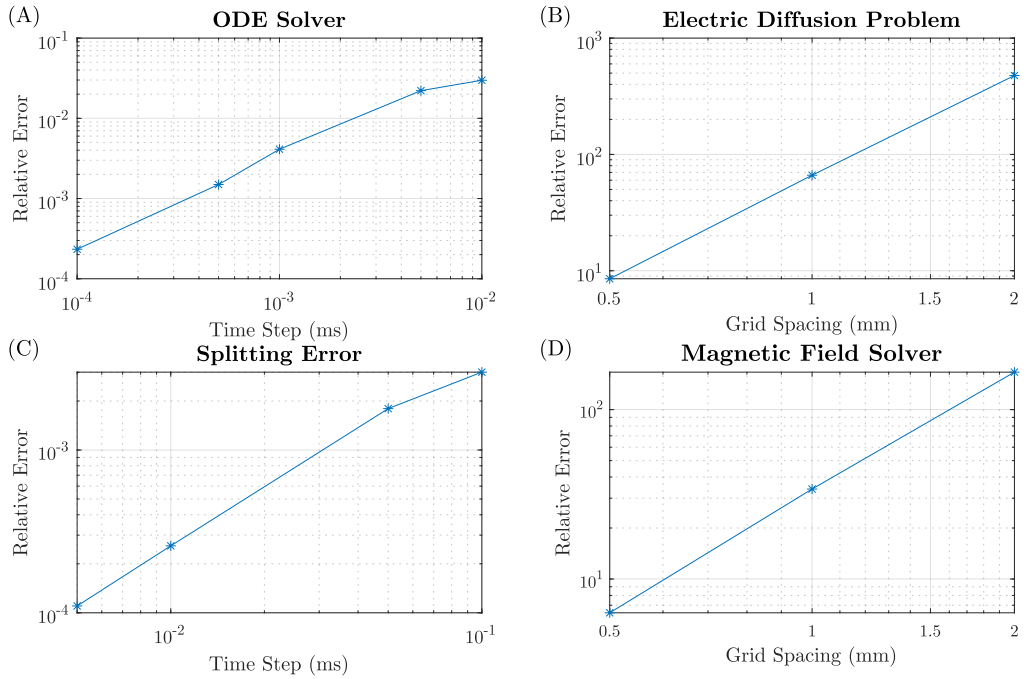

Figure 6.2: (A) Relative error of the transmembrane potential depending on the time step size when solving a single membrane model. (B) Relative error of the electric solution vector $\boldsymbol{u}_{\mathrm{e}}^{n}$ when solving the coupled diffusion problem for a single time step with different grid spacings. (C) Relative error of the electric solution vector $\boldsymbol{u}_{\mathrm{e}}^{n}$ when varying the global time step of the operator splitting method. After triggering an action potential, the simulation captures a time interval of 0.4 ms. (D) Relative error of the magnetic solution vector $\boldsymbol{u}_{\mathrm{b}}^{n}$ for a given current distribution in dependence of the grid spacing.

Part III

In Silico Experiments

7 The Fundamental Properties of EMG and MMG Signals

Artificially evoked contractions (e.g., electric stimulation or through reflexes) yield the synchronised activity of several muscle fibres. Hence, the corresponding EMG or MMG signals are considerably easier to understand than signals of voluntary contractions. However, one cannot control all relevant system parameters experimentally. This chapter systematically investigates simulated compound muscle responses, i.e., the EMG or MMG generated by the synchronous activity of several muscle fibres, for idealised fusiform muscles. Thereby, a compound muscle electric potential[1] describes the signal observable using EMG, and a compound muscle magnetic field represents the corresponding MMG signal. The conducted *in silico* experiments are described in Section 7.1. Given the simulated signals, Section 7.2 exemplarily investigates the temporal properties of compound muscle electric potentials and compound muscle magnetic fields observed from a single electrode or magnetometer. Further, in Section 7.3, the spatiotemporal properties of muscle-induced bioelectromagnetic fields are examined by considering high-density EMG and high-density MMG signals. Finally, Section 7.4 exploits the simulation environment to predict the relevance of different currents for measurable MMG signal.

7.1 In Silico Experiments

The *in silico* experiments presented in this chapter use the simulation framework introduced in Part II to systematically investigate compound muscle electric potentials and compound muscle magnetic fields. That is the influence of the number of active muscle fibres, the properties of the recruited muscle fibres, the distance between the active fibres and the detection system, and the electric tissue properties. This section introduces the corresponding *in silico* experiments.

7.1.1 Tissue Geometry, Stimulation Protocol and Discretisation

For excluding the influence of complex muscle geometries, a cube-shaped, fusiform muscle with edge lengths $L = 60\,\text{mm}$, $W = 15\,\text{mm}$ and $H = 20\,\text{mm}$ is considered. It is assumed that the muscle fibres are aligned with the longest edge of the tissue sample. Moreover, the simulated tissue sample can have a subcutaneous fat layer of varying thickness (see Figure 7.1). The simulations are described in a coordinate system inspired by the muscle's morphology. A unique (orthogonal) coordinate system can be obtained by choosing two orthogonal reference directions. That is the muscle fibre direction and the body surface's normal vector. Hence, as shown in Figure 7.1, the $x_\text{f}^\parallel$-direction is aligned with the muscle fibres and parallel to the body surface, the $x_\text{t}^\parallel$-direction is perpendicular to the muscle fibres and parallel to the muscle surface, and the $x_\text{t}^\perp$-direction is perpendicular to the muscle fibres and normal to the body surface.

[1] In the literature, compound muscle electric potentials are also referred to as compound muscle potentials or compound muscle action potentials. This work chooses compound muscle electric potential as it unambiguously refers to the measured physical field. Within this work, this is particularly relevant to distinguish EMG and MMG measurements. A compound muscle magnetic field denotes the corresponding MMG signal following this argument. Accordingly, the term compound muscle response includes all muscle-induced bio-signals.

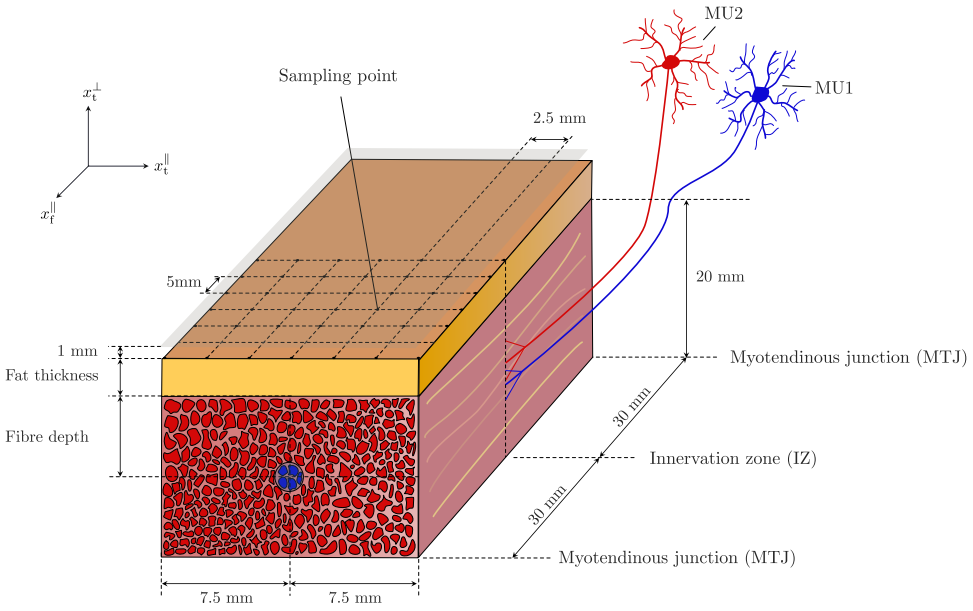

Figure 7.1: Schematic drawing illustrating the simulated tissue geometry, whereby muscle and fat tissue are coloured in red and yellow, respectively. The muscle fibres are aligned with the $x_1^{\parallel}$-direction. The sampling points illustrate a high-density EMG array. The virtual MMG array is shifted by 1 mm above the body surface (indicated by the transparent plane).

A series of simulations were conducted to investigate how the distance between active muscle fibres and the detection system affects the results. The muscle was activated by selectively stimulating muscle fibres at different depths, namely $d_{\text{fibre}} = 3\,\text{mm}$, $5\,\text{mm}$, $7\,\text{mm}$ and $9\,\text{mm}$, and centred in the $x_{\text{t}}^{\parallel}$ direction. This is achieved by functionally subdividing the virtual muscle into two motor units. All recruited fibres are grouped into the first motor unit, i.e., MU1. The territory of MU1 comprises all skeletal muscle material points with the cross-sectional coordinates $x_{\text{t}}^{\parallel} = 0\,\text{mm}$ and $x_{\text{t}}^{\perp} = 20\,\text{mm} - d_{\text{fibre}}$. If not noted otherwise, the motor unit volume fraction of MU1 is $f_{\text{r}}^{1} = 1$. The territory of the second motor unit, i.e., MU2, is chosen such that Equation (5.5) holds for each skeletal muscle material point. MU1 is stimulated by applying a current pulse with an amplitude of $700\,\text{mA}\,\text{cm}^{-2}$ and a duration of $0.1\,\text{ms}$ to the respective intracellular domain at the innervation zone. Further, three subcutaneous fat tissue layers with thicknesses of $0\,\text{mm}$, $2\,\text{mm}$ and $4\,\text{mm}$ are considered for studying the influence of fat. As baseline parametrisation the surface-to-volume ratio of the muscle fibres is $A_{\text{m}}^{k} = 250\,\text{cm}^{-1}$ ($k = 1, 2$), i.e., corresponding to a muscle fibre radius of $80\,\mu\text{m}$. The anisotropy ratio of the extracellular conductivity tensor is 2. All other model parameters are directly adopted from Table 5.1.

For the discretisation of the computational model, the global time step Δt is set to $0.1\,\text{ms}$. Further, the time step for solving the membrane models is $\Delta t_{\text{ode}} = 0.01\,\text{ms}$. The spatial discretisation of the tissue sample is based on a regular grid of equidistantly distributed points. Thereby, the spacing of the grid points is $0.5\,\text{mm}$.

An idealised recording system that does not affect the physical fields is assumed to obtain synthetic EMG and MMG signals. For the EMG, it measures at each virtual electrode $\boldsymbol{x}_i^{\text{el}}$ ($i = 1, ..., S_{\text{el}}$, with S_{el} denoting the number of electrodes) the extracellular potential or the

body potential:

$$\mathrm{EMG}_i \;=\; \begin{cases} \phi_\mathrm{e}\ , & \boldsymbol{x}_i^\mathrm{el} \in \Omega_\mathrm{m}\ , \\ \phi_\mathrm{b}\ , & \boldsymbol{x}_i^\mathrm{el} \in \Omega_\mathrm{b}\ . \end{cases} \tag{7.1}$$

This is equivalent to a monopolar EMG recording. The electrodes are always placed on top of the simulated tissue sample. For the virtual MMG, the detection system records at each virtual magnetometer $\boldsymbol{x}_i^\mathrm{mag}$ ($i = 1, ..., S_\mathrm{mag}$, with S_mag denoting the number of magnetometers) all three components of the magnetic field, i.e.,

$$\mathbf{MMG}_i \;=\; \left[B_\mathrm{f}^{\parallel},\, B_\mathrm{t}^{\parallel},\, B_\mathrm{t}^{\perp}\right]^T\ ,\quad \boldsymbol{x}_i^\mathrm{mag} \in \Omega_\mathrm{f}\ . \tag{7.2}$$

Thereby, $B_\mathrm{f}^{\parallel}$ is the magnetic field component aligned with the muscle fibres (and tangential to the body surface), $B_\mathrm{t}^{\parallel}$ is the component of the magnetic field orthogonal to the muscle fibres and tangential to the body surface, and $B_\mathrm{t}^{\perp}$ is the magnetic field component normal to the body surface (and orthogonal to the muscle fibres), see Figure 7.1. Moreover, the virtual magnetometers are always placed 1 mm above the tissue sample's surface. Sampling the model output at each time step, i.e., $\Delta t = 0.1$ ms, yields a sampling frequency of 10 000 Hz for both the synthetic EMG and the synthetic MMG.

7.1.2 Data Analysis

The root mean square (RMS) value is computed to quantify the amplitude of a signal. For an arbitrary signal $\boldsymbol{\psi} \in \mathbb{R}^L$, the root mean square value is defined as:

$$\mathrm{RMS} \;=\; \sqrt{\frac{1}{L}\sum_{i=1}^{L}(\psi^t)^2}\ . \tag{7.3}$$

Therein, the superscript t refers to a (discrete) time sample and L is the total number of samples (in time). Further, the frequency content of the signals is investigated by estimating the power spectral density (PSD), i.e., reflecting the squared modulus of a signal's Fourier transform. The power spectral density is computed using MATLAB's built-in *meanfreq* function. To compute the sparsity and thus the spatial selectivity of a recording, Hoyer's sparsity measure [126, 129] is computed, i.e.,

$$\mathrm{Sparseness}(\boldsymbol{\psi}) \;=\; \left(\sqrt{L} - \frac{||\,\boldsymbol{\psi}\,||_1}{||\,\boldsymbol{\psi}\,||_2}\right)\left(\sqrt{L} - 1\right)^{-1}\ . \tag{7.4}$$

Therein, $||*||_1$ and $||*||_2$ denote the L^1 norm and L^2 norm, respectively.

7.2 Single Sensor Recordings

This section showcases the temporal dynamics of compound muscle electric potentials and compound muscle magnetic fields, i.e., the EMG or MMG signals caused by the simultaneous activity of several muscle fibres. For this purpose, virtual EMG and MMG recordings from a single sampling point are considered. First, the summation of single-fibre muscle action potentials is described. Second, the impact of the muscle fibre type on EMG and MMG signals is examined. Finally, the influence of anatomical factors, such as the depth of the active fibres or the thickness of subcutaneous fat, is investigated.

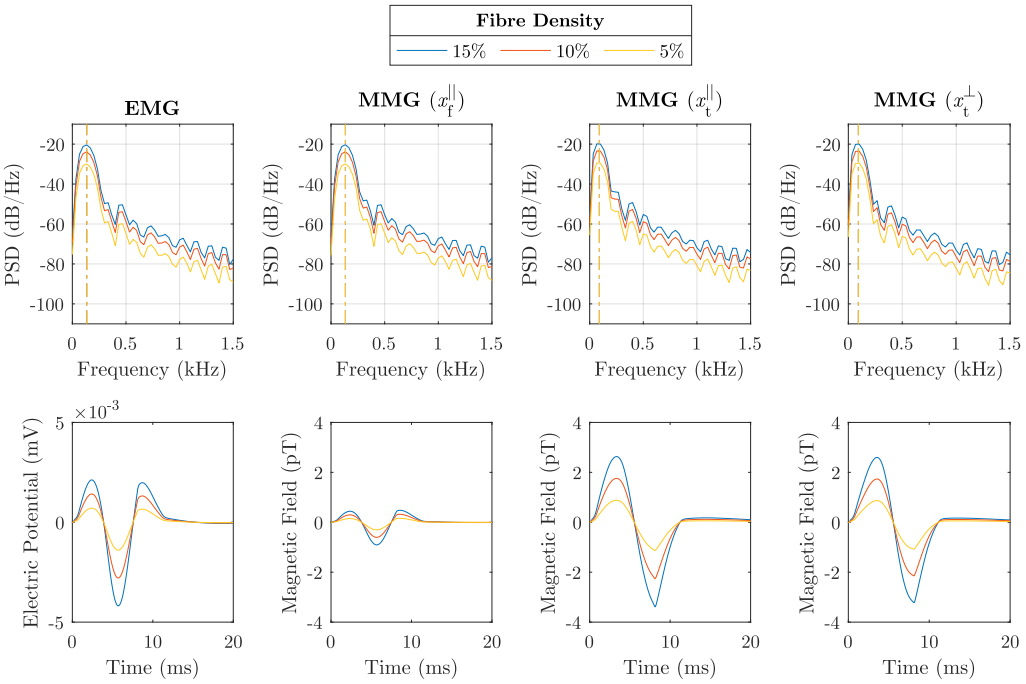

Figure 7.2: Power spectral density (PSD) and time domain graph for the simulated EMG and MMG signal when varying the number of active muscle fibres. Hence, for the same geometrical configuration of the active muscle fibres, the motor unit density parameter f_r^k is varied, i.e., 15 % (blue), 10 % (red) and 5 % (yellow). Each spectrum is normalised with the total power of the respective signal obtained from the simulation with a fibre density of 15 %. The dashed lines in the power spectrum (top row) indicate the mean frequency content of the signal.

7.2.1 The Summation of Muscle Fibre Action Potentials

A single-fibre action potential is the smallest event observable when measuring muscle-induced bioelectromagnetic fields. Detecting single-fibre activity in humans is usually considered a hallmark of neuromuscular diseases [cf. e.g., 226]. For enabling motion, the neuromuscular system recruits motor units (see Chapter 2). This corresponds to the synchronous activity of several muscle fibres. Hence, compound muscle electric potentials and compound muscle magnetic fields are the basic components of EMG or MMG signals in the healthy neuromuscular system. Nevertheless, it is helpful to investigate the signals generated by single fibres to obtain a fundamental understanding of EMG and MMG. Simulating the activity of isolated muscle fibres is beyond the scope of the homogenised multi-domain model presented in Chapter 5. However, the summation of muscle fibre action potentials can be investigated by varying the mesoscale motor unit density parameter f_r^k. Hence, this section considers three simulations where the fibre load of a motor unit (MU1) is varied, i.e., f_r^1 equal to 5 %, 10 % and 15 %. The geometrical settings of the *in silico* experiments are fixed. The depth of the active fibres is 10 mm, and the thickness of the subcutaneous fat tissue is 2 mm. Further, the simulated bioelectromagnetic fields are recorded from a single EMG electrode or MMG sensor placed between the innervation zone and the boundary of the muscle, i.e., $x_l^{\parallel} = 15$ mm and $x_t^{\parallel} = 2.5$ mm (see Figure 7.1).

It can be observed from the bottom row of Figure 7.2 that the duration of compound muscle electric potentials and compound muscle magnetic fields is in the range of 10 ms to 15 ms. Thereby, the MMG components orthogonal to the muscle fibres, i.e., the $x_t^{\perp}$-component and

the $x_t^{\parallel}$-component, show a characteristic two-phasic shape. In contrast, the signals observed through EMG and the MMG's $x_f^{\parallel}$-component have a tri-phasic shape. The difference in the shape is also reflected in the frequency content of the different signals. The spectra of the signals are shown in the top row of Figure 7.2. For example, for $f_r^1 = 15\,\%$ the mean frequency content is 133.4 Hz for the EMG, 134.1 Hz for the MMG's $x_f^{\parallel}$-component, 90.5 Hz for the MMG's $x_t^{\parallel}$-component and 93.2 Hz for the MMG's $x_t^{\perp}$-component. Notably, the shape of all signals is (nearly) independent of the motor unit density f_r^k. This fact is underscored by the mean frequency content variability of all signals being less than 0.5 % when f_r^k varies.

Further, the bottom row of Figure 7.2 shows that the amplitude of the compound muscle electric potential and all components of the compound muscle magnetic field (linearly) correlates with the motor unit volume fraction f_r^k. When comparing the RMS value of signals obtained from simulations with motor unit volume fractions of 5 % and 10 % to that obtained from the in silico experiment with a volume fraction of 15 %, the relative RMS values obtained are 33 % and 66 % respectively for all signals. Further, when comparing the signals obtained from the simulation with a volume fraction of 15 % to the linear combination of the signals from the *in silico* experiments with volume fractions of 5 % and 10 %, the relative L2-errors are 1.1 % for the EMG, 1.1 % for the MMG's $x_f^{\parallel}$-component, 0.8 % for the MMG's $x_t^{\parallel}$-component and 0.8 % for the MMG's $x_t^{\perp}$-component. Hence, the contributions of individual muscle fibre action potentials add up linearly. This holds for compound muscle electric potentials and compound muscle magnetic fields.

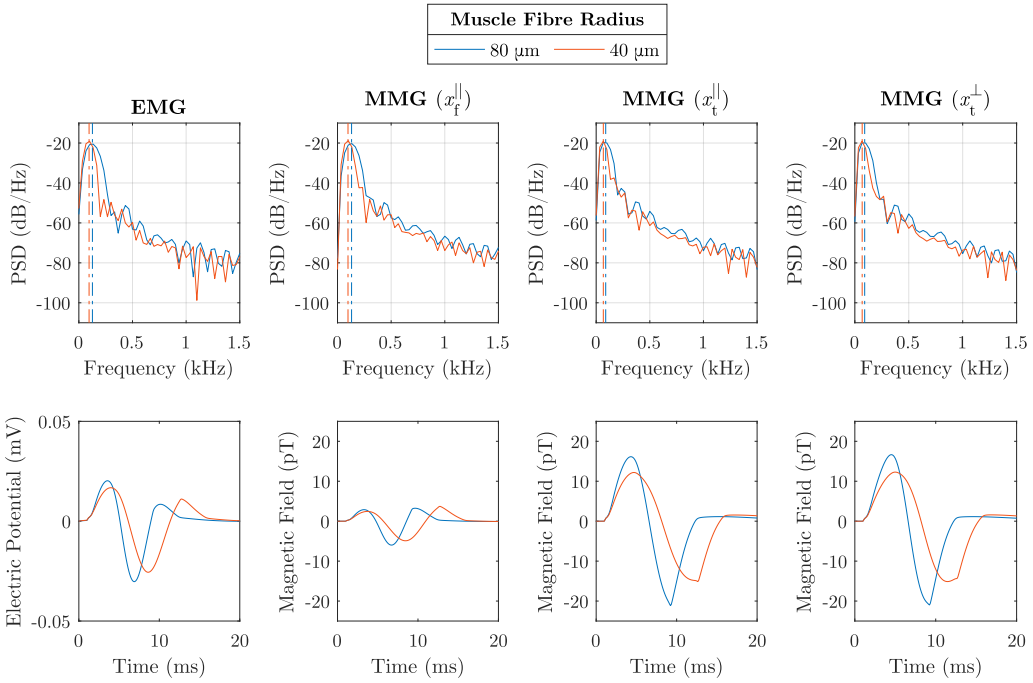

Figure 7.3: Power spectral density (PSD) and time domain graph of the simulated EMG and MMG signal for muscle fibres of different radius (blue: 80 µm; red: 40 µm). Each spectrum is normalised with the total power of the respective signal obtained from the simulation with a fibre radius of 80 µm. The dashed lines in the power spectrum (top row) indicate the mean frequency content of the signal.

7.2.2 Influence of the Muscle Fibre Properties

Next, the influence of the muscle fibre properties on compound muscle electric potentials and compound muscle magnetic fields is examined. As for the simulations presented in the previous section, the geometrical parameters are fixed, i.e., the depth of the activated muscle fibres is 5 mm and the thickness of the subcutaneous fat tissue layer is 2 mm. Further the motor unit density parameter f_{r}^{1} is 100 %. However, virtual muscles with muscle fibres of different sizes are considered, i.e., 80 µm and 40 µm. This corresponds to surface-to-volume ratios A_{m}^{k} of 250 cm^{-1} and 500 cm^{-1}, respectively. The simulated bioelectromagnetic fields are observed from a single EMG electrode or MMG sensor with the coordinates $x_{\mathrm{l}}^{\parallel} = 15\,\mathrm{mm}$ and $x_{\mathrm{t}}^{\parallel} = 2.5\,\mathrm{mm}$.

Figure 7.3 (bottom row) shows that the duration of the compound muscle electric potentials and the compound muscle magnetic fields depends on the muscle fibre radius. For both EMG and MMG the signal duration is approximately 12 ms for a muscle fibre radius of 80 µm and 16 ms for a muscle fibre radius of 40 µm. Yet, the basic shape of the signals is preserved (see Section 7.2.1). This behaviour is also reflected in the signals' frequency content. For example, for a muscle fibre radius of 40 µm, the mean frequency content of the EMG signal decreases by 24.6 % when compared to the simulation with a muscle fibre radius of 80 µm. For the MMG the mean frequency decreases by 25.4 % for the MMG's $x_{\mathrm{l}}^{\parallel}$-component, by 25.1 % for the MMG's $x_{\mathrm{t}}^{\parallel}$-component and by 25.5 % for the MMG's $x_{\mathrm{t}}^{\perp}$-component. Further, it can be observed that the amplitude of the EMG signal decreases by 1.2 % when comparing the simulations with a muscle fibre radius of 80 µm to the simulation with a muscle fibre radius of 40 µm. Analogous, the RMS increases by 12.33 % for the MMG component perpendicular to the muscle fibres as well as parallel to the body surface and increases by 11.6 % for the MMG's normal-to-the-surface component. For the MMG component aligned with the muscle fibre direction, the RMS value is identical for a muscle fibre radius of 40 µm and 80 µm.

7.2.3 Influence of Muscle Fibre Depth

This section investigates the influence of the distance of the active muscle fibres and the sampling point. To focus on the properties of the muscle tissue itself, an isolated muscle is considered. Accordingly, the thickness of the subcutaneous fat tissue layer is 0 mm. A set of compound muscle electric potentials and compound muscle magnetic fields is simulated by selectively stimulating muscle fibres in different depths of the muscle (see Figure 7.1), i.e., 3 mm, 5 mm, 7 mm and 9 mm. The corresponding EMG and MMG signals are recorded from a single electrode or magnetometer with coordinates $x_{\mathrm{l}}^{\parallel} = 15\,\mathrm{mm}$ and $x_{\mathrm{t}}^{\parallel} = 2.5\,\mathrm{mm}$.

The bottom row of Figure 7.4 shows that the amplitude of all signals decreases with increasing depth of the active muscle fibres. Moreover, the decrease in amplitude is more pronounced for the MMG than for the EMG. In detail, when defining the *in silico* experiment with a fibre depth of 3 mm as reference, for a muscle fibre depth of 9 mm the normalised RMS value is 1.2 % for the MMG's $x_{\mathrm{l}}^{\parallel}$-component, 1.2 % for the MMG's $x_{\mathrm{l}}^{\parallel}$-component and 3.1 % for the MMG's $x_{\mathrm{t}}^{\perp}$-component. The normalised RMS value is 13.4 % for the EMG. It is noted that depending on the depth of the active muscle fibres, the magnitude of the compound muscle magnetic fields is in the range of femto-Tesla to pico-Tesla.

Moreover, it can be observed that the EMG exhibits a more pronounced modulation in frequency content than the MMG. In detail, when defining the simulation with a depth of 3 mm as a reference, for a muscle fibre depth of 9 mm, the EMG's mean frequency drops by 26.9 %. In comparison, the mean frequency decreases by 12.2 % for the MMG component aligned with the

muscle fibres and decreases by 15.0 % for the MMG component orthogonal to the body surface. Further, the modulation of the frequency content is less than 2 % for the MMG's $x_{\mathrm{t}}^{\parallel}$ component.

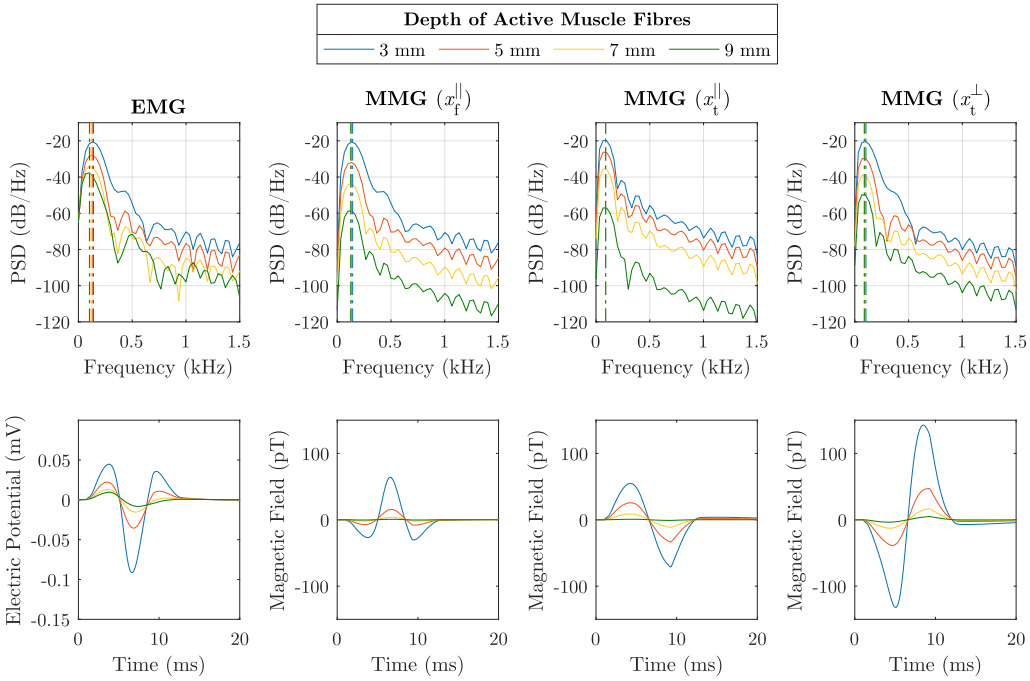

Figure 7.4: Power spectral density (PSD) and time domain graph of the simulated EMG and MMG signals for variable depths of the activated muscle tissue (blue: 3 mm; red: 5 mm; yellow: 7 mm; green: 9 mm). Each spectrum is normalised with the total power of the respective signal obtained from the simulation with a depth of 3 mm. The dashed lines in the power spectrum (top row) indicate the mean frequency content of the signal.

7.2.4 Influence of Fat Tissue

Previously, it was shown that the shape and the amplitude of EMG or MMG signals depend on the distance between the active muscle fibres and the sampling point. This behaviour is because a propagating source is observed, as well as the electric properties and the geometry of the tissue. In this section, the influence of the tissue properties is studied. For this purpose, three *in silco* experiments with a fixed distance between the sampling point and the active muscle fibres are considered. However, the thickness of the subcutaneous fat tissue layer is varied, i.e., 0 mm, 2 mm and 4 mm. To compensate for the differences in the fat tissue thickness, the depth of the stimulated muscle fibres is 5 mm, 3 mm and 1 mm, respectively. This yields a fixed distance of 5 mm between the active fibres and the body surface. A virtual EMG electrode or MMG sensor is placed in the middle between the innervation zone and the boundary of the muscle, i.e., $x_{\mathrm{l}}^{\parallel} = 15\,\mathrm{mm}$ and $x_{\mathrm{t}}^{\parallel} = 2.5\,\mathrm{mm}$.

Figure 7.5 (bottom left) illustrates that the amplitude of a compound muscle electric potential strongly depends on the thickness of the fat tissue layer. Comparing the RMS of the EMG signals simulated for fat tissue layers of 2 mm and 4 mm to the case without fat, an increase of the RMS by 109.0 % and 281.1 % is observed. The amplitude of the compound muscle magnetic fields also depends on the thickness of the fat tissue layer. However, the effect of the tissue arrangement is less pronounced for the MMG than for the

EMG. In detail, the influence of the fat tissue is least pronounced for the MMG's normal-to-the-surface component. When using the signal obtained from the simulation without fat as a reference, for fat tissue layers of 2 mm and 4 mm, the RMS increases by 22.8 % and 53.2 %, respectively. For the same scenario, the RMS of the MMG's $x_{\mathrm{f}}^{\parallel}$-component increases by 40.7 % and 106.7 %. The RMS increases by 49.3 % and 106.2 % for the MMG's $x_{\mathrm{t}}^{\parallel}$-component.

Further, one can observe an increase in the mean frequency for all signals. For example, when comparing the simulation without fat and the simulation with a fat tissue thickness of 4 mm, the mean frequency of the EMG signal increases by 12.5 %. In comparison, the mean frequency increases by 12.8 % for the MMG's $x_{\mathrm{f}}^{\parallel}$-component, 6.1 % for the MMG's $x_{\mathrm{t}}^{\parallel}$-component and 7.6 % for the MMG's $x_{\mathrm{t}}^{\perp}$-component

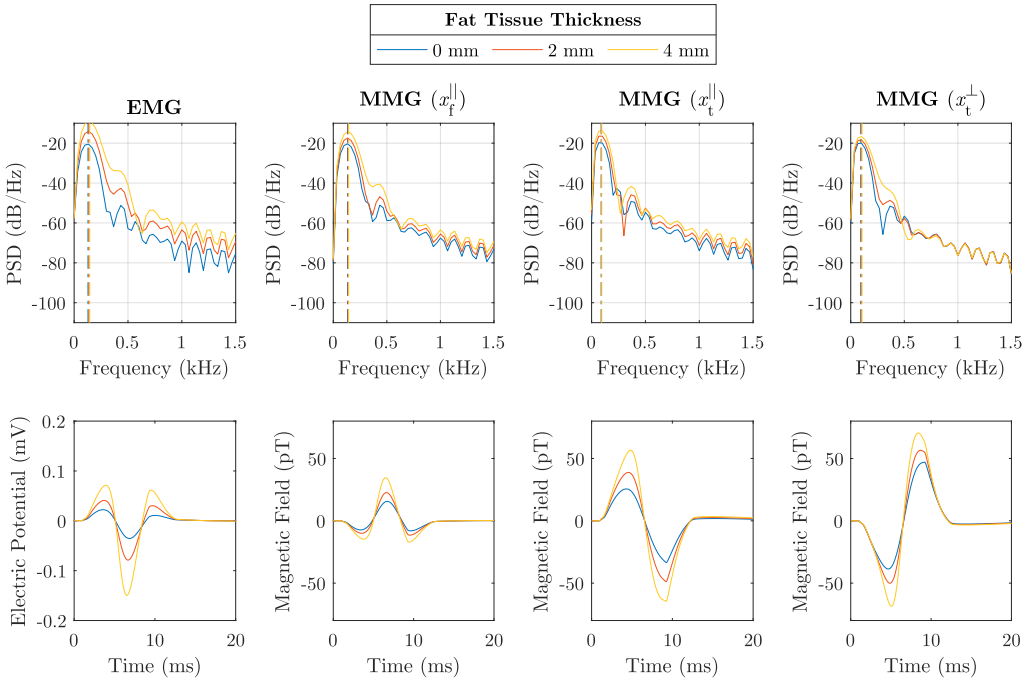

Figure 7.5: Power spectral density (PSD) and time domain graph of the simulated EMG and MMG signals for variable thicknesses of a superficial fat tissue layer, i.e., 0 mm (blue), 2 mm (red) and 4 mm (yellow). The distance between the active fibres and the body surface is fixed, yielding fibre depths of 9 mm, 7 mm and 5 mm, respectively. Each spectrum is normalised by the total power of the respective signal obtained from the simulation without fat. The dashed lines in the power spectrum (top row) indicate the mean frequency content of the signal.

7.3 High-Density Recordings

Bioelectromagnetic fields depend on the spatial coordinate of an observation and time. Hence, measuring EMG or MMG at multiple points in space yields images of the electric potential or magnetic field for each time frame. When a dense array of sampling points is used, such measurements are called high-density recordings. This section investigates the fundamental spatiotemporal patterns of muscle-induced bioelectromagnetic by considering compound muscle electric potentials and compound muscle magnetic fields detected by utilising (virtual) high-density recordings.

7.3.1 The Spatiotemporal Patterns of EMG and MMG Signals

To illustrate the fundamental properties of high-density EMG (HD-EMG) and high-density MMG (HD-MMG) signals, a single *in silico* experiment is analysed. Muscle fibres are selectively stimulated in a depth of 5 mm. Further, a fat tissue layer with a thickness of 2 mm is added on top of the muscle. The corresponding bioelectromagnetic fields are recorded with a detection system consisting of 7×7 sampling points (see Figure 7.6A). The sampling points span from the innervation zone (IZ) to the myotendinous junction (MTJ), and their spacing along the muscle fibre direction is 5 mm. Further, the sampling points span the whole width of the muscle, and the spacing perpendicular to the muscle fibre direction is 2.5 mm.

The spatiotemporal pattern of the simulated high-density EMG is shown in Figure 7.6B. Further, Figure 7.6C-E show the corresponding high-density MMG. Thereby, the three magnetic field components are visualised in individual panels. First, it is noted that the high-density EMG or MMG signals exhibit a time delay when comparing two signals from different sampling points in a line parallel to the muscle fibre direction. Hence, the temporal coordinate is linked to the spatial coordinate. Logically, this is caused by the propagation of the muscle fibre action potentials. For the high-density EMG, Figure 7.6B illustrates that the basic (time-domain) shape of the observable compound muscle electric potential depends on the $x_{\mathrm{f}}^{\parallel}$-coordinate, i.e., two-phasic at the innervation zone as well as at the myotendinous junction and tri-phasic in between [cf. e.g., 147]. For the high-density MMG, the relation between the spatial coordinate and the compound muscle magnetic field shape depends on the measured magnetic field component. In detail, the MMG's normal-to-the-surface component shows a characteristic bi-phasic shape for all sampling points of the high-density MMG array. Notably, the $x_{\mathrm{t}}^{\parallel}$ coordinate of the active muscle fibres represents a reflection axis, where the sign of the signal is flipped (see Figure 7.6E). This behaviour is also observed for the MMG's $x_{\mathrm{f}}^{\parallel}$-component. However, comparable to high-density EMG, the signal's shape depends on the spatial coordinate along the muscle fibre direction, i.e., bi-phasic at the innervation zone and the myotendinous junction and tri-phasic in between. The MMG's $x_{\mathrm{f}}^{\parallel}$-component also shows a characteristic bi-phasic shape. Moreover, Figure 7.6D shows that the magnetic field component orthogonal to the muscle fibres and parallel to the body surface is maximal directly above the active muscle fibres and quickly decreases in the lateral direction. Finally, it is noted that both MMG components that are orthogonal to the muscle fibre direction are zero at the innervation zone and decrease in amplitude towards the myotendinous junction.

7.3.2 The Influence of the Muscle Fibre Properties

In the previous section, it was demonstrated that for muscle-induced bioelectromagnetic fields, the temporal coordinate and the spatial coordinate are linked, i.e., due to the propagating nature of the action potentials. Typically, it is assumed that the action potential conduction velocity is related to the properties of the muscle fibres, i.e., particularly the muscle fibre diameter [e.g., 5, 10, 96]. Hence, this section investigates the spatiotemporal correlation of high-density EMG signals and high-density MMG signals as a function of muscle fibre size. Therefore, two different muscles consisting of differently sized muscle fibres, i.e., the muscle fibre radius is 80 µm and 40 µm, are simulated. This corresponds to surface-to-volume ratios A_{m}^{k} ($k = 1, 2$) of $250\,\mathrm{cm}^{-1}$ and $500\,\mathrm{cm}^{-1}$, respectively. A fat tissue layer with a thickness of 2 mm is added on top of both virtual muscles. Compound muscle electric potentials and compound muscle magnetic fields are simulated by selectively recruiting all muscle fibres in a depth of 5 mm.

Within the *in silico* simulation framework, the muscle fibre conduction velocity can be directly

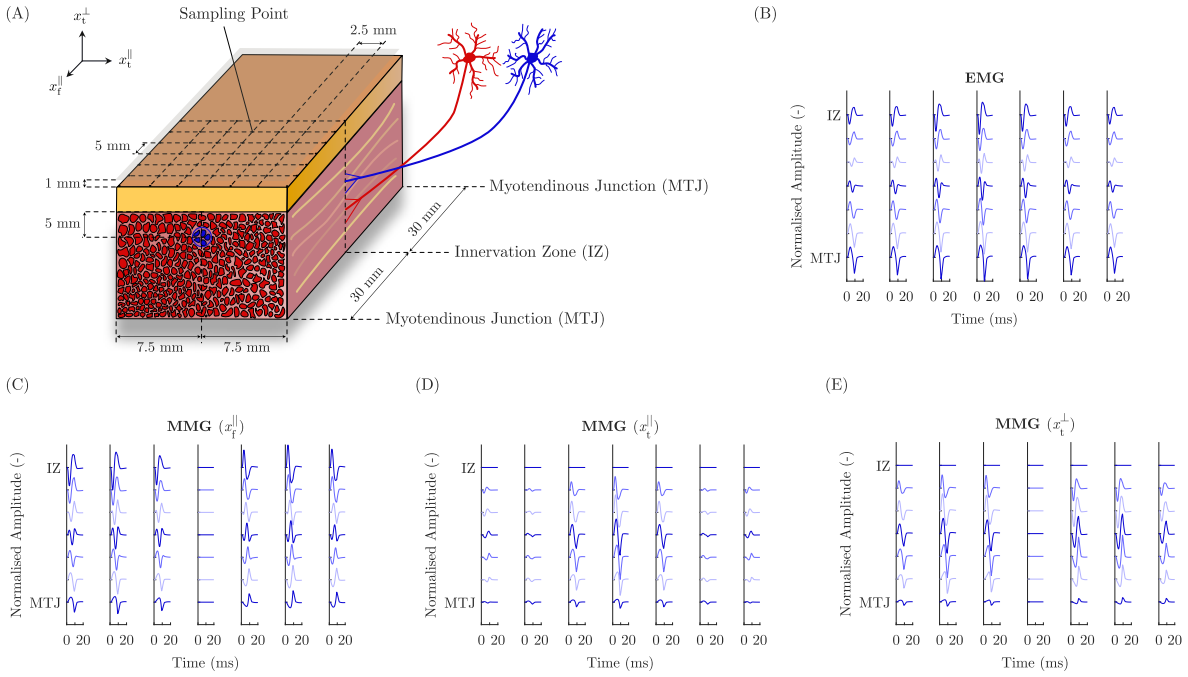

Figure 7.6: High-density EMG or MMG signals recorded from a grid with 7×7 sampling points. (A) The sampling points span from the innervation zone (IZ) to the myotendinous junction (MTJ), i.e., the end of the muscle fibres. The step size between the sampling points is 5 mm along the muscle fibre direction and 2.5 mm transversal to the muscle fibre direction. The EMG electrodes are on the body surface, and the magnetometers are shifted by 1 mm above the body surface (transparent plane). The depth of the activated muscle fibres is 5 mm. Further, in the $x_\mathrm{t}^{\parallel}$-direction, the active fibres are centred in the middle of the tissue sample. (B) Spatiotemporal pattern of the simulated compound muscle electric potential. (C) to (E) Spatiotemporal patterns of the simulated compound muscle magnetic fields, i.e., the individual magnetic field components.

measured by computing the temporal delay of the transmembrane potential at two points along the muscle fibre path. In detail, for the simulations with a fibre radius of 40 µm and 80 µm, the muscle fibre conduction velocities are $2.78\,\mathrm{m\,s^{-1}}$ and $3.85\,\mathrm{m\,s^{-1}}$, respectively. Figure 7.7 shows the simulated compound muscle electric potential and all components of the compound muscle magnetic field on a linear array of sampling points along the muscle fibre direction, i.e., $x_\mathrm{t}^{\parallel} = 2.5\,\mathrm{mm}$. The distance between the sampling points is 5 mm, and the sampling points span from the innervation zone to the myotendinous junction. It can be observed that the spatiotemporal delay of the signals correlates with the muscle fibre conduction velocity. Hence, the muscle fibre conduction velocities can be estimated indirectly by computing the temporal delay associated with the maximum cross-correlation for two signals sampled at different locations along the muscle fibre direction [cf. e.g., 177]. Thereby, the influence of end of fibre effects, as well as end plate effects, can be reduced by considering double differential signals [17], i.e., the summed signal of two outer sampling points subtracted by twice the signal recorded at a central sampling point. For example, if one considers two double differential signals between the innervation zone and the myotendinous junction, the conduction velocities estimated from the EMG are $2.9\,\mathrm{m\,s^{-1}}$ and $4.2\,\mathrm{m\,s^{-1}}$. Further, the conduction velocities computed from the MMG signals are $2.9\,\mathrm{m\,s^{-1}}$ and $4.5\,\mathrm{m\,s^{-1}}$ for the MMG's $x_\mathrm{f}^{\parallel}$-component, $2.5\,\mathrm{m\,s^{-1}}$ and $3.6\,\mathrm{m\,s^{-1}}$ for the MMG's $x_\mathrm{t}^{\parallel}$-component as well as $2.5\,\mathrm{m\,s^{-1}}$ and $3.3\,\mathrm{m\,s^{-1}}$ MMG's $x_\mathrm{t}^{\perp}$-component.

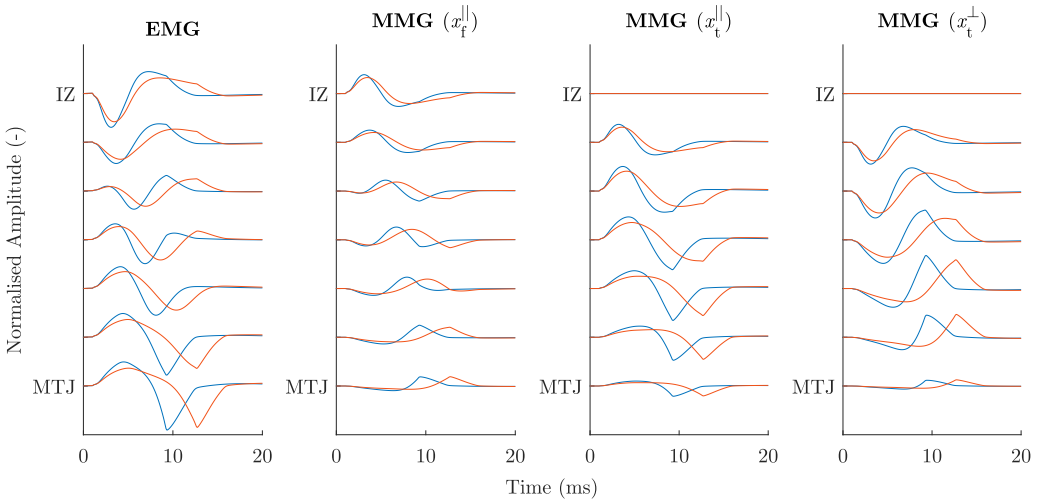

Figure 7.7: High-density EMG and high-density MMG signals observed from a linear array of sampling points. The sampling points span from the innervation zone (IZ) to the myotendinous junction (MTJ). Moreover, the sampling points are shifted by 2.5 mm from the muscle's transversal centre line. The spacing of the sampling points is 5 mm. The red curve curves correspond to the simulation with a muscle fibre radius of 80 µm, and the blue curve corresponds to the simulation with a muscle fibre radius of 40 µm.

7.3.3 The Distribution of the Signal Amplitude

Instead of directly analysing the spatiotemporal patterns of bioelectromagnetic fields, features of a signal can be computed for each sampling point. This reduces the multi-dimensional data to two-dimensional images. Here, the spatial distribution of the signal amplitude is considered. This is achieved by computing the RMS value for each discretisation point on the body surface. A single *in silico* experiment is considered to compare the images of the RMS values. The muscle is activated by selectively stimulating the muscle fibres in a depth of 5 mm. Further, a fat tissue layer with a thickness of 2 mm is added on top of the muscle.

From Figure 7.8, it can be observed that the signal amplitude distribution is fundamentally different for the EMG and the three MMG components. When fixing the spatial coordinate along the muscle fibre direction, for the EMG, the RMS is maximal directly over the active muscle fibres and decreases towards the muscle's boundary. The MMG's $x_t^{\parallel}$-component is also maximal directly above the active fibres. However, the signal amplitude is more spatially confined. For the MMG's $x_f^{\parallel}$-component and the MMG's $x_t^{\perp}$-component, the signal amplitude is zero directly over the active fibres.

Suppose a line parallel to the muscle fibre direction is followed. In that case, the RMS of the EMG shows two local maxima, i.e., one at the innervation zone and one at the myotendinous junctions. Further, the signal amplitude is maximal at the innervation zone for the MMG's $x_f^{\parallel}$-component. In contrast, the amplitude is zero at the innervation zone for both MMG components perpendicular to the muscle fibres. Further, the RMS images of the MMG's $x_t^{\parallel}$-component and the MMG's $x_t^{\perp}$-component have the maximal intensity in the middle between the innervation zone and the myotendinous junction.

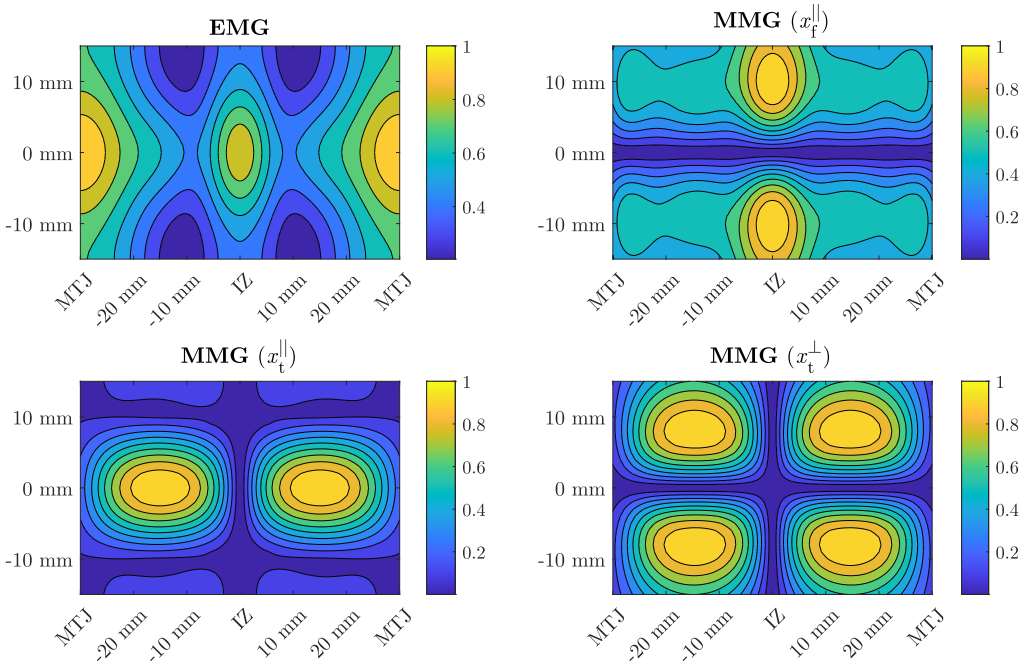

Figure 7.8: Root mean square (RMS) images of a compound muscle electric potential as well as the compound muscle magnetic field for each discretisation point on the body surface. The RMS values are normalised to the corresponding maximum value.

7.3.4 The Influence of the Tissue Properties

After considering the basic spatiotemporal patterns of compound muscle electric potentials and compound muscle magnetic fields, this section investigates the influence of the tissue properties and composition on high-density EMG or MMG. This is accomplished through a series of *in silico* experiments that vary the depth of the active muscle fibres as well as the thickness of the subcutaneous fat. In detail, muscle fibres are selectively stimulated in depths of 1 mm, 3 mm, 5 mm, 7 mm and 9 mm, respectively. Further, three fat tissue layers with thicknesses of 0 mm, 2 mm and 4 mm are considered. This yields a set of 15 simulations. The predicted bioelectromagnetic fields are investigated by computing the RMS value for each discretisation point on the body surface.

Figure 7.9 summarises for all conducted *in silico* experiments the RMS of the EMG as well as the three MMG components in a line perpendicular to the muscle fibres mid-way through the innervation zone and the myotendinous junction, i.e., $x_l^{||} = 15\,\text{mm}$. As reported in the previous section, the distribution of the RMS values is fundamentally different for the EMG and the three MMG components. For the EMG, the RMS reaches its maximum directly over the active fibres. In contrast, for the MMG's $x_l^{||}$-component and the MMG's $x_t^{\perp}$-component, the compound muscle electric potential's amplitude is zero directly over the active fibres, i.e., the muscle's transversal centre line. When increasing the distance to the muscle's transversal centre line, the RMS first increases and decreases after reaching its maximum. Notably, the distance to the maximum correlates with the depth of the active fibres. For the case without fat, the distance between the zero value of the MMG's $x_l^{||}$-component (i.e., directly over the source) and the maximal RMS value is 2 mm for a fibre depth of 1 mm, 3 mm for a fibre depth of 3 mm and 3.5 mm for fibre depths below 5 mm. For the MMG's $x_t^{\perp}$-component and in the case without

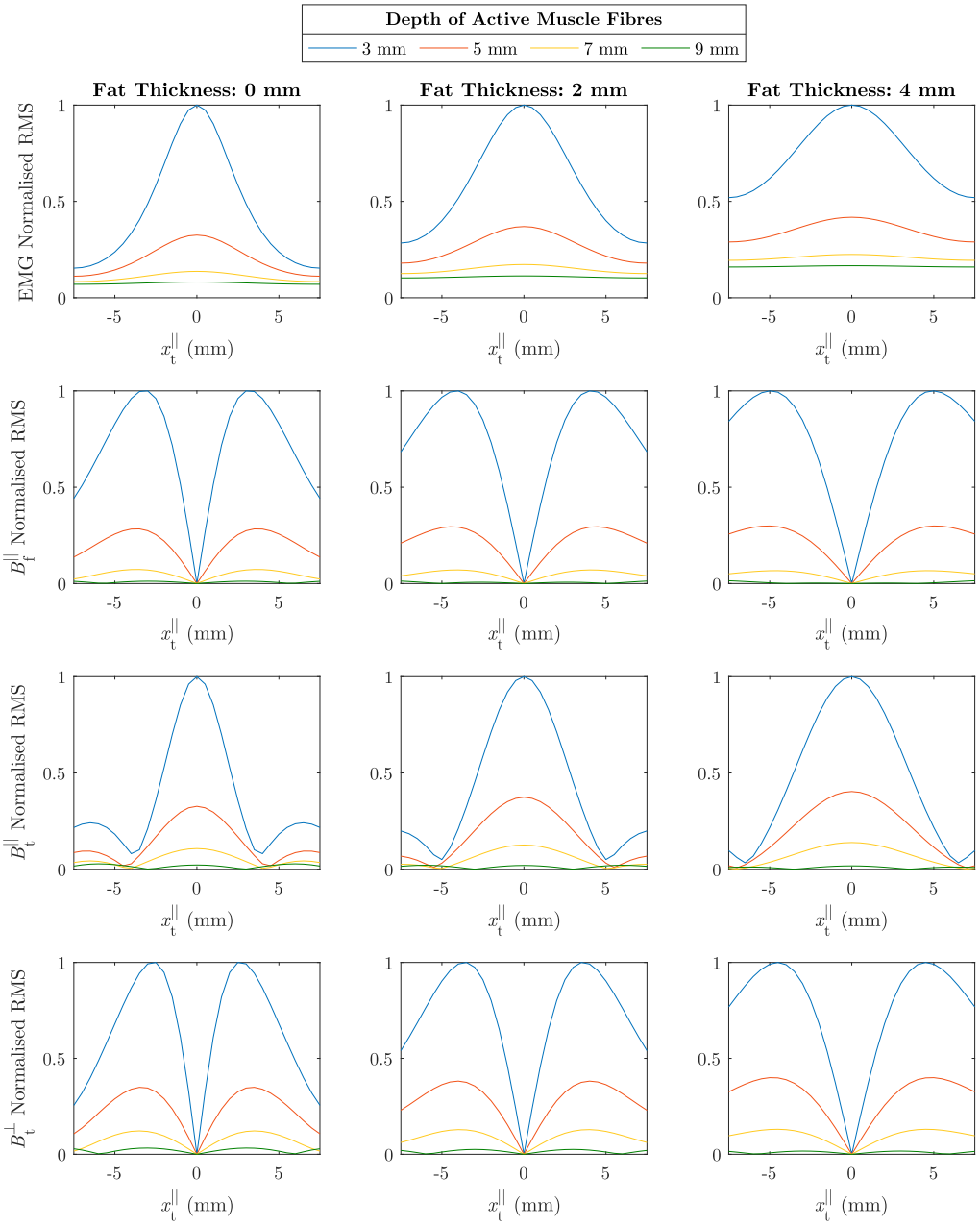

Figure 7.9: Normalised RMS values in a line orthogonal to the muscle fibres in the middle between the innervation zone and the muscle boundary, i.e., $x_1^{\parallel} = 15\,\text{mm}$. From left to right, the thickness of the fat tissue increases. The first row shows the EMG, the second row shows the $x_1^{\parallel}$-component of the MMG, the third row shows the $x_t^{\parallel}$-component of the MMG, and the fourth row shows $x_t^{\perp}$-component of the MMG. Further, the colours indicate the depth of the activated muscle fibres (blue: 3 mm; red: 5 mm; yellow: 7 mm; green: 9 mm; grey: 11 mm).

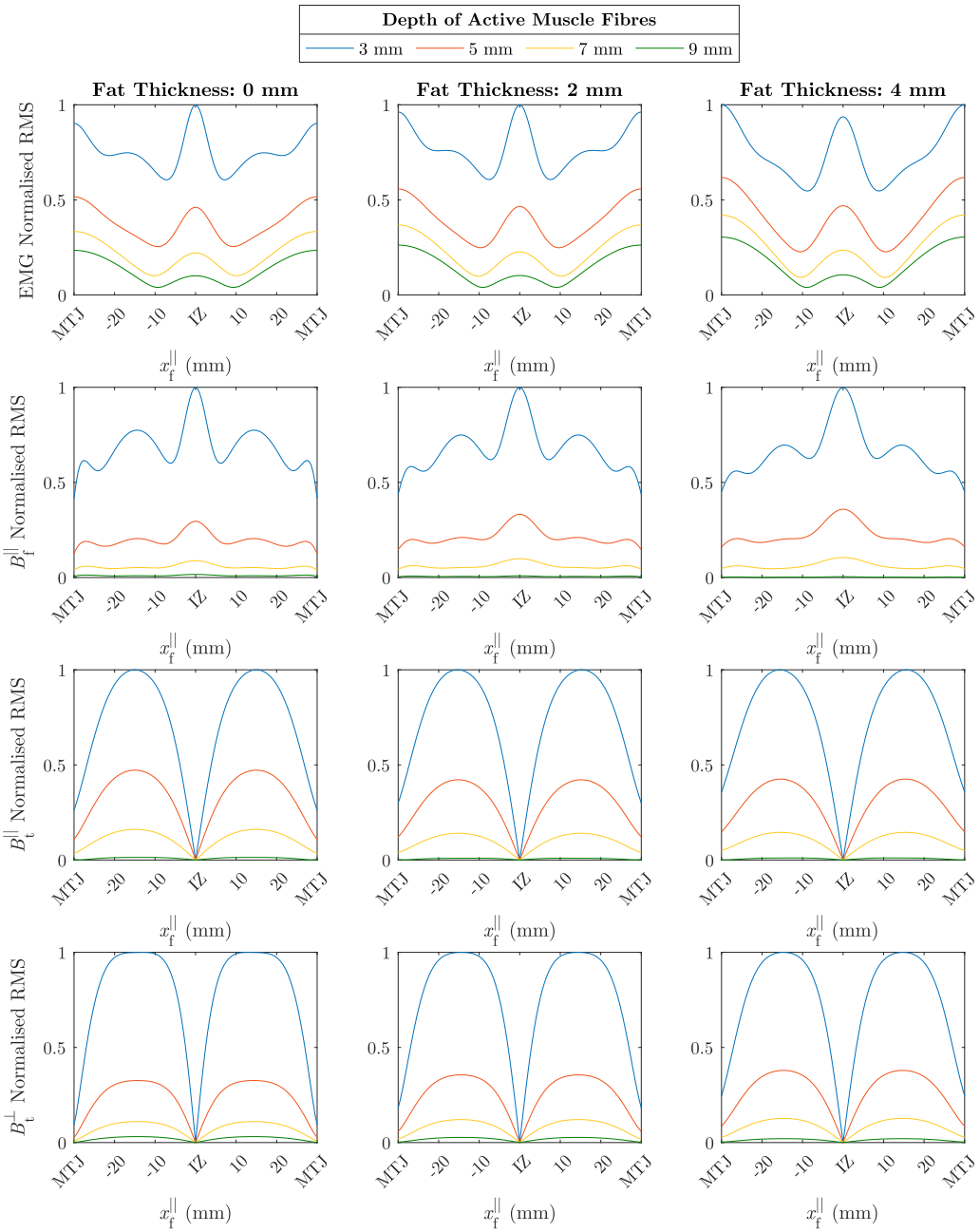

Figure 7.10: Normalised RMS values in a line parallel to the muscle fibres, i.e., $x_t^{\parallel} = 2.5\,\text{mm}$. From left to right, the thickness of the fat tissue layer increases. The first row shows the EMG, the second row shows the MMG's $x_l^{\parallel}$-component, and the third row shows the MMG's $x_t^{\parallel}$-component and the fourth row shows the MMG's $x_t^{\perp}$-component. Further, the colours indicate the depth of the activated muscle fibres (blue: 3 mm; red: 5 mm; yellow: 7 mm; green: 9 mm; grey: 11 mm).

fat, the distance between the maximum RMS value and the zero value is 1.5 mm for a fibre depth of 1 mm, 2.5 mm for a fibre depth of 3 mm and saturates at 3.5 mm for fibre depths below 5 mm.

When increasing the thickness of the fat tissue layer's thickness, the sparsity of the signals is modulated. For example, for a muscle fibre depth of 3 mm the Hoyer sparsity value, cf. Section 7.1.2, of the RMS values decreases by a factor of 6.04 when comparing the case with a fat tissue thickness of 4 mm to the case without fat. The sparsity of the MMG is less affected by the subcutaneous fat tissue. In detail, for the MMG component aligned with the muscle fibre direction, the Hoyer sparsity of the RMS values increases by a factor of 1.08. Moreover, the Hoyer sparsity of the RMS values decreases by a factor of 1.08 for the MMG's $x_{\mathrm{t}}^{\parallel}$-component and decreases by a factor of 1.40 for the MMG's $x_{\mathrm{t}}^{\perp}$-component.

Further, Figure 7.10 shows the RMS of the simulated EMG and MMG signals in a line parallel to the muscle fibre direction, i.e., $x_{\mathrm{t}}^{\parallel} = 2.5\,\mathrm{mm}$. Notably, it is observed that the main characteristics of the amplitude distribution along the muscle fibre direction are (nearly) invariant to the depth of the active fibres and the thickness of the subcutaneous fat tissue layer. For example, it can be observed that independent of the depth of the active muscle fibres and the thickness of the subcutaneous fat tissue layer, the amplitude of the MMG components perpendicular to the muscle fibres, i.e., the $x_{\mathrm{t}}^{\parallel}$-direction and the $x_{\mathrm{t}}^{\perp}$-direction, is zero at the innervation zone. In contrast, the MMG component aligned with the muscle fibres shows a local maximum at the innervation zone. The same behaviour is observed for the EMG. However, for the EMG, the dominance of the local maximum at the innervation zone depends on the depth of the active muscle fibres. For the MMG's $x_{\mathrm{t}}^{\parallel}$-component, several local maxima can be observed between the innervation zone and the myotendinous junction. However, the number of local maxima and their location varies depending on the depth of the active muscle fibres and the thickness of the subcutaneous fat tissue layer.

7.4 The Source of the Muscle-Induced Magnetic Field

The electric activity of the muscle fibre membranes ultimately causes MMG. The muscle fibre action potentials yield conductive currents in the muscle fibres and the extracellular space. Both types of current contribute to the measurable magnetic field. Within the presented *in silico* simulation framework, the magnetic field can be decomposed into the contributions of each domain, i.e., the intracellular domains of all motor units, the extracellular domain and the body region. This is possible due to the linearity of the magnetic field equations, i.e., Equation (5.18) and Equation (5.19). By computing the magnetic field generated by the currents in each domain, this section predicts the relevance of the different currents for the measurable MMG signal.

7.4.1 Single Sensor MMG Recordings

The contribution of the different current densities to the total MMG signal is exemplarily investigated for a single *in silico* experiment. That is, for a cube-shaped muscle and a superficial fat tissue layer with a thickness of 2 mm, muscle fibres in a depth of 5 mm are selectively stimulated. The magnetic field induced by the current densities in each domain of the multi-domain skeletal muscle model and the body region is computed. The results obtained from this *in silico* experiment are exemplarily evaluated at a single sampling point on the body surface, i.e., $x_{\mathrm{f}}^{\parallel} = 15\,\mathrm{mm}$ and $x_{\mathrm{t}}^{\parallel} = 2.5\,\mathrm{mm}$. From the left panel in Figure 7.11, it can be observed that the MMG's $x_{\mathrm{l}}^{\parallel}$-component is fully determined by volume currents in the extracellular space and the body

region. When normalising the RMS of the signals generated by an individual current source to the RMS value of the overall magnetic field, the RMS of the extracellular contribution is 99.9 %, and the RMS of the body region contribution is 0.1 %. Further, Figure 7.11 (middle and right) show that the MMG components orthogonal to the muscle fibre direction, i.e., the $x_{\mathrm{t}}^{\parallel}$-component and the $x_{\mathrm{t}}^{\perp}$-component, depend on currents from all domains. Notably, the non-recruited muscle fibres contribute considerably to the experimentally observable magnetic field. The magnetic field contribution of the recruited fibres has the opposite direction than the contributions from the non-recruited fibres and the extracellular domain. In detail, for the MMG's $x_{\mathrm{t}}^{\parallel}$-component, the relative domain-specific RMS values, i.e., normalised to the RMS of the overall magnetic field, are 313.7 % for the extracellular space, 824.8 % for the recruited intracellular domains, 416.9 % for the non-recruited intracellular domains and 0.2 % for the body region. Considering the MMG's normal-to-the-body-surface component, the recruited fibres dominate the measurable signal, i.e., the relative RMS value is 253.6 %. Further, the relative RMS values are 101.3 % for the non-recruited intracellular domains, 55.9 % for the extracellular space and 0.03 % for the body region.

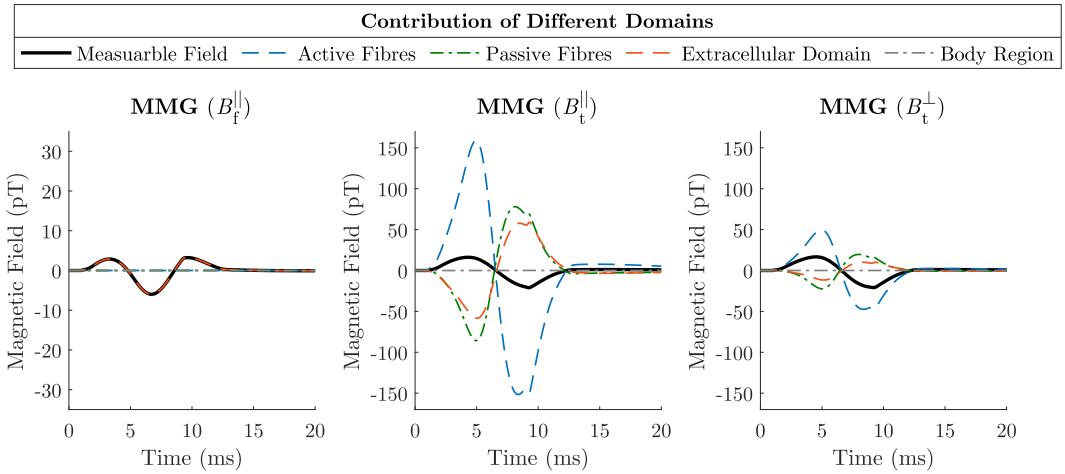

Figure 7.11: Contribution of different domains to the magnetic muscle compound action potential. The presented data correspond to a simulation where the muscle fibres are stimulated in a depth of 5 mm. The coordinates of the MMG sensor are $x_{\mathrm{l}}^{\parallel} = 15\,\mathrm{mm}$ and $x_{\mathrm{t}}^{\parallel} = 2.5\,\mathrm{mm}$.

7.4.2 High-Density MMG Recordings

After considering the contribution of different currents to the MMG signal for an arbitrarily chosen sampling point, this section generalises the results from the previous section for a high-density MMG array. Here, an array of 4×3 sampling points is considered. The distance between two sampling points is 10 mm along the muscle fibre direction and 5 mm perpendicular to the muscle fibre direction.

It can be observed from Figure 7.12A that the MMG component aligned with the muscle fibres is fully determined by currents in the extracellular space and the body region. This is explained by the fact that the magnetic field is related to the current density through the curl operator. Further, from Figure 7.12B and Figure 7.12C, it can be seen that the magnetic field induced by the intracellular currents always shows a characteristic two-phasic shape. This is in agreement with magnetic field measurements from single muscle fibres [256]. Hence, more complex waveforms are always caused by extracellular currents (see Figure 7.12B). Note that extracellular

currents are expected to strongly depend on the exact geometry of the muscle and the surrounding tissues. Hence, the results can differ between different subjects or muscles. Moreover, it is observed that intracellular currents dominantly cause the magnetic field components orthogonal to the muscle fibre direction. However, as the muscle fibre action potentials trigger reversal currents in the extracellular space and passive muscle fibres, the observable magnetic field is considerably lower than the magnetic field caused by active muscle fibres.

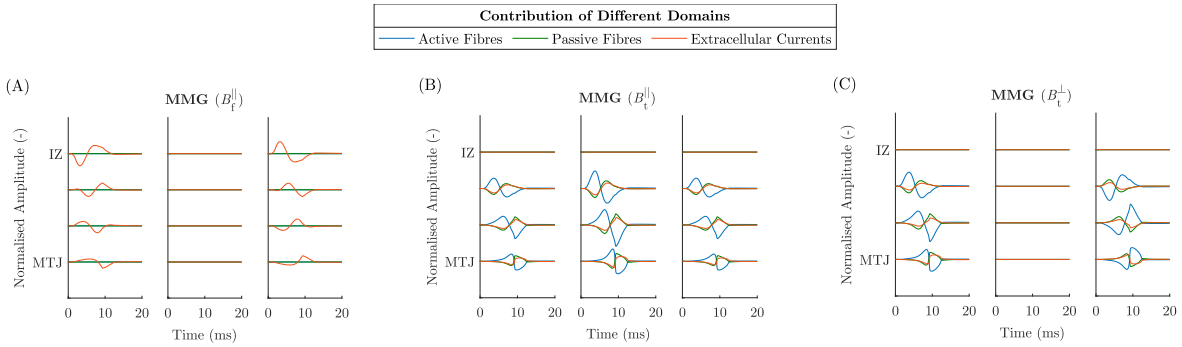

Figure 7.12: Contribution of different currents to an exemplary high-density magnetic compound muscle magnetic field. Each panel (A to C) shows one MMG component. The magnetic field induced by the active muscle fibres is shown in red. The yellow colour indicates the magnetic field induced by currents in the non-recruited muscle fibres. Further, the green colour shows the magnetic field generated by extracellular currents, i.e., the extracellular domain of the muscle region as well as the body region.

7.5 Summary and Discussion

This chapter provides the first systematic comparison of EMG and MMG. The analysed signals are simulated with the biophysical model presented in Part II of this work. This data is comparable to EMG and MMG of electrically or reflex-evoked contractions [e.g., 15]. However, experimentally, controlling the position and the number of recruited muscle fibres is impossible. Thus, the presented *in silico* experiments provide insights on muscle-induced bioelectromagnetic fields that would currently not be easily feasible through experimental methods.

EMG and MMG are caused by the propagation of action potentials in the muscle fibres. Notably, the electric compound muscle electric potentials and the magnetic compound muscle magnetic fields represent the linear summation of the signals generated by all involved muscle fibre action potentials (see Section 7.2.1). Moreover, the duration of compound muscle electric potentials measured via EMG or compound muscle magnetic fields recorded by MMG is comparable, which agrees with experimental observations [cf. e.g., 19, 38, 207, 271]. However, there are substantial differences concerning the spatiotemporal patterns of each signal. That is, EMG and the different MMG components vary in basic signal shape (see Section 7.3.1) and the spatial distribution of the signal amplitude (see Section 7.3.3). Common for all signals is that the spatial and temporal coordinates are linked, i.e., due to the propagating nature of the muscle fibre action potentials (see Section 7.3.2). For the interpretation of EMG and MMG signals, it is essential to consider that bioelectromagnetic fields induced by active skeletal muscles depend on (i.) the properties of the recruited muscle fibres, (ii.) the relative position between the sampling point and the active fibres and (iii.) the properties of the tissue itself. Those factors are typically unknown in an *in vivo* experiment. Hence, the interpretation of non-invasively recorded signals is associated with significant levels of uncertainty. This is

a well-known limitation of surface EMG measurements [cf. e.g., 45, 70] and represents a significant factor that invasive needle EMG recordings are preferred in clinical applications [e.g., 26, 43, 226]. The interpretation of non-invasive MMG data is subject to the same sources of uncertainty. Yet, it is shown that high-density MMG data is sparser and, hence, spatially more selective than comparable high-density EMG data. Thus, using MMG instead of EMG potentially leads to superior results when inverse modelling is used to reconstruct the bioelectric sources in skeletal muscles [e.g., 152, 154, 180, 255]. However, despite this theoretical advantage of MMG shown through computer simulations, experimental research is needed to determine whether MMG can provide new insights into neuromuscular physiology.

Further, the capabilities of the *in silico* environment are exploited for exploring the biophysical origin of the magnetic field generated by a skeletal muscle. An electrical current only can generate a magnetic field circular to the direction of the current. Accordingly, it is shown that the magnetic field aligned with the muscle fibres is entirely determined by volume currents in the extracellular space or the body region. In contrast, both magnetic field components orthogonal to the muscle fibre direction are dominantly caused by currents in the active fibres. The magnetic field generated by the active muscle fibres shows a characteristic bi-phasic shape, which is in agreement with experimental findings [cf. 256]. The charge balance ultimately requires the existence of reversal currents. Such reversal currents exist both in the extracellular space as well as in non-recruited muscle fibres. This effect limits the amplitude of the measurable magnetic field. However, as the extracellular region allows the flux of ions in all spatial directions, the magnitude of the overall magnetic field is larger than zero.

This chapter showed that the amplitude of compound muscle magnetic fields is in the range of pico-Tesla. Moreover, it is shown that the bandwidth of MMG signals is comparable to EMG data. Hence, the noise spectral density of MMG sensors should be as low as a few tens of $\mathrm{fT}/\sqrt{\mathrm{Hz}}$ and their bandwidth should be up to 500 Hz. Currently, this is only possible with the superconducting quantum interference device (SQUID) [e.g., 35, 143] and optically pumped magnetometers (OPMs) [e.g., 14, 95, 205, 231]. However, as SQUIDs require cryogenic cooling, they must be placed several centimetres away from the subject. Moreover, as SQUID arrays are rigid devices optimised for brain recordings, existing systems do not provide sufficient flexibility to measure MMG. OPMs can be modularly arranged to record signals from all superficial muscles. Yet, SQUIDs are still superior to OPMs regarding their sensitivity and bandwidth. Thus, advancing MMG requires further research on magnetometers. Other magnetic sensing technologies that potentially can be used for biomagnetic recordings in the future are magnetoelectric sensors [273] and nitrogen-vacancy centres in diamond [267].

8 EMG and MMG of Voluntary Contractions

The voluntary force output of a skeletal muscle can be controlled by modulating the number of recruited motor units and their discharge frequency (see Chapter 2). Each motor neuron's discharge synchronously triggers an action potential in all the muscle fibres it innervates. Consequently, each motor neuron firing causes a compound muscle response, i.e., referred to as motor unit electric potential (MUEP) and motor unit magnetic field (MUMF), respectively. Based on this behaviour, a muscle can be considered a natural amplifier of motor neuron activity. However, because motor unit discharge patterns are not synchronised in time and motor unit responses have positive and negative phases, EMG or MMG of voluntary contractions yield complex interference signals. This chapter presents a series of simulations to support and guide the analysis of these challenging bio-signals. The basic simulation set-up is described in Section 8.1. Next, Section 8.2 demonstrates the fundamental interference patterns of EMG or MMG and discusses the associated challenges. The current gold standard to reconstruct the neural drive to a muscle is the decomposition of EMG signals into the spike trains of individual motor units. However, for non-invasive surface EMG measurements, the number of reliably decomposable motor units is limited by the distance between the active muscle fibres and electrodes and the body's electrical properties. The previous chapter demonstrated that non-invasive MMG signals are sparser than high-density EMG data. Due to this reason, it is hypnotised that measuring MMG could overcome some of the limitations of surface EMG-based motor unit decomposition. Thus, Section 8.3 tests the hypothesis that MMG is superior to EMG for distinguishing different motor unit responses. Finally, Section 8.4 presents a novel *in silico* trail framework that predicts upper bound accuracy estimates of surface EMG-based or non-invasive MMG-based motor unit decompositions.

8.1 In Silico Experiments

The multi-domain simulation framework introduced in Part II is used to investigate EMG or MMG signals of voluntary contractions. This section describes the specific simulation set-up for the *in silico* experiments presented in this chapter.

8.1.1 Tissue Geometry, Motor Unit Population and Discretisation

In Chapter 7, it was shown that the spatio-temporal patterns of compound muscle electric potentials and compound muscle magnetic fields depend on the tissue geometry, the spatial configuration of the muscle fibres, and the tissue properties. Here, a cube-shaped layered tissue model is used to exclude the potential influence of complex tissue geometries on the results presented. The edge lengths of the muscle sample are $L = 80\,\text{mm}$, $W = 40\,\text{mm}$ and $H = 40\,\text{mm}$ (see Figure 8.1). Further, a fat tissue layer of variable thickness, i.e., 0 mm, 5 mm and 20 mm, is added on top of the muscle. The muscle fibres are aligned with the longest edge of the muscle, yielding a fusiform muscle. To limit the computational complexity of the conducted simulations, a half-muscle is considered, i.e., the distance between the centre of the innervation zone and the myotendinous junction is 65 mm (see Figure 8.1).

Further, five different motor unit pools consisting of $N = 150$ motor units are simulated. Assuming an idealised circular shape of the motor unit territories, the anatomy of each motor unit is fully described by its centre and radius. The motor unit territory centres are randomly distributed within the muscle's cross-sectional area. Further, the radius of each motor unit territory is randomised according to a uniform distribution ranging from 3 mm to 5 mm. Thereby, it is noted that the motor unit territories can overlap with each other (see Figure 8.1). It is assumed that a motor unit's fibre load follows an exponential distribution, and the ratio of the innervation number of the largest motor unit to the smallest motor unit is roughly 100 [e.g., 81, 193]. To compute for each motor unit territory a local (continuous) fibre load, first, each point within the motor unit territory is weighted with a parameter w_k, i.e.,

$$w_k \;=\; \exp\left(\ln(100)\,\frac{(k-1)}{(N-1)}\right) \,+\, 1\ . \tag{8.1}$$

Next, the motor unit volume fractions f_{r}^k $(k = 1, ..., N)$ are calculated for each skeletal muscle material point:

$$f_{\mathrm{r}}^k \;=\; w_k \,/\, \sum_{m=1}^{N} w_m\ ,\ k = 1, ..., N\ . \tag{8.2}$$

In the last step, the motor unit territories are sorted such that the integral of the motor unit volume fraction over the whole muscle region increases with the motor unit index k. For each motor unit, the neuromuscular junctions are located in a plane orthogonal to the muscle fibre directions, which are randomly distributed in the innervation zone, i.e., spanning a length of 10 mm (cf. Figure 8.1). Further, the radius of the muscle fibres is uniformly distributed, i.e., 40 µm for the largest motor unit and 80 µm for the smallest motor unit. The anisotropy ratio of the extracellular conductivity tensor is set to 4. All other model parameters are adopted from Table 5.1.

For the discretisation of the tissue sample, the spacing of the grid points is 0.5 mm in the $x_{\mathrm{f}}^{\parallel}$-direction and 1 mm in the $x_{\mathrm{t}}^{\parallel}$-direction as well as in the $x_{\mathrm{t}}^{\perp}$-direction. Further, the step size of the global time step is set to $\Delta t = 0.1$ ms. The membrane models are solved with a step size of $\Delta t_{\mathrm{ode}} = 0.01$ ms. Virtual high-density EMG and high-density MMG signals are obtained by using a 10×7 array of sampling points that is centred between the innervation zone and the myotendinous junction (see Figure 8.1). The distance between the sampling points is 5 mm. While the high-density EMG array is placed on top of the muscle, the MMG array is 1 mm above the body surface. Further, sampling the model output after each fifth global time step yields a sampling frequency of 2000 Hz.

8.1.2 Simulating Voluntary Contractions

A muscle's force can be modulated by motor unit recruitment and rate coding (see Chapter 2). Here, a phenomenological approach integrating basic physiological knowledge is used to compute the motor neuron discharge times. In the presented *in silico* experiments, three different isometric contraction levels, i.e., low intensity, medium intensity and high intensity, are considered. First, a motor unit's recruitment threshold is assumed to increase with its size [109]. Hence, the number of active motor units increases with the contraction intensity. Further, it is assumed that the smallest motor unit exhibits the highest firing frequency [49, 208]. Thereby, the peak firing rate increases with the contraction intensity. The firing rate of the largest active motor unit is always set to 8 Hz [59]. Further, the firing frequencies for all other motor units are uniformly distributed between the minimum firing rate, i.e., 8 Hz, and the peak firing rate. For each contraction level, the firing rate decreases with the size of the motor units. Spike trains are

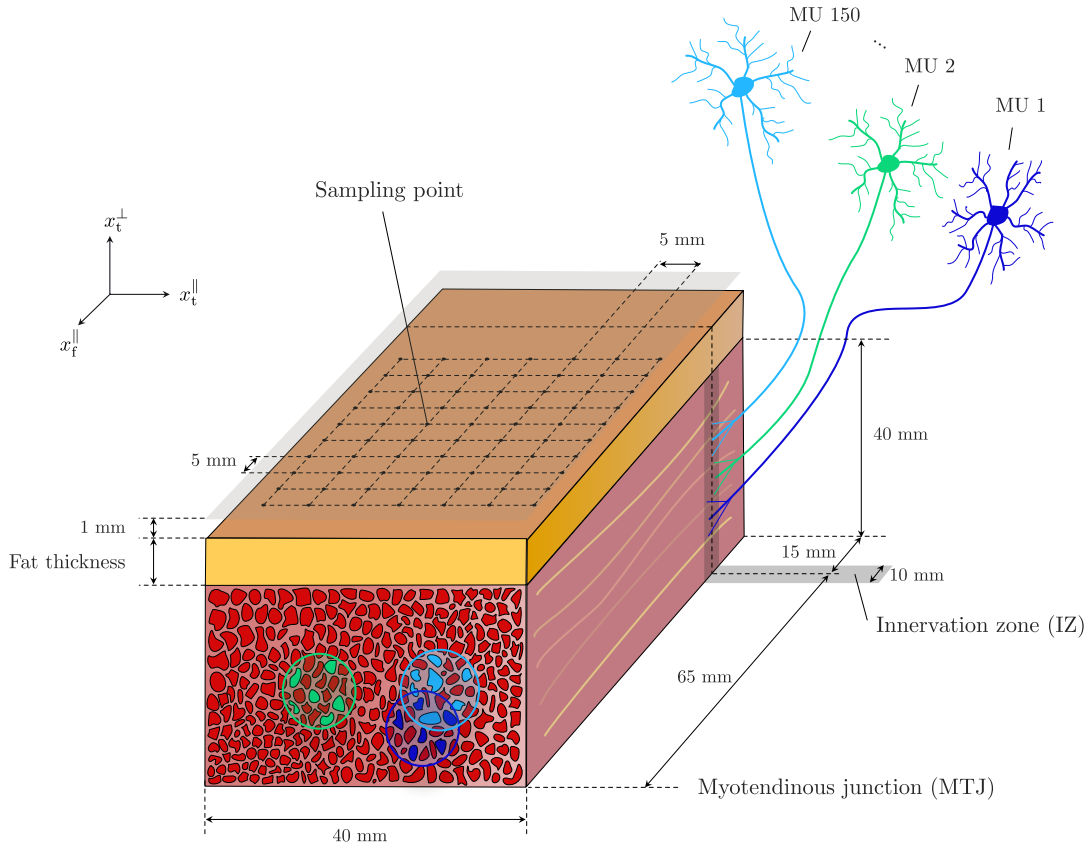

Figure 8.1: Schematic drawing illustrating the basic set-up of the simulations presented. For the virtual EMG, the sampling array is placed on the body surface. The virtual MMG array is 1 mm above the body surface (indicated by the transparent plane).

obtained by adding a random jitter of ±10 % to the base firings [33, 167], which are determined by the mean inter-spike interval. The parameters for simulating the three different contraction intensities are summarised in Table 8.1.

Contraction intensity	Number of recruited motor units	Peak firing rate
Low MVC	60	15 Hz
Medium MVC	100	20 Hz
High MVC	150	25 Hz

Table 8.1: Summary of model parameters for simulating the neural drive to the muscle.

8.2 The Fundamental Properties of EMG and MMG During Voluntary Contractions

The fundamentals of EMG and MMG of voluntary contractions are introduced by considering the interaction between two motor units. A linear signal model can describe the observed interference patterns. This generative model is the basis for discussing the challenges associated with decoding the neural drive to the muscle from bioelectromagnetic field measurements.

8.2.1 Constructive and Destructive Interference

To illustrate the fundamental properties of EMG and MMG of voluntary contractions, the interaction of two motor units from a randomly selected virtual test muscle is investigated (see Section 8.1.1). Thereby, the thickness of the subcutaneous fat tissue is 5 mm. The presented *in silico* experiments test the influence of the temporal delay of the motor unit discharge times when both motor units are simultaneously active. Hence, after simulating an isolated stimulus for each motor unit, temporal delays of 0 ms, 5 ms, 10 ms and 15 ms are considered.

Figure 8.2 exemplarily shows, for a single sampling point, that constructive or destructive interference can be observed depending on the time delay between the discharges of both motor units. When both motor units are activated synchronously, the RMS value of the EMG signal in a time window of 30 ms after the stimulus is 196.0 % of the RMS value obtained in a time window of 30 ms after an isolated stimulus of the second motor unit. Analogously, the relative RMS values of the MMG signals are 298.3 % for the $x_\mathrm{f}^{\parallel}$-component, 190.4 % for the $x_\mathrm{t}^{\parallel}$-component and 283.0 % for the $x_\mathrm{t}^{\perp}$-component. For a time delay of 10 ms, the relative RMS values in a time window of 30 ms after the stimulus of the second motor unit decrease to 72.3 % for the EMG, 82.8 % for the MMG's $x_\mathrm{f}^{\parallel}$-component, 84.1 % for the MMG's $x_\mathrm{t}^{\parallel}$-component and 123.9 % for the MMG's $x_\mathrm{t}^{\perp}$-component. Hence, this basic *in silico* experiment illustrates that the signal amplitude of EMG and MMG signals is complexly coupled to both the firing times of the motor neurons as well as the shape of the motor unit responses, i.e., the properties of the muscle.

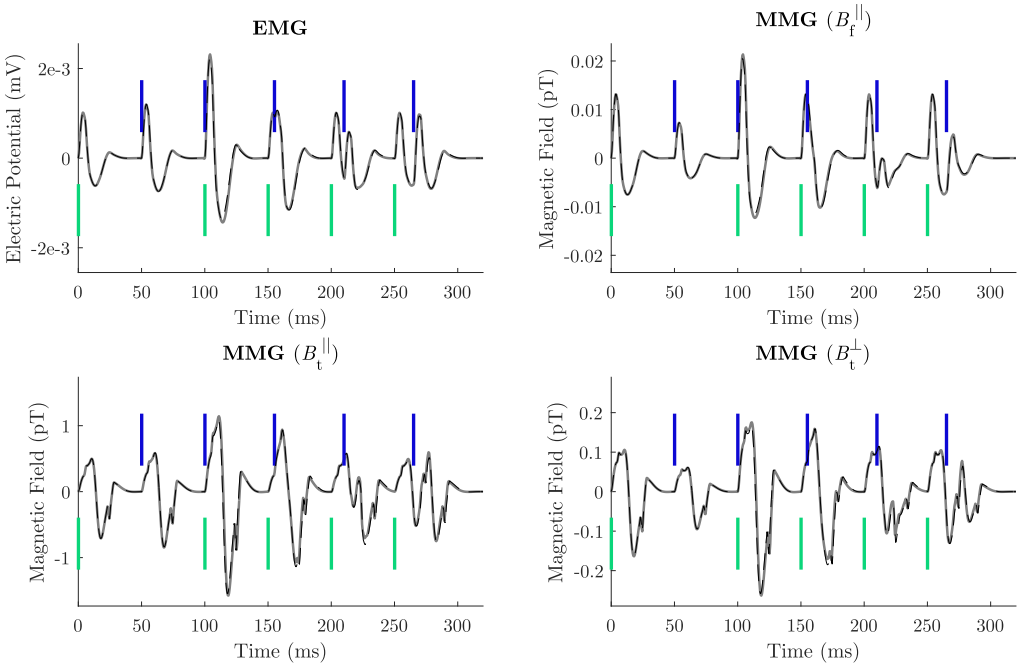

Figure 8.2: Interaction of two motor units observed from a single sampling point via EMG and all three components of the MMG. The sampling point is located midway between the innervation zone and the myotendinous junction, i.e., $x_\mathrm{f}^{\parallel} = 35\,\mathrm{mm}$ and $x_\mathrm{t}^{\parallel} = 20\,\mathrm{mm}$. The firings of the first motor unit are indicated in green, and the firings of the second motor unit are shown in blue. The solid grey line shows the EMG and MMG signals simulated with the multi-domain model, and the black dashed line shows the approximation obtained from Equation (8.3).

8.2.2 Generative Model for EMG and MMG

EMG and MMG of voluntary contractions can be described through a linear convolutive mixing model [cf. e.g., 44, 70]. For a multi-channel recording system with M channels, the EMG or MMG signal observed at the ith channel is given by

$$\psi_i^t \;=\; \sum_{k=1}^{N} \sum_{l=0}^{L-1} h_{ik}^l s_k^{t-l} \;,\; i = 1, ..., M \;. \tag{8.3}$$

The superscript t refers to a (discrete) time sample. From Equation (8.3), it is evident that the EMG or MMG measured during voluntary contractions is the superposition of signal components stemming from the individual motor units k ($k = 1, ..., N$). The contribution of each motor unit k is determined by the discharge times of the motor neuron, i.e., a binary spike train s_k^t, which is convolved by the corresponding motor unit response $\boldsymbol{H}_{ik} = [h_{ik}^0, ..., h_{ik}^{L-1}]^T$, i.e., the motor unit electric potential or motor unit magnetic field. Thereby, L denotes the number of time samples of the motor unit response.

The validity of this signal model, i.e., Equation (8.3), is tested by comparing the computed EMG or MMG signals to the results predicted by the multi-domain model. Figure 8.2 shows that for the interaction of two motor units (cf. Section 8.2.1) both models are almost perfectly in agreement. Considering all sampling points of the high-density EMG or MMG array, the relative L^2-error is 1.3 % for the EMG signal, 1.3 % for the MMG's $x_{\mathrm{f}}^{\parallel}$-component, 5.0 % for the MMG's $x_{\mathrm{t}}^{\parallel}$-component and 5.2 % for the MMG's $x_{\mathrm{t}}^{\perp}$-component. Further, Figure 8.3 summarises the results obtained from an *in silico* experiment computing the EMG signal and the MMG signals during the simultaneous activity of ten motor units. It is observed that the linear signal model closely approximates the muscle-induced bioelectromagnetic fields simulated with the multi-domain model. That is, the relative L^2-error for all discretisation points on the body surface is 0.2 % for the EMG, 0.2 % for the MMG's $x_{\mathrm{f}}^{\parallel}$-component, 1.1 % for the MMG's $x_{\mathrm{t}}^{\parallel}$-component and 1.0 % for the MMG's $x_{\mathrm{t}}^{\perp}$-component.

8.2.3 The Relation Between Contraction Intensity and Signal Amplitude

It was shown that EMG or MMG signals observed during voluntary contraction depend both on the neural drive to the muscle, i.e., through the spike trains s_k^t, as well as the muscle properties, i.e., through the motor unit responses h_{ik}^t. Hence, it is impossible to separate both effects explicitly. Nevertheless, different measures of the EMG amplitude are frequently used to describe the strength of the neural drive to the muscle. This section quantifies the uncertainty associated with methods that aim to estimate the neural drive to the muscle based on the amplitude of muscle-induced bioelectromagnetic fields. This uncertainty is caused by the inter-subject variability of the motor unit responses and the variability in the motor unit firings.

Five muscles with different motor unit territory distributions are considered to investigate the relation between the signal amplitude and the neural drive to the muscle (see Section 8.1). Thereby, for all muscles, the thickness of the subcutaneous fat tissue layer is 5 mm. After simulating a library of motor unit electric potentials and motor unit magnetic fields for each muscle, Equation (8.3) is used to predict the interference signals for three different contraction intensities. Thereby, the same spike trains are applied to all virtual muscles. High-density EMG signals and high-density MMG signals are simulated by considering an array of 10×7 sampling points, which is placed midway between the innervation zone and the myotendinous

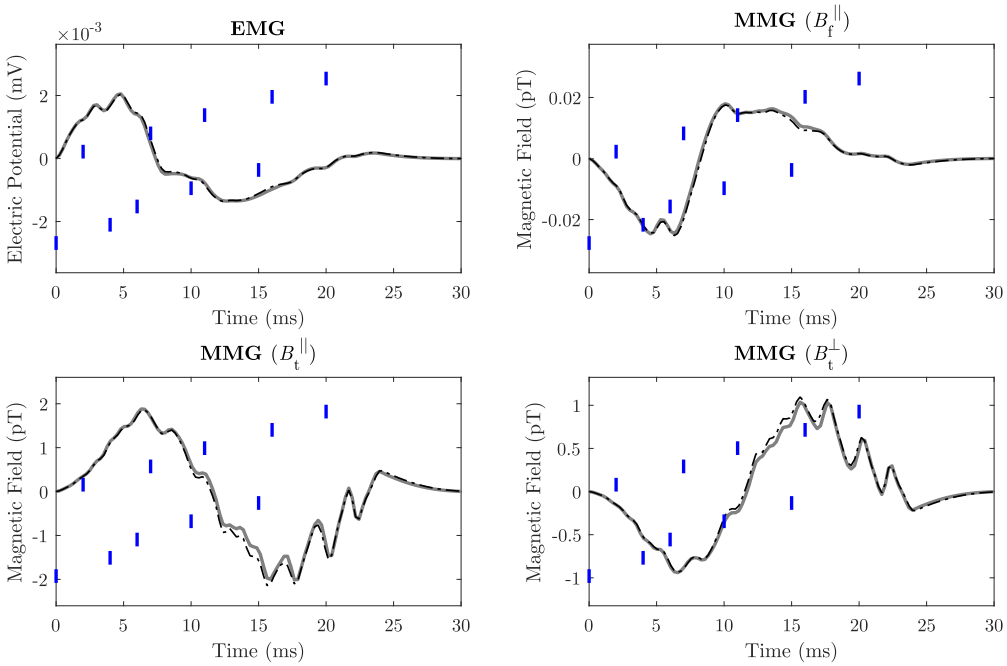

Figure 8.3: EMG and MMG signals caused by the activity of ten motor units. The solid grey line shows the signals predicted by the multi-domain model, and the dashed-dotted black line shows the linear approximation (see Equation (8.3)). Further, the vertical blue lines indicate the firing times of the motor units.

junction on the surface of the simulated tissue sample (see Figure 8.1). Estimates of the signal amplitudes are obtained by computing the mean RMS value across all high-density EMG or MMG sampling points.

Figure 8.4 shows that the amplitude of the EMG and all three components of the MMG monotonically increases with the contraction intensity. However, for the same neural drive to the muscle, the signal amplitude is variable across the population of the virtual muscles. Notably, the variability across the virtual muscles is more pronounced for the high-density EMG than the high-density MMG. Moreover, the lowest variability of the RMS values is observed for the MMG components orthogonal to the muscle fibres. For example, for the medium contraction level the coefficient of variation of the mean RMS values is 50.1 % for the EMG, 36.1 % for the MMG's $x_f^{\parallel}$-component, 19.1 % for the MMG's $x_t^{\parallel}$-component and 16.7 % for the MMG's $x_t^{\perp}$-component.

In summary, this section showcases the limitations of methods that aim to directly extract the neural drive to the muscle from the amplitude of an interference signal. For a more elaborated discussion on the factors affecting the amplitude of EMG signals, the reader is referred to the existing literature [cf. e.g., 45, 56, 67, 70, 76].

8.3 Similarity of Motor Unit Electric Potentials and Motor Unit Magnetic Fields

Given the limitations of methods that directly correlate the EMG amplitude and the neural drive to the muscle, the current gold standard for decoding the neural control of the muscle

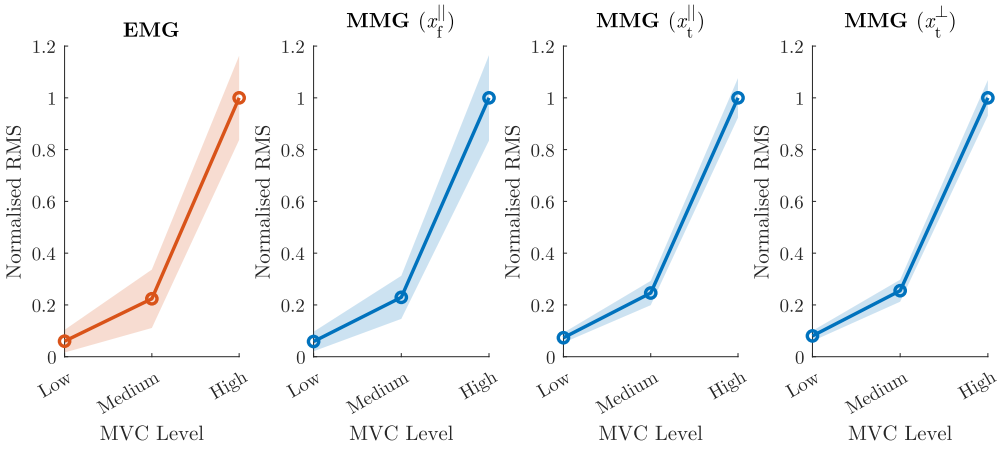

Figure 8.4: Relative RMS values for a high-density EMG array and all components of a high-density MMG array depending on the contraction intensity. All values are normalised to the mean RMS value at the highest contraction level.

is the decomposition of EMG signals into the spike trains of individual motor units. However, due to the distance between the active muscle fibres and the electrodes, surface EMG exhibits spatial low-pass filtering that depends on the electric properties of the body. This limits the number of motor units reliably decomposable from surface EMG. In contrast, the propagation of magnetic fields is not affected by biological tissues. This makes non-invasive MMG a promising method with the potential to overcome some of the limitations of surface EMG-based motor unit decomposition. This section investigates this hypothesis by comparing the similarity of simulated motor unit electric potentials and motor unit magnetic fields.

8.3.1 Measures of Similarity

A unique representation of the motor unit responses in a high-density EMG or MMG signal is a fundamental requirement to decompose interference signals into the spike trains of individual motor units. To quantify the uniqueness of motor unit responses, the cosine similarity is computed for all pairs of motor units included in the same pool of motor units. Therefore, the motor unit responses are aligned in time by maximising their channel-by-channel cross-correlation. The cosine similarity between the multi-channel motor unit responses of motor unit k and motor unit q is given by

$$S_{\cos}^{kq} = \frac{\sum_{l=0}^{L-1}\sum_{i=1}^{M} h_{ik}^{l} h_{iq}^{l}}{\sqrt{\sum_{l=0}^{L-1}\sum_{i=1}^{M}\left(h_{ik}^{l}\right)^2}\sqrt{\sum_{l=0}^{L-1}\sum_{i=1}^{M}\left(h_{iq}^{l}\right)^2}} \,. \tag{8.4}$$

Therein, M denotes the number of channels. Note that $S_{\cos}^{kq} = 0$ means that the kth and the qth motor unit response are orthogonal and hence uncorrelated. In contrast, $S_{\cos}^{kq} = 1$ indicates that the motor unit responses are identical.

8.3.2 Similarity for Exemplary Pairs of Motor Unit Responses

This section illustrates the theoretical advantage of MMG by comparing the similarity of pairs of motor unit electric potential and motor unit magnetic fields. The motor unit electric potentials and the motor unit magnetic fields are simulated with the multi-domain simulation

framework using the set-up described in Section 8.1.1.

Figure 8.5 considers for two pairs of motor units the similarity of the corresponding motor unit electric potentials and the motor unit magnetic fields observed from an array of 10×7 sampling points. It can be observed that for two motor units with spatially distinct territories, both the motor unit electric potentials and the motor unit magnetic fields can be visually distinguished in the temporal domain, see Figure 8.5B and Figure 8.5E. In detail, the cosine similarity across all channels is 0.90 for the motor unit electric potentials and 0.73 for the motor unit magnetic fields. Further, the minimum channel-by-channel cosine similarity is 0.54 for the motor unit electric potentials and 0.37 for the motor unit magnetic fields. Note that the motor unit magnetic fields have three channels for each sampling point, i.e., one for each magnetic field vector component.

However, if one considers two motor units in close physical proximity, the high-density motor unit electric potentials become nearly indistinguishable. This is quantitatively reflected in the cosine similarity, i.e., 0.99 across all channels and the minimum channel-by-channel cosine similarity is 0.96. In contrast, the motor unit magnetic fields are still visually distinguishable on some channels. The cosine similarity between the two high-density motor unit magnetic fields is 0.93. Further, the minimum channel-by-channel cosine similarity is 0.79. This example demonstrates that non-invasive MMG can provide better contrast between the two motor unit responses when it is hardly feasible to distinguish two motor units using surface EMG.

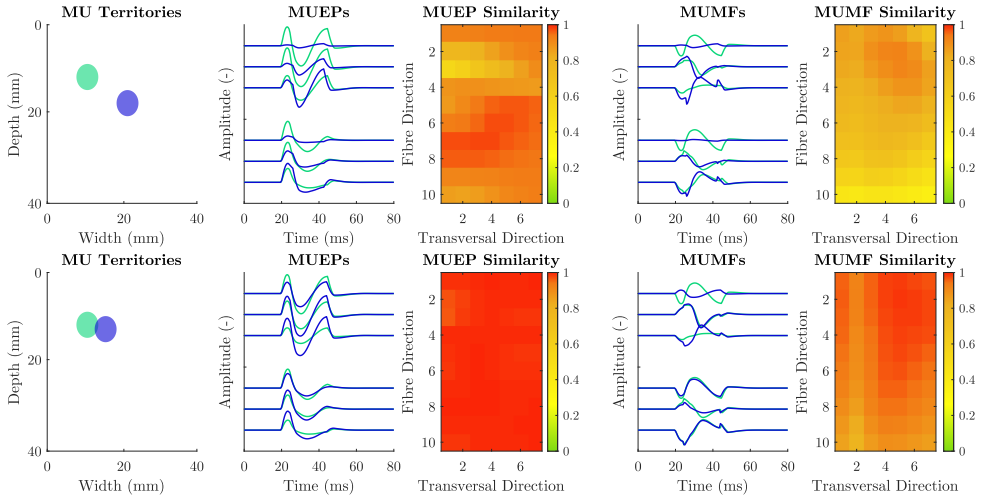

Figure 8.5: Illustrative example comparing the similarity of motor unit responses. The left column shows the territories of two arbitrarily chosen motor units, illustrated by blue and green colours. The second column shows the corresponding motor unit electric potentials on a few randomly selected channels of the high-density EMG signal. The third column shows the channel-by-channel cosine similarity between the two motor unit electric potentials. A value of zero (green) indicates uncorrelated motor unit responses and a value of 1 means that the motor unit responses are identical (red). The fourth column shows the motor unit magnetic fields on a few randomly selected channels of the high-density MMG signal. The last column shows the channel-by-channel cosine similarity between the two motor unit magnetic fields.

8.3.3 Similarity of the Motor Unit Responses Across the Whole Motor Unit Pool

The robust decomposition of a motor unit requires that the respective motor unit response is unique compared to all other motor unit responses. Hence, this section investigates five different motor unit populations and three different thicknesses of the subcutaneous fat tissue layers (see Section 8.1.1). Thereby, for each virtual muscle, the mean cosine similarity of the motor unit electric potentials as well as the motor unit magnetic fields across the muscle's motor unit pool is computed.

Figure 8.6 shows that the average cosine similarity of the motor unit magnetic fields is lower than for the motor unit electric potentials. For example, for a thickness of 5 mm of the subcutaneous fat tissue, the mean cosine similarity is 0.38 for the motor unit magnetic fields and 0.76 for the motor unit electric potentials. Further, with increasing thickness of the subcutaneous fat, for the motor unit electric potentials, the mean cosine similarity increases. In contrast, there is no significant relation between the cosine similarity of the motor unit magnetic fields and fat tissue thickness. In conclusion, it can be expected that more motor units can be decomposed from the high-density MMG than from the high-density surface EMG.

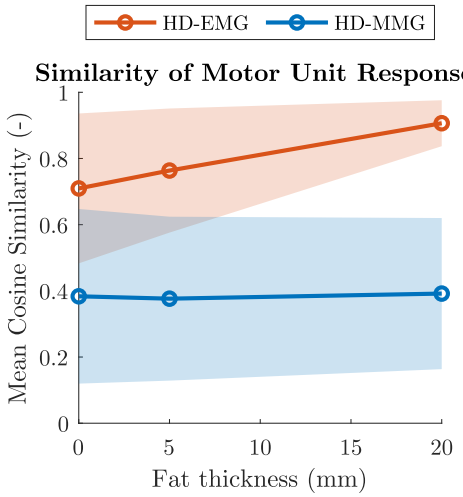

Figure 8.6: Mean cosine similarity of the motor unit electric potentials (red) and the motor unit magnetic fields (blue) across the whole motor unit pool depending on the thickness of the subcutaneous fat tissue. The markers denote the average values from all virtual muscles, and the shaded areas represent the corresponding standard deviations.

8.3.4 The Influence of the Spatial Configuration of the Motor Units

This section uses the *in silico* environment to examine the influence of the spatial configuration of the motor unit territories on the uniqueness of the corresponding motor unit electric potentials and motor unit magnetic fields. Hence, three motor units, i.e., superficial, centred and deep, from one virtual muscle are considered. The muscle has a fat tissue thickness of 5 mm. For each selected motor unit, the cosine similarity of the motor unit action signals is correlated with the spatial configuration of the motor unit territories. In detail, for each grid point of the muscle, the mean cosine similarity between the reference motor unit response and the motor unit responses of all motor units for which $f_{\mathrm{r}}^{k} > 0$ holds at the selected grid point is computed.

Figure 8.7 showcases that the uniqueness of the motor unit electric potentials correlates with the depth of the motor unit territory. That is, the fraction of the muscle's cross-sectional area with a mean cosine similarity larger than 0.9 is 3.0 % for the superficial motor unit, 18.4 % for the centred motor unit and 24.5 % for the deep motor unit. For the MMG, there is no considerable correlation between the depth of the motor units and the uniqueness of the motor unit magnetic fields. In detail, the fraction of the muscle's cross-sectional area with a mean cosine similarity larger than 0.9 is always less than 1 %. Thus, it is expected that the MMG decomposition will be less affected by variations in the depth of the motor units.

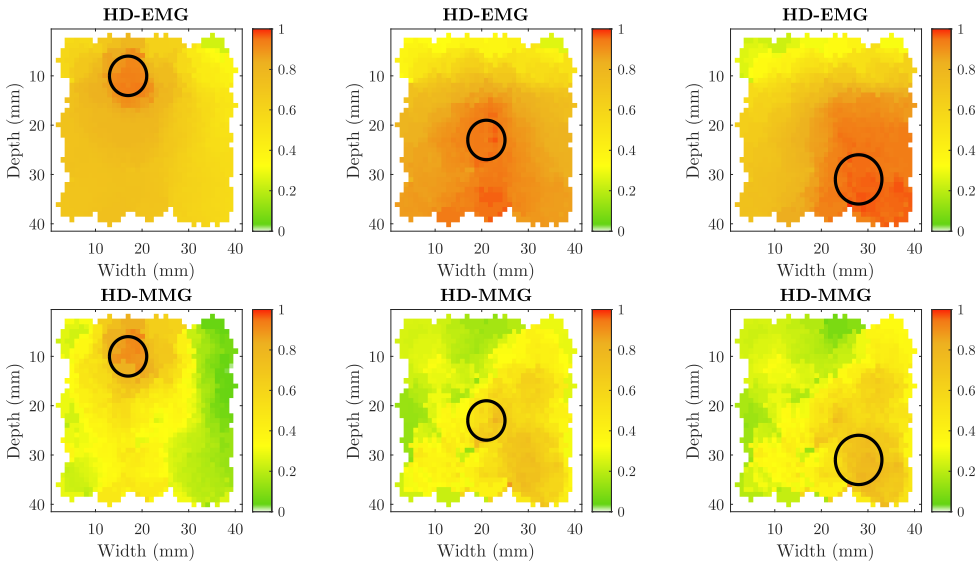

Figure 8.7: Uniqueness of three randomly selected motor unit electric potentials (top row) and motor unit magnetic fields (bottom row) depending on the (spatial) positions of the motor units. Black circles visualise the territories of the considered motor units. The colour map indicates the mean cosine similarity between the motor unit response of the selected motor unit and all other motor unit responses located at the respective grid point.

8.4 In Silico Trials for Investigating the Separability of EMG and MMG

In Section 8.2, it was shown that EMG and MMG of voluntary contractions share the same generative model. Solving the inverse problem, i.e., inverting Equation (8.3), allows to study individual motor units *in vivo*. This is known as motor unit decomposition. For surface EMG, this is possible by utilising blind source separation methods. However, the similarity of motor unit electric potentials limits the number of motor units that can be reliably decomposed. In Section 8.3, it was shown that motor unit responses are less similar when high-density MMG is measured instead of high-density EMG. Hence, this section investigates non-invasive MMG-based motor unit decomposition and compares the results to surface EMG-based motor unit decomposition.This is achieved by performing *in silico* trials that integrate the knowledge of the forward mixing model into state-of-the-art motor unit decomposition algorithms[1].

[1]The methods and results presented in this section have been elaborated in close collaboration with Lena Lehmann and Francesco Negro. The contributions of Lena and Francesco are greatly acknowledged

8.4.1 In Silico Framework for Predicting Upper Bound Accuracy Estimates of Motor Unit Decompositions

The motor unit responses are unknown when decomposing experimentally acquired EMG or MMG signals. Hence, motor unit decomposition requires the solution of an optimisation problem to estimate the forward mixing model. Thereby, the selected algorithm strongly affects the decomposition results. To focus on the influence of the signal properties, this work introduced an *in silico* trial platform that can predict upper-bound accuracy estimates of motor unit decompositions [cf. 142]. In short, for simulated data, the motor unit responses are known. They can, therefore, be directly integrated into the workflow of state-of-the-art (blind source separation-based) motor unit decomposition algorithms [cf. e.g., 30, 125, 194]. Hence, for a set of virtual muscles, the motor unit electric potentials and the motor unit magnetic fields are simulated with the multi-domain simulation framework (see Part II). Further, interference signals corresponding to different contraction intensities are computed via Equation (8.3). Finally, the motor unit spike trains are optimally reconstructed with the proposed methodology. The proposed approach is schematically illustrated in Figure 8.8.

First, it is exploited that any convolutive mixing model with finite impulse response filters (see Equation (8.3)) can be transformed into an instantaneous mixture of extended sources and, hence, a matrix system [e.g., 194]. Therefore, the signal ψ_i^t, consisting of M observations at time frame t, is expanded by K time instances to yield an extended observation vector $\widetilde{\boldsymbol{\psi}}^t \in \mathbb{R}^{KM}$:

$$\begin{aligned} \widetilde{\boldsymbol{\psi}}^t \;=\; \Big[&\psi_1^t, \psi_1^{t-1}, \dots, \psi_1^{t-(K-1)}, \dots, \\ &\psi_M^t, \psi_M^{t-1}, \dots, \psi_M^{t-(K-1)}\Big]^T . \end{aligned} \tag{8.5}$$

Here, the chosen extension factor K equals the dimension of the motor unit responses L. The extended observations $\widetilde{\boldsymbol{\psi}}^t$ can be computed by

$$\widetilde{\boldsymbol{\psi}}^t \;=\; \widetilde{\boldsymbol{H}}\, \tilde{\boldsymbol{s}}^t \,. \tag{8.6}$$

Therein, the extended spike train vector $\tilde{\boldsymbol{s}}^t \in \mathbb{R}^{N(L+K-1)}$ is derived from the spike trains s_k^t, i.e.,

$$\begin{aligned} \tilde{\boldsymbol{s}}^t \;=\; \Big[&s_1^t, s_1^{t-1}, \dots, s_1^{t-(L-1)-(K-1)}, \dots, \\ &s_N^t, s_N^{t-1}, \dots, s_N^{t-(L-1)-(K-1)}\Big]^T . \end{aligned} \tag{8.7}$$

Further, the mixing matrix of the extended system $\widetilde{\boldsymbol{H}} \in \mathbb{R}^{KM \times N(L+K-1)}$ is given by

$$\widetilde{\boldsymbol{H}} \;=\; \begin{bmatrix} \widetilde{\boldsymbol{H}}_{11} & \widetilde{\boldsymbol{H}}_{12} & \dots & \widetilde{\boldsymbol{H}}_{1N} \\ \widetilde{\boldsymbol{H}}_{21} & \widetilde{\boldsymbol{H}}_{22} & \dots & \widetilde{\boldsymbol{H}}_{2N} \\ \dots & \dots & \dots & \dots \\ \widetilde{\boldsymbol{H}}_{M1} & \widetilde{\boldsymbol{H}}_{M2} & \dots & \widetilde{\boldsymbol{H}}_{MN} \end{bmatrix} , \tag{8.8}$$

where the block matrices $\widetilde{\boldsymbol{H}}_{ij} \in \mathbb{R}^{K \times (L+K-1)}$ are defined as

$$\widetilde{\boldsymbol{H}}_{ik} \;=\; \begin{bmatrix} h_{ik}^0 & h_{ik}^1 & \dots & h_{ik}^{L-1} & 0 & \dots & 0 \\ 0 & h_{ik}^0 & \dots & h_{ik}^{L-2} & h_{ik}^{L-1} & \dots & 0 \\ \cdot & \cdot & \dots & \cdot & \cdot & \dots & \cdot \\ \cdot & \cdot & \dots & \cdot & \cdot & \dots & \cdot \\ \cdot & \cdot & \dots & \cdot & \cdot & \dots & \cdot \\ 0 & 0 & \dots & \cdot & \cdot & \dots & h_{ik}^{L-1} \end{bmatrix} . \tag{8.9}$$

Therein, h_{ik}^t denote the motor unit responses.

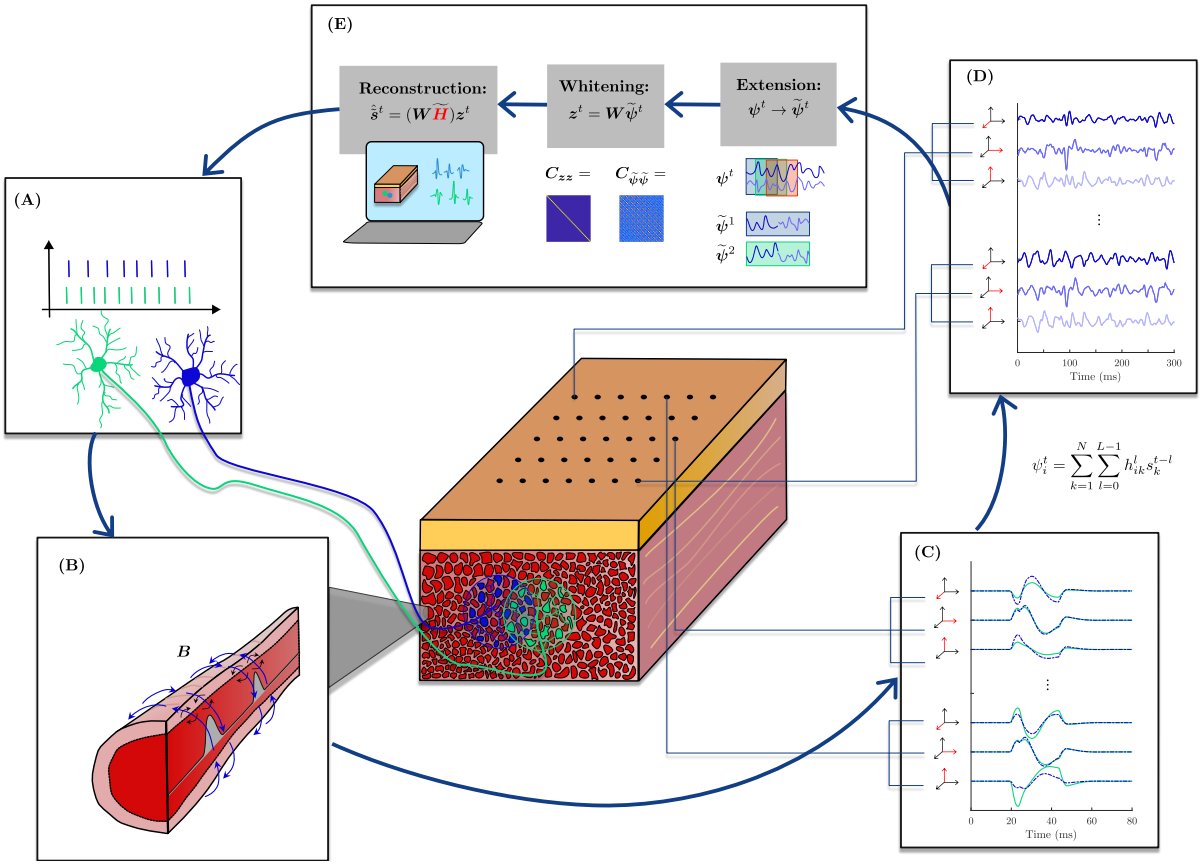

Figure 8.8: A-D: Schematic illustration of the generative model of MMG during voluntary contractions. (A) The discharge patterns of motor neurons in the spinal cord control the activity of skeletal muscles. (B) Every neural stimulus at a muscle fibre's neuromuscular junction triggers a muscle fibre action potential. (C) The spatiotemporal summation of the action potentials yields a characteristic motor unit magnetic field (MUMF) for each motor unit. (D) The simultaneous activity of multiple motor units mixes the motor unit magnetic fields according to the firing instances of the motor units. (E) Concept of a state-of-the-art motor unit decomposition algorithm. Instead of solving a blind source separation problem, we use the known motor unit responses to obtain upper-bound decomposition performance estimates.

Instead of directly inverting Equation (8.6), the signal extension is followed by a whitening transformation [cf. e.g., 134]. This linear transformation is used to decorrelate the signals, i.e.,

$$\boldsymbol{z}^t \;=\; \boldsymbol{W}\widetilde{\boldsymbol{\psi}}^t \;, \tag{8.10}$$

such that the covariance matrix of the extended observations, i.e., $\boldsymbol{C_{zz}}$, is the identity matrix (see Figure 8.8E). Here, ZCA (zero-phase component analysis) whitening is applied [144], in which the whitening matrix $\boldsymbol{W}$ is constructed from the eigendecomposition of the extended signals covariance matrix $\boldsymbol{C}_{\widetilde{\boldsymbol{\psi}}\widetilde{\boldsymbol{\psi}}}$, i.e.,

$$\boldsymbol{W} \;=\; \boldsymbol{V}\boldsymbol{D}^{-\frac{1}{2}}\boldsymbol{V}^T \;. \tag{8.11}$$

Therein, $\boldsymbol{D}$ is a diagonal matrix containing in increasing order the eigenvalues e_j $(j = 1, ..., KM)$ of the extended signals covariance matrix $\boldsymbol{C}_{\widetilde{\boldsymbol{\psi}}\widetilde{\boldsymbol{\psi}}}$ and $\boldsymbol{V}$ is the corresponding eigenvector matrix. Note that eigenvalues that are numerically zero, i.e., $e_j < \varepsilon \cdot KM$, with ε denoting the modulus of the distance from the maximum eigenvalue to the next larger floating point number, are

discarded for the calculation of the whitening matrix $\boldsymbol{W}$. Accordingly, the mixing model for the extended and whitened observations reads

$$\boldsymbol{z}^t \;=\; \boldsymbol{W}\widetilde{\boldsymbol{H}}\;\tilde{\boldsymbol{s}}^t \;=\; (\boldsymbol{W}\widetilde{\boldsymbol{H}})\;\tilde{\boldsymbol{s}}^t\;. \tag{8.12}$$

Therein, the mixing matrix $(\boldsymbol{W}\widetilde{\boldsymbol{H}})$ is equivalent to the extended and whitened motor unit responses. Next, the motor unit spike trains are estimated by approximating a solution for the linear system given in Equation (8.12). For the presented *in silico* trials, this is achieved by correlating the whitened motor unit responses with the extended and whitened signal $\boldsymbol{z}^t$, i.e.,

$$\begin{aligned}\hat{s}_k^t \;&=\; (\boldsymbol{W}\widetilde{\boldsymbol{h}}_k)^T\boldsymbol{z}^t\;,\\ \widetilde{\boldsymbol{h}}_k \;&=\; \Big[h_{1k}^{L-1}, h_{1k}^{L-2}, ..., h_{1k}^{0}, ...,\\ &\qquad h_{Mk}^{L-1}, h_{Mk}^{L-2}, ..., h_{Mk}^{0}\Big]^T\;.\end{aligned} \tag{8.13}$$

Therein, $\hat{s}_k^t$ is the reconstructed spike train of motor unit k at the discrete time instance t. Further, $\widetilde{\boldsymbol{h}}_k$ denote the extended motor unit responses. Notably, the motor unit responses need to be sorted from the last to the first time instance. The evaluation of Equation (8.13) is impossible for experimentally acquired signals as the mixing matrix is unknown. Hence, inverting Equation (8.12) requires solving a blind source separation problem.

Ultimately, the estimated spike trains $\hat{s}_k^t$ yield a real number for each time frame and motor unit (cf. Figure 8.9). For each motor unit k, the relative size of $\hat{s}_k^t$ measures the probability that a discharge occurs at time frame t. To obtain for each motor unit k a binary spike train $\hat{s}_k'^t$, a peak detection method is applied to the estimated spike trains $\hat{s}_k^t$. Further, the k-means clustering algorithm [79, 157] is applied to identify (potential) false-positive firings, i.e., separating the spikes into two clusters whereby the cluster centroids are initialised by the minimum peak height and the maximum peak height, respectively.

8.4.2 Measures of Decomposition Performance

Different performance metrics are computed to evaluate the separability of high-density EMG and MMG. Therefore, the predicted spikes are classified for each motor unit k $(k = 1, ..., N)$ into the true-positive spikes TP^k that represent the firings that appear in the true spike train s_k^t and in the predicted spike train $\hat{s}_k'^t$ with a maximal delay of $\pm 0.5\,\mathrm{ms}$. Further, the false-positive spikes FP^k are the firings only included in the predicted spike train $\hat{s}_k'^t$ and the false-negative spikes denote the firings that are only included in the true spike train s_k^t. Thereby, for each motor unit k $(k = 1, ..., N)$ the rate-of-agreement RoA^k is given by

$$\mathrm{RoA}^k \;=\; \frac{|\mathrm{TP}^k|}{|\mathrm{TP}^k| + |\mathrm{FP}^k| + |\mathrm{FN}^k|}\;, \tag{8.14}$$

where $|\mathrm{TP}^k|$ is the number of true-positive spikes, $|\mathrm{FP}^k|$ is the number of false positive spikes and $|\mathrm{FN}^k|$ is the number of false-negative spikes. The uncertainty of identifying the firings of motor unit k from a given interference signal is evaluated by computing for each motor unit k $(k = 1, ..., N)$ the silhouette coefficient [cf. e.g., 194], i.e.,

$$\mathrm{SIL}^k \;=\; \frac{\sum\limits_{p\in\mathrm{TP}^k} D^{pk}_{\mathrm{nospike}} - \sum\limits_{p\in\mathrm{TP}^k} D^{pk}_{\mathrm{spike}}}{\max\left(\sum\limits_{p\in\mathrm{TP}^k} D^{pk}_{\mathrm{spike}}, \sum\limits_{p\in\mathrm{TP}^k} D^{pk}_{\mathrm{nospike}}\right)}\;. \tag{8.15}$$

Therein, D^{pk}_{spike} is the euclidean distance between a true positive point of the estimated spike train $\hat{s}^p_k$ and the mean value of all estimated true positive spike points $\bar{\hat{s}}_{p\in\text{TP}^k}$, i.e., $D^{pk}_{\text{spike}} = \|\hat{s}^p_k - \bar{\hat{s}}_{p\in\text{TP}^k}\|$. Accordingly, D^{pk}_{nospike} is the euclidean distance between a true positive value of the estimated spike train $s^p_{k,\text{est}}$ and the mean value of all remaining estimated spike points not included in the set of the true-positive spikes $\bar{\hat{s}}_{p\notin\text{TP}^k}$, i.e., $D^{pk}_{\text{spike}} = \|\hat{s}^p_k - \bar{\hat{s}}_{p\notin\text{TP}^k}\|$. For $\text{SIL}^k < 0.9$, a motor unit is considered to be reliably decomposable [194].

8.4.3 Upper Bound Accuracy Estimates for EMG-Based and MMG-Based Motor Unit Decompositions

The *in silico* trials that predict upper bound accuracy estimates for the decomposition of high-density EMG and high-density MMG comprise 45 independent computational experiments. Five different motor unit pools are generated, and motor unit electric potential libraries and motor unit magnetic field libraries are simulated for three different fat tissue layers (see Section 8.1.1). For these 15 virtual muscles 30 s long steady isometric contractions are simulated via Equation (8.3) and repeated for three different contraction intensities, i.e., low MVC, medium MVC and high MVC. The interference signals obtained from these simulations are analysed with the decomposition framework introduced in Section 8.4.1.

Figure 8.9 shows for three motor units the spike trains that are estimated from high-density EMG (top row) and high-density MMG (bottom row). The first motor unit can be perfectly reconstructed from both high-density EMG and high-density MMG, i.e., the rate-of-agreement is 100 %. Further, the robustness of the decomposition is reflected in the silhouette coefficients, which are 0.98 for the high-density EMG and 0.97 for the high-density MMG. The second motor unit is considered to be reliably identifiable from both high-density EMG, i.e., SIL = 0.91, and high-density MMG, i.e., SIL = 0.95. However, while the spike train is perfectly reconstructed from the high-density MMG signal, the rate-of-agreement is only 92.6 % for the EMG-based decomposition. The last exemplary selected motor unit can only be reliably identified from the high-density MMG. The poor reconstruction of the spike train obtained from the high-density EMG is reflected in the silhouette coefficient and the rate-of-agreement. That is, the silhouette coefficient is 0.78. This is considerably lower than the threshold value of 0.9. Further, the rate-of-agreement is only 5.2 %.

Figure 8.10 summarises the results of all conducted *in silico* trials. The fraction of separable motor units, i.e., the number of motor units with $\text{SIL}^k > 0.9$ divided by the number of active motor units, is related to the thickness of the subcutaneous fat and the contraction intensity. For both high-density EMG and high-density MMG, the fraction of separable motor units decreases with the thickness of the fat tissue layer. Further, the fraction of separable motor units negatively correlates with the contraction intensity. Notably, for all conditions considered, the decomposition performance of the high-density MMG is superior to that of the high-density EMG. In detail, the fraction of separable motor units increases between 56 % and 116 % when decomposing high-density MMG instead of high-density EMG. The accuracy of the spike train estimation is reflected in the rate-of-agreement. That is, the mean rate-of-agreement for the set of reliably decomposable motor units is 98.1 % for the high-density EMG and 99.7 % for the high-density MMG. The mean rate-of-agreement for the motor units that are classified as not reliably identifiable, i.e., $\text{SIL}^k < 0.9$, is 20.5 % for the high-density EMG and 64.3 % for the high-density MMG. This indicates that the chosen thresholding method might underestimate the potential performance benefit when decomposing high-density MMG instead of high-density surface EMG.

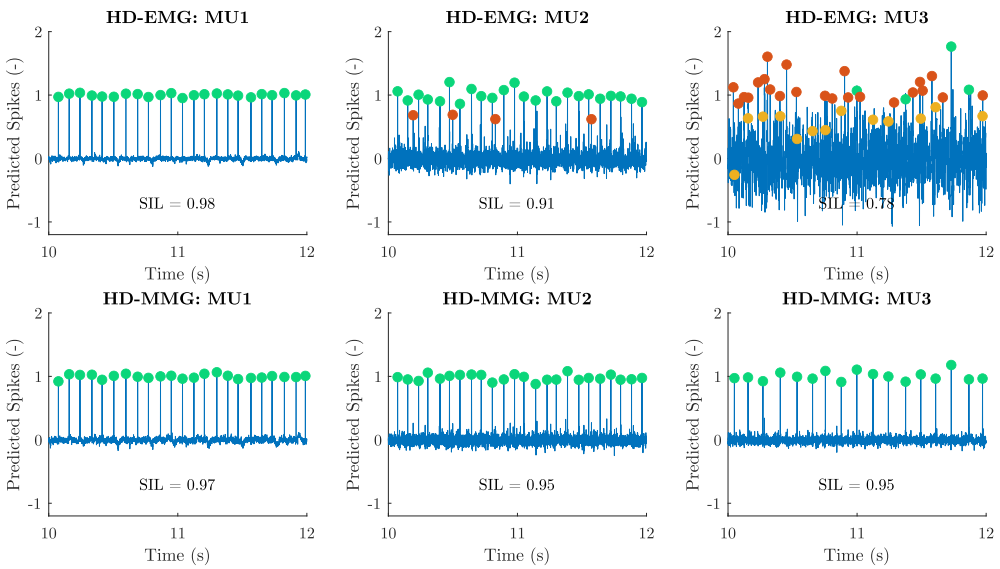

Figure 8.9: Exemplary spike trains estimated from high-density EMG (top row) and high-density MMG (bottom row). Each column represents one randomly selected motor unit. Green circles correspond to true positive spikes, red circles to false positive spikes, and orange circles to false negative spikes. All predicted spike trains are normalised to the mean values at the true positive spikes.

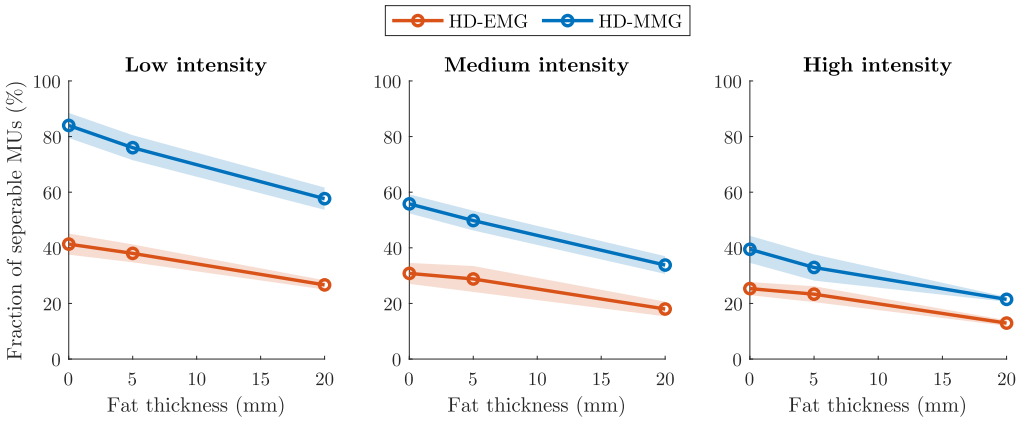

Figure 8.10: Fraction of motor units that can be reliably identified by decomposing high-density EMG (red) or high-density MMG (blue). All results are shown for three different contraction intensities (left to right) depending on the thickness of the subcutaneous fat tissue layer. The markers indicate mean values, and the shaded areas represent the corresponding standard deviations.

8.4.4 Difference in Separable Motor Units

The previous section demonstrated that high-density MMG can decompose more motor units than high-density surface EMG. This section investigates if there is a difference between motor units which can be decomposed from MMG and EMG. Figure 8.11A subdivides the motor units classified as reliably decomposable into three groups. That is, 25 % of the motor units can be reliably decomposed from both high-density EMG and high-density MMG, 1 % of the motor units are only identifiable from high-density EMG and 19 % of the motor units can only be reconstructed from high-density MMG. In summary, non-invasive MMG-based motor

unit decomposition nearly identifies all motor units that can be decomposed from high-density surface EMG. However, the MMG decomposition allows to observe motor units that cannot be identified with the EMG-based decomposition.

Next, it is investigated if the motor units detected only through the MMG-based decompositions have common characteristics. Figure 8.11B and Figure 8.11C map for both EMG and MMG the fraction of identifiable motor units to the anatomical position of the motor units. It can be observed that the EMG-based decomposition has a strong bias to detect superficial motor units. In detail, when the muscle is subdivided into a superficial part and a deep part, 67 % of the motor units from the superficial part are classified as separable. However, only 4 % of the motor units from the deep part are classified as detectable. The MMG-based motor unit decomposition also tends to identify more superficial motor units, cf. Figure 8.11C. However, considerably more deep motor units can be reliably decomposed, i.e., 88 % of the superficial motor units and 41 % of the deep motor units are classified as detectable.

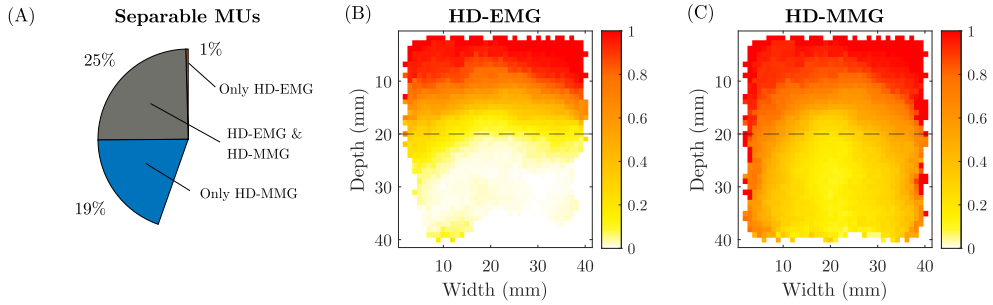

Figure 8.11: (A) Fraction of motor units reliably decomposable in all *in silico* trials. (B) Fraction of motor units identifiable with HD-EMG depending on the spatial position of the motor units. (C) Fraction of motor units identifiable with HD-MMG depending on the spatial position of the motor units. The dashed horizontal lines in (B) and (C) show the boundary between the muscle's superficial and deep parts.

8.4.5 Relevance of MMG Properties

This section examines which properties of the MMG are particularly relevant for obtaining good decomposition results. First, the relevance of the individual MMG components is examined. Hence, the proposed *in silico* motor unit decomposition framework (cf. Section 8.4.1) is applied to each MMG component individually, i.e., the $x_{\mathrm{f}}^{\parallel}$-component, the $x_{\mathrm{t}}^{\parallel}$-component and the $x_{\mathrm{t}}^{\perp}$-component. From Figure 8.12A, it can be observed that the fraction of separable motor units for the individual MMG components is between the values of high-density EMG-based decomposition and high-density (vector) MMG-based decomposition. Notably, the MMG components transversal to the muscle fibre direction yield a better decomposition performance than the MMG component aligned with the muscle fibres. The fraction of separable motor units is highest for the MMG component normal to the body surface. In detail, defining the vector MMG-based decomposition as a reference solution, the fraction of separable motor units decreases by 34.4 %, 24.4 % and 18.0 %, for the scalar MMG components $x_{\mathrm{f}}^{\parallel}$, $x_{\mathrm{xf}}^{\parallel}$ and $x_{\mathrm{xf}}^{\perp}$, respectively.

The magnetic field is a three-dimensional vector field. Hence, when using vector magnetometers, a high-density MMG signal has three times more channels for the same number of sampling points than a corresponding high-density EMG signal. Therefore, it is investigated if the higher

number of channels causes the superior separability of high-density MMG signals. This is tested by applying the decomposition workflow to two data sets only considering every third and every sixth MMG sensor. The corresponding decomposition results are summarised in Figure 8.12B. It can be observed that with only 12 vector magnetometers, the high-density MMG decomposition identifies more motor units than the EMG-based decomposition, which uses an array of 70 electrodes. Further, for an array with 24 vector magnetometers, the decomposition performance is nearly as good as for the 70-MMG-sensors case. In detail, using only every third and every sixth MMG sensor decreases the fraction of separable motor units by 2.6 % and 34.2 %, respectively. Hence, it is concluded that measuring a vector field instead of a scalar field is the most important feature of the MMG to explain its superior decomposition performance.

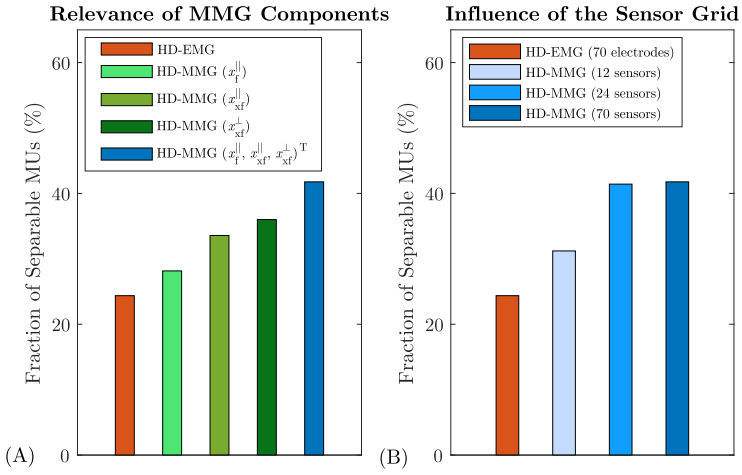

Figure 8.12: Fraction of separable motor units considering all *in silico* trials. (A) Decomposition performance for the individual MMG components. (B) Decomposition performance when using a reduced number of MMG sensors.

8.5 Summary and Discussion

This chapter investigates the use of EMG and MMG to decode the voluntary drive to a muscle through simulations. First, it is shown that both EMG and MMG signals exhibit positive and destructive interference. This behaviour can be described by a linear convolutive model [44, 70], which depends on the firing instances of the motor neurons and the motor unit responses. Hence, signals stemming from voluntary contractions depend on the neural drive to the muscle and the state of the muscle itself [cf. e.g., 45, 67, 70]. Therefore, no univocal relation exists between the voluntary drive to the muscle and the signal amplitude (see Section 8.2.3). Thus, the current gold standard for decoding the neural drive to a muscle *in vivo* is decomposing (high-density) EMG signals [11, 177] into the firing times of individual motor units [e.g., 30, 47, 124, 194]. For surface EMG, the similarity of the motor unit electric potentials limits the number of motor units that can be reliably decomposed [75]. This is caused by the body's low-pass filtering effect. In Section 8.3, it is shown that non-invasive high-density MMG is superior over high-density surface EMG to discriminate different motor units, i.e., particularly for motor units with overlapping territories as well as for motor units located deep within the muscle. This makes MMG-based motor unit decomposition a promising alternative to the well-established EMG-based decomposition.

In Section 8.4, a novel *in silico* trial framework is introduced to predict upper bound accuracy estimates of motor unit decompositions. Using an *in silico* testing framework has several advantages. Decomposing experimentally recorded EMG or MMG signals requires solving a blind source separation problem. Thereby, the results are influenced by the selected decomposition algorithm. In contrast, one can consistently achieve the best achievable decomposition in the presented *in silico* testing framework. This is possible as one can use the knowledge about the forward model to solve the inverse problem. Yet, as the motor unit decomposition problem is typically ill-conditioned, even with the full knowledge of the forward model, a perfect reconstruction of the spike trains is only sometimes feasible. Further, during *in vivo* experiments, the biophysical properties of the body are associated with considerable uncertainty. This makes it very challenging to relate the results of motor unit decompositions and the properties, the anatomy and the function of the body. This work shows that the decomposition goodness for both EMG and MMG is negatively correlated with subcutaneous fat tissue thickness and contraction intensity. This is consistent with decomposition results from experimentally measured surface EMG signals [e.g., 52, 75, 203], even if other factors may play a role [250]. The simulation environment also allows us to systematically study the differences between EMG-based and MMG-based motor unit decomposition. Notably, the decomposition of high-density MMG detects nearly all motor units that can be decomposed from the corresponding high-density EMG signal. However, while surface EMG-based decomposition is limited to detecting motor units up to a depth of approximately 20 mm, the non-invasive MMG-based decomposition can also decompose deeper motor units. The predicted depth limit of the surface EMG-based motor unit decomposition is in agreement with experimental observations [cf. 82, 220]. This underlines the predictive power of the presented *in silico* trials. Finally, in Section 8.4.5, it is shown that the most important property for explaining the MMG's superior separability is that a three-dimensional vector field is considered. This property is more important than the fact that magnetic fields propagate differently than electric fields in the body. The latter is often considered as the most relevant advantage of MMG.

The simulation results presented in this chapter are upper-bound accuracy estimates of motor unit decompositions. Whether the theoretical advantages of MMG-based motor unit decomposition also apply to experimentally measured signals depends on many factors. The simulations presented assumed ideal magnetometers. Yet, magnetometers that are currently used to measure biomagnetic fields, most importantly, the superconducting quantum interference device (SQUID) [e.g., 35, 143] and optically pumped magnetometers (OPMs) [e.g., 14, 95, 205, 231], still have some limitations for high-density MMG measurements. For example, SQUIDs require cryogenic cooling. Hence, SQUIDs must be placed several centimetres away from the skin. Further, SQUIDs are rigid devices (typically in a helmet-like geometry) that do not provide the flexibility required to cover different muscles. OPMs can overcome those limitations. However, OPMs still have shortcomings regarding the bandwidth (most sensors act as a low-pass filter with a cutoff frequency in the range of 150 Hz to 300 Hz) and the achievable grid density (typical sensor footprint sizes are in the range of 1 cm^2 to 4 cm^2). The application of other magnetometers to measure MMG is currently subject to basic research, for example, magnetoelectric sensors [273] or nitrogen-vacancy centres [267]. Further, it was assumed that the signals are not affected by noise. However, experimentally measured EMG or MMG signals are affected by different sources of physiological noise, e.g., cross-talk from other muscles or (small) motions, and non-physiological noise, e.g., ambient electromagnetic fields or imperfections of the detection system. The influence of these factors needs to be examined in the future. We also note that solving a blind source separation problem strongly depends on the implemented optimisation schemes. Moreover, the utilised biophysical model is

an idealised representation of the underlying physiology and anatomy. For example, the motor units are characterised by the mean firing rate, muscle fibre diameter, territory, and fibre load. However, the respective parameters' distribution and the corresponding assumptions' validity might vary considerably between different muscles, subjects or patients. This shortcoming is substantiated by the fact that we considered an idealised cube-shaped tissue geometry. Despite the advantage that geometrical effects do not play a role in the presented results, the influence of muscle geometry needs to be explored in the future. This can easily achieved by applying the proposed methodology to realistic muscle geometries discretised by the finite element method [cf. e.g., 159, 185, 234].

This chapter shows that high-density MMG can become the new gold standard for recording single motor unit activity non-invasively and *in vivo*. Further experimental research is required to prove the theoretical predictions presented within this work. This should be feasible within the next decade. The proposed *in silico* decomposition framework can be used to optimise high-density MMG recording systems, establish a systematic understanding of motor unit decomposition results, and benchmark the performance of motor unit decomposition algorithms.

9 Summary, Discussion and Conclusion

9.1 Summary and Context

EMG is a well-established experimental methodology to study the neuromuscular system *in vivo*. The associated challenges, as well as its limitations, have been discussed extensively in the scientific literature [e.g., 45, 67, 70, 175]. In contrast, MMG represents an emerging method that has recently gained attention due to progress in the field of sensor technology [e.g., 14, 95, 205, 231] and the signal's physical properties [e.g., 18, 20, 140, 154, 270]. EMG and MMG measure the same biophysical phenomenon, i.e., the electric activation of skeletal muscles, and hence, contain similar information on the body's function. However, no systematic comparison between both signals exists. Thus, this work introduces a computational model for simulating muscle-induced bioelectromagnetic fields. This enables detailed *in silico* investigations of EMG and MMG, which can provide insights into muscle-induced bioelectromagnetic fields that would not be easily accessible using experimental methods. Hence, the presented work contributes to developing methodologies for studying the neuromuscular system *in vivo*.

In summary, a novel bioelectromagnetic multiscale model of skeletal muscle tissue was developed, see Chapter 5. Notably, the multi-domain skeletal muscle model integrates a well-established (microscopic) description of the muscle fibre membrane's electrophysiology [e.g., 2, 27, 121, 237] and the most relevant structural as well as functional features of skeletal muscle tissue into a multiphase macroscopic continuum model. The proposed model can be described as a skeletal muscle-specific bidomain-like model [cf. e.g., 37, 110] and is expected to have strong predictive capabilities. To simulate muscle-induced bioelectromagnetic fields in the whole body, the multi-domain skeletal muscle model can be coupled to a volume conductor model, i.e., representing electrically inactive tissues surrounding the muscle, for example, fat, connective tissues or the skin. Further, the modelling framework allows the computation of the muscle-induced magnetic field. As no analytical solution exists for the described mathematical model, a numerical discretisation scheme for approximating the proposed model equations was developed, see Chapter 6. The resulting computational model was validated by performing a set of convergence studies.

Using muscle-induced bioelectromagnetic fields within biomedical applications requires a solid understanding of the relation between the biophysical processes in the body and the spatiotemporal patterns of the measurable signals. This work presents the first detailed comparison of compound muscle electric potentials and compound muscle magnetic fields, see Chapter 7. That is, the EMG or MMG signal generated by the synchronous activity of multiple muscle fibres. Thus, the results presented are comparable to EMG or MMG of electrically or reflex-evoked contractions [e.g., 15]. EMG or MMG of artificially evoked contractions is more straightforward to interpret than signals stemming from voluntary contractions. Nevertheless, it is impossible to control all system parameters experimentally. In contrast, the simulation framework allows the investigation of each relevant factor. This work simulated muscle-induced bioelectromagnetic fields for idealised cube-shaped fusiform skeletal muscles, where the influence of complex muscle architectures can be neglected [cf. e.g., 19, 177]. It is shown that EMG

and MMG signals depend on the number of active muscle fibres, the depth of the active fibres, the properties of the recruited muscle fibres, the electric properties of the tissues, and the spatial configuration of the detection system. These factors are typically unknown for *in vivo* studies. Thus, studies correlating surface EMG signals and the biophysical state of the body are often associated with considerable uncertainty. This work demonstrates that MMG is subject to the same sources of uncertainty. One of surface EMG's most extensively discussed properties is the spatial low-pass filtering effect, depending on the exact properties of the body [e.g., 66, 159, 219]. This effect inherently limits the sparsity and, thus, the spatial selectivity of surface EMG measurements. This work demonstrates that the sparsity of MMG signals is less sensitive to changes in the body's properties or anatomy. The increased spatial selectivity can decrease the influence of amplitude cancellation when recording interference signals [e.g., 67], potentially reduces the effect of cross-talk from nearby muscles [e.g., 71, 240, 248] and might lead to more accurate results of source localisation methods [97]. Further, the computational model allows us to examine the relevance of different currents for explaining a measurable MMG signal. The simulations predict that both MMG components orthogonal to the muscle fibres strongly reflect intracellular currents. Further, it is noted that the model predicts an unexpectedly large contribution of currents in the non-recruited muscle fibres to the overall magnetic field. Intracellular currents can not be detected with EMG. Whether this provides any advantage for biomedical applications needs to be studied in the future.

EMG measurements are routinely used to decode the neural control signals to the muscle, for example, for studying motor control [e.g., 63, 69, 70] or for driving human-machine interfaces [e.g., 73, 78, 90, 123, 258]. However, no univocal relation between the EMG's signal amplitude and the muscle force exists [e.g., 56, 67, 83]. Hence, the current gold standard for reconstructing the voluntary drive to a muscle is the decomposition of EMG signals into the spike trains of individual motor units [e.g., 51, 63, 124, 194]. However, (non-invasive) surface EMG-based motor unit decomposition is limited to detecting only a small subpopulation of motor units from a whole motor unit pool. Better results can only be achieved by using invasive high-density needle electrodes [e.g., 186, 187]. This is caused by the body's spatial-low pass filtering effect, which increases the similarity between different motor unit electric potentials such that they often become indistinguishable [75]. Chapter 8 compares the use of MMG and EMG for decoding voluntary contractions It is shown that EMG and MMG of voluntary contractions can be described by the same generative model [cf. 44]. Accordingly, both signals exhibit positive as well as destructive interference. Hence, as for EMG, there is no univocal relation between the amplitude of the MMG signal and the neural drive to the muscle. This work compares MMG- and EMG-based motor unit decompositions by using a novel *in silico* trial framework. The *in silico* trials integrate the presented computational skeletal muscle model into the workflow of blind source separation-based motor unit decomposition algorithms [e.g., 30, 125, 194]. It is shown that non-invasive high-density MMG-based motor unit decomposition is superior to high-density surface EMG-based motor unit decomposition. The fraction of motor units that can be robustly decomposed nearly increases by a factor of two. Notably, decomposing non-invasively measured MMG data also allows the detection of rather deep motor units. This is not possible when decomposing high-density surface EMG [82, 220]. Further, the most important feature explaining the MMG's superior separability is that a three-dimensional vector field is considered.

9.2 Discussion

9.2.1 Validation and Limitations

A direct validation of the proposed simulation framework is currently out of scope due to methodological limitations. However, as the proposed model consistently integrates a validated microscopic electric circuit model of the muscle fibre membranes [2, 27, 121, 237], i.e., the source of EMG and MMG, into a macroscopic continuum model respecting Maxwell's equations, it is emphasised that the proposed multiscale model provides strong predictive capabilities. This is underlined by various experimental observations correctly predicted by the presented simulation framework. For example, the muscle fibre conduction velocities predicted by the computational model are perfectly in the range of experimental observations, i.e., approximately $2.5\,\mathrm{m\,s^{-1}}$ to $5\,\mathrm{m\,s^{-1}}$ [5]. Further, the EMG signals predicted by the multi-domain model replicate the key features of (experimentally acquired) EMG data, for example, regarding the signal shape [147, 177], the amplitude decay [82], the effect of fat tissue [9, 219], the signal's frequency content [46] as well as the interference patterns observed during voluntary contractions [44, 45, 67, 70]. Comparable data has yet to be recorded for MMG. Nevertheless, the presented *in silico* predictions are qualitatively in agreement with existing experimental measurements. First, the model respects the observation that the compound muscle responses recorded via EMG and MMG have the same temporal duration and show similar frequency content [38, 207, 271]. Further, the bi-phasic shape of the magnetic field generated by the active muscle fibres is in agreement with the measurement of the magnetic field induced by an isolated muscle fibre [cf. 256] or an isolated axon [e.g., 225]. Yet, experimentally measured compound muscle magnetic fields show variable multi-phasic shapes [e.g., 19, 20]. This agrees with the simulated MMG signals. Multi-phase shapes are caused by volume currents in the extracellular space or end-of-fibre effects. However, as volume currents strongly depend on the exact tissue geometry and the electric tissue properties, a direct comparison to existing experimental data is impossible. Nevertheless, it should be noted that the presented continuum modelling approach allows high flexibility to resolve arbitrary muscle geometries when employing discretisation schemes such as the finite element method [e.g., 269]. Moreover, this work focused on the physical properties of muscle-induced bioelectromagnetic fields. Hence, idealised sensors are considered, i.e., having the ability to record the physical fields from a single point in space, the capability to sample the full bandwidth of the physical fields and the measurements are not affected by noise. However, for comparing *in silico* predictions with experimental data, the properties of the EMG electrodes or MMG sensors need to be considered.

9.2.2 Contextualisation of the Proposed Simulation Framework

Mathematical models have been an essential tool to describe the behaviour of excitable tissues [e.g., 110, 214, 221] or cells [e.g., 116, 121, 200] and for assisting the interpretation of bioelectromagnetic fields [e.g., 138, 163, 212]. For example, volume conductor models, cf. Section 4.2.1, are commonly used for EEG-based or MEG-based neuro-imaging techniques [e.g., 98, 204, 228, 257] and for the simulation of EMG signals [e.g., 179, 242]. Further, the bidomain model, cf. Section 4.2.2, has provided essential insights into the properties of the electric signals generated by the heart as well as the biophysics of defibrillations [e.g., 37, 110, 253]. The most relevant difference between volume conductor models and the bidomain model is their capabilities to explain the generation of a bioelectromagnetic field mechanistically. Volume conductor models are appropriate when the fundamental properties of the (relevant) bioelectric sources are known and can be described independently from the body's electric potential field. Therefore, volume conductor models typically use phenomenological descriptions of the bioelec-

tric sources. The origin of the magnetic field generated by a skeletal muscle has yet to be fully explored. Hence, this work introduced a novel multiscale simulation framework that can mechanistically link the function and structure of the tissue to the observed bioelectromagnetic fields.

The class of bidomain-like models [e.g., 23, 42, 182, 221, 246, 254] represents the most prominent example of tissue-scale models that directly link the propagation of electric signals in the body to the biophysical function of a tissue. Therefore, the cell membrane dynamics and the tissue's most relevant microstructural features are integrated into a multiphase macroscopic continuum model. However, none of the existing bidomain-like models can adequately resolve the electrophysiological behaviour of skeletal muscle tissue. Most importantly, bidomain-like models fail to adequately resolve a skeletal muscle's functional organisation in motor units. Hence, this work introduces a skeletal muscle-specific extension of the bidomain model, cf. Chapter 5. For deriving the multi-domain equations, it is assumed that at each material point, the behaviour of each intracellular domain can be modelled by considering the microscale interaction between one representative muscle fibre for each motor unit and the surrounding extracellular space. Further, the consistency of the macroscopic charge balance is guaranteed by introducing a mesoscale motor unit density parameter, i.e., resolving the local motor unit composition of the tissue. Notably, a multi-domain model can also be obtained by homogenising the behaviour of multiple cells [cf. 23, 42]. This would require formulating the intracellular current balance equations considering the overall membrane surface area of all cells associated with an intracellular domain. In the classical bidomain model, a representative control volume can be reduced to a single cell interacting with the extracellular space. Hence, both modelling assumptions will yield the same results. However, the two assumptions for a multi-domain approach will result in different biophysical tissue properties. While the conduction velocity of action potentials for the presented multi-domain model of skeletal muscle tissue is strongly associated with the shape and the function of a single cell, for the alternative approach, the propagation of electric signals in the tissue reflects an ensemble property of multiple cells.

Computing the solution of the microscopic membrane models at each discretisation point is associated with significant computational demands. Hence, using bidomain-type models typically requires the development of efficient numerical methods as well as the use of large-scale computational facilities [e.g., 16, 80, 94, 145, 162]. Thus, when the properties of the electric sources can be described with sufficient precision a priori, a volume conductor model provides a better trade-off between the computational cost and the accuracy of the simulations. Finally, it is noted that the presented model considers isometric conditions. However, muscle contraction is associated with large deformations. EMG and MMG signals during motions can be simulated by coupling the proposed bioelectromagnetic skeletal muscle model to a continuum-mechanical skeletal muscle model [cf. e.g., 104, 105, 185, 221, 230, 234].

9.2.3 Future Directions and Biomedical Applications

The results presented within this work consider an idealised cube-shaped, fusiform skeletal muscle. However, both EMG and MMG signals strongly depend on the geometry of the muscle itself as well as the surrounding tissues [19, 177]. To investigate muscle geometry's influence on muscle-induced bioelectromagnetic fields, the *in silico* experiments performed within this work should be applied to other muscle architectures. Thereby, it is noted that recording high-density EMG allows the extraction of morphological features [177], for example, the innervation zone or the muscle fibre direction in pinnated muscles. Such anatomical markers can also be extracted from MMG signals [e.g., 19]. However, such methods only provide a rough view of a muscle's (superficial) structure. More detailed insights into the structure of

skeletal muscles could be obtained by developing physiological imaging techniques based on muscle-induced bioelectromagnetic fields, i.e., simulating the bioelectric source field explaining a measured EMG or MMG signal. While inverse modelling is commonly used for localising the neural activity in the brain [e.g., 98, 204, 228, 257], only a few studies have applied such techniques to EMG signals [152, 180, 255] or only recently MMG signals [154]. Such electrophysiological tomograms of skeletal muscles could, for example, provide insights on the (spatial) recruitment strategies of muscles [111], the morphology of individual motor units [28, 113, 241], the anatomical position of the innervation zones [153] and could ultimately be used to track the internal deformation of the tissue. Electrophysiological images of skeletal muscles rarely exist because surface EMG-based inverse modelling typically yields inaccurate results due to the unknown conductive properties of the tissue. For example, for the brain, it was shown that magnetic field-based source reconstruction provides higher accuracy than the electric potential field-based counterpart [97]. Hence, advancing MMG might be a critical step towards novel *in vivo* imaging techniques of skeletal muscles. The presented modelling framework can be used to generate labelled test data for optimising and validating methods that aim to reconstruct the bioelectric sources in skeletal muscles.

This work showed that non-invasive high-density MMG-based motor unit decomposition is superior to high-density surface EMG-based motor unit decompositions, cf. Section 8.4. It was concluded that representing a three-dimensional vector field is the most critical feature of the MMG for explaining its outstanding separability. Nevertheless, the factors influencing the performance of motor unit decompositions require further investigation. The latter can be achieved by utilising the presented *in silico* trial framework, cf. Section 8.4.1, for example, regarding the influence of the synchronisation of the motor neuron firings, the size of the motor unit pool, the muscle properties as well as the muscle geometry. Further, for the detection system, it is essential to investigate the geometrical arrangement of the sensors as well as the influence of noise. While it was shown that the number of motor units that can be observed is higher when decomposing MMG instead of EMG, another significant limitation of state-of-the-art motor unit decomposition techniques is that they are typically limited to isometric contractions. Only a few exceptions consider cyclic contractions [e.g., 48, 89], whereby the signal can be easily windowed into quasi-isometric segments. The fact that MMG can be used as a physiological imaging technique might open up new possibilities for decomposing MMG signals during arbitrary motions. In particular, one can use simulations to predict the motor unit responses for arbitrary joint positions. Further, a fundamental challenge of *in vivo* motor unit decomposition is the development of proper validation methods. One approach is to simultaneously perform needle EMG recordings as well as surface EMG measurements and compare the similarity between the spike trains of commonly identified motor units [e.g., 47, 124, 194]. The fact that the MMG measures a three-dimensional vector field might enable completely non-invasive validation methods, for example, comparing the similarity of spike trains identified from different MMG components.

This work focused on EMG and MMG signals generated by the healthy neuromuscular system. The potential use of MMG in clinical applications, for example, as a non-invasive diagnostic tool replacing needle EMG measurements [cf. e.g., 164], needs to be explored in the future. The results show that – as for EMG – MMG is the linear superposition of the signals generated by the individual motor units. This is the basis for using electrically evoked contractions and surface EMG to perform motor unit number estimation (MUNE) [e.g., 29]. The number of motor units is a critical biomarker to quantify the progression of neuromuscular diseases. The equivalence regarding the signal summation of EMG and MMG

means that MMG-based MUNE is possible. Because MMG is less biased in recording signals from superficial motor units, MMG-based MUNE might be superior to EMG-based MUNE. This needs to be investigated in the future. Further, the fact that the proposed multiscale model links the function and structure of a skeletal muscle to the measurable bioelectromagnetic fields allows us to predict EMG or MMG signals for various neuromuscular pathologies. For example, diverse types of myotonic discharges can be simulated by implementing the corresponding ion channel defects in the microscopic membrane model [cf. e.g., 27, 61].

The results presented in this thesis focused on the physical properties of muscle-induced bioelectromagnetic fields. In an experimental environment, measurements are affected by different sources of physiological noise (e.g., cross-talk from other muscles or signals stemming from other organs such as the heart) and non-physiological noise (e.g., electromagnetic noise from the environment or imperfections of the observation system). When conducting high-density EMG or MMG measurements, noise can be suppressed by performing spatial filtering [e.g., 177]. That is, computing the linear combination of the signals recorded at different sampling points. This can be considered an approximation for the spatial derivatives of the measured physical field. Further, spatial filtering can be used to focus on specific sources, i.e., increasing the spatial sensitivity of a measurement [e.g., 75]. Hence, in the future, the fundamentals and advantages of spatial filters applied to high-density MMG need to be explored [268].

9.3 Conclusion

This work has developed methods that enable systematic *in silico* investigations of muscle-induced bioelectromagnetic fields, i.e., EMG and MMG. Both signals stem from the same biophysical phenomenon, namely the muscle fibre action potentials, and can be used to study the neuromuscular system *in vivo*. Currently, only EMG is routinely used as a clinical diagnostic tool and in various research applications. The advantages and limitations of EMG recordings are extensively described in the scientific literature. In contrast, MMG is an emerging technology with great potential to provide (novel) insights into the function of the neuromuscular system. To pave the way towards using MMG in biomedical applications, this work presents the first systematic comparison between EMG and MMG. It is shown that EMG and MMG are complementary signals that share various common characteristics, for example, regarding the duration of the signals and the spatiotemporal signal summation. Yet, it is shown that the sparsity of non-invasive MMG is less affected by the properties and anatomy of the body than surface EMG. Further, this work demonstrates that MMG recordings can push the boundaries of non-invasive motor unit decomposition. The MMG methodology is expected to be widely available within the next ten years. To unlock the full potential of MMG, experimental work and theoretical studies must be carefully combined.

Bibliography

[1] Adrian, E. D. & Bronk, D. W.: The discharge of impulses in motor nerve fibres: Part I. impulses in single fibres of the phrenic nerve. *The Journal of physiology* **66** (1928), 81.

[2] Adrian, R. H.; Chandler, W. K. & Hodgkin, A. L.: Voltage clamp experiments in striated muscle fibres. *The Journal of Physiology* **208** (1970), 607–644.

[3] Aidley, D. J.: *The physiology of excitable cells*. Cambridge University Press 1998.

[4] Anderson, F. C. & Pandy, M. G.: Dynamic optimization of human walking. *J. Biomech. Eng.* **123** (2001), 381–390.

[5] Andreassen, S. & Arendt-Nielsen, L.: Muscle fibre conduction velocity in motor units of the human anterior tibial muscle: a new size principle parameter. *The Journal of Physiology* **391** (1987), 561–571.

[6] Andreassen, S. & Rosenfalck, A.: Relationship of intracellular and extracellular action potentials of skeletal muscle fibers. *Critical reviews in bioengineering* **6** (1981), 267–306.

[7] Arfken, G. B.; Weber, H. J. & Harris, F. E.: Chapter 10-green's functions. *Mathematical methods for physicists* (2013), 447–467.

[8] Armstrong, C. M. & Hille, B.: Voltage-gated ion channels and electrical excitability. *Neuron* **20** (1998), 371–380.

[9] Barkhaus, P. E. & Nandedkar, S. D.: Recording characteristics of the surface EMG electrodes. *Muscle & Nerve: Official Journal of the American Association of Electrodiagnostic Medicine* **17** (1994), 1317–1323.

[10] Blijham, P. J.; Ter Laak, H. J.; Schelhaas, H. J.; Van Engelen, B.; Stegeman, D. F. & Zwarts, M. J.: Relation between muscle fiber conduction velocity and fiber size in neuromuscular disorders. *Journal of Applied Physiology* **100** (2006), 1837–1841.

[11] Blok, J.; Van Dijk, J.; Drost, G.; Zwarts, M. & Stegeman, D.: A high-density multichannel surface electromyography system for the characterization of single motor units. *Review of scientific instruments* **73** (2002), 1887–1897.

[12] Bodine-Fowler, S.; Garfinkel, A.; Roy, R. R. & Edgerton, V. R.: Spatial distribution of muscle fibers within the territory of a motor unit. *Muscle & Nerve: Official Journal of the American Association of Electrodiagnostic Medicine* **13** (1990), 1133–1145.

[13] Booth, V.; Rinzel, J. & Kiehn, O.: Compartmental model of vertebrate motoneurons for Ca^{2+}-dependent spiking and plateau potentials under pharmacological treatment. *Journal of Neurophysiology* **78** (1997), 3371–3385.

[14] Boto, E.; Meyer, S. S.; Shah, V.; Alem, O.; Knappe, S.; Kruger, P.; Fromhold, T. M.; Lim, M.; Glover, P. M.; Morris, P. G. et al.: A new generation of magnetoencephalography: Room temperature measurements using optically-pumped magnetometers. *NeuroImage* **149** (2017), 404–414.

[15] Botter, A. & Merletti, R.: *EMG of Electrically Stimulated Muscles*, John Wiley & Sons, Ltd 2016, chap. 11. ISBN 9781119082934, pp. 311–332.

[16] Bradley, C. P.; Emamy, N.; Ertl, T.; Göddeke, D.; Hessenthaler, A.; Klotz, T.; Krämer, A.; Krone, M.; Maier, B.; Mehl, M.; Rau, T. & Röhrle, O.: Enabling detailed, biophysics-based skeletal muscle models on HPC systems. *Frontiers in Physiology* **9** (2018), 816, ISSN 1664-042X.

[17] Broman, H.; Bilotto, G. & De Luca, C. J.: A note on the noninvasive estimation of muscle fiber conduction velocity. *IEEE transactions on biomedical engineering* (1985), 341–344.

[18] Broser, P. J.; Knappe, S.; Kajal, D.-S.; Noury, N.; Alem, O.; Shah, V. & Braun, C.: Optically pumped magnetometers for magneto-myography to study the innervation of the hand. *IEEE Transactions on Neural Systems and Rehabilitation Engineering* **26** (2018), 2226–2230.

[19] Broser, P. J.; Marquetand, J.; Middelmann, T.; Sometti, D. & Braun, C.: Investigation of the temporal and spatial dynamics of muscular action potentials through optically pumped magnetometers. *Journal of Electromyography and Kinesiology* **59** (2021), 102571.

[20] Broser, P. J.; Middelmann, T.; Sometti, D. & Braun, C.: Optically pumped magnetometers disclose magnetic field components of the muscular action potential. *Journal of Electromyography and Kinesiology* **56** (2021), 102490.

[21] Bryant, S. H.: Cable properties of external intercostal muscle fibres from myotonic and nonmyotonic goats. *The Journal of Physiology* **204** (1969), 539 – 550.

[22] Buchthal, F.; Erminio, F. & Rosenfalck, P.: Motor unit territory in different human muscles. *Acta Physiologica Scandinavica* **45** (1959), 72–87.

[23] Buist, M. L. & Poh, Y. C.: An extended bidomain framework incorporating multiple cell types. *Biophysical Journal* **99** (2010), 13 – 18, ISSN 0006-3495.

[24] Burke, R.: Motor units: anatomy, physiology, and functional organization. *Comprehensive Physiology* (2011), 345–422.

[25] Burke, R. & Tsairis, P.: Anatomy and innervation ratios in motor units of cat gastrocnemius. *The Journal of physiology* **234** (1973), 749–765.

[26] Campanini, I.; Disselhorst-Klug, C.; Rymer, W. Z. & Merletti, R.: Surface EMG in clinical assessment and neurorehabilitation: barriers limiting its use. *Frontiers in Neurology* (2020), 934.

[27] Cannon, S.; Brown, R. & Corey, D.: Theoretical reconstruction of myotonia and paralysis caused by incomplete inactivation of sodium channels. *Biophysical Journal* **65** (1993), 270–288.

[28] Carbonaro, M.; Meiburger, K. M.; Seoni, S.; Hodson-Tole, E. F.; Vieira, T. & Botter, A.: Physical and electrophysiological motor unit characteristics are revealed with simultaneous high-density electromyography and ultrafast ultrasound imaging. *Scientific Reports* **12** (2022), 1–14.

[29] de Carvalho, M.; Barkhaus, P. E.; Nandedkar, S. D. & Swash, M.: Motor unit number estimation (MUNE): Where are we now? *Clinical Neurophysiology* **129** (2018), 1507–1516.

[30] Chen, M. & Zhou, P.: A novel framework based on FastICA for high density surface EMG decomposition. *IEEE Transactions on Neural Systems and Rehabilitation Engineering* **24** (2015), 117–127.

[31] Cheng, L. K.; Sands, G. B.; French, R.; Withy, S.; Wong, S.; Legget, M.; Smith, W. & Pullan, A. J.: Rapid construction of a patient-specific torso model from 3D ultrasound for non-invasive imaging of cardiac electrophysiology. *Medical and Biological Engineering and Computing* **43** (2005), 325–330.

[32] Cisi, R. R. & Kohn, A. F.: Simulation system of spinal cord motor nuclei and associated nerves and muscles, in a web-based architecture. *Journal of Computational Neuroscience* **25** (2008), 520–542.

[33] Clamann, H. P.: Statistical analysis of motor unit firing patterns in a human skeletal muscle. *Biophysical journal* **9** (1969), 1233–1251.

[34] Clamann, H. P.: Activity of single motor units during isometric tension. *Neurology* **20** (1970), 254–254.

[35] Clarke, J.; Lee, Y.-H. & Schneiderman, J.: Focus on SQUIDs in biomagnetism. *Supercond. Sci. Technol* **31** (2018), 080201.

[36] Claydon, F.; Pilkington, T.; Tang, A.; Morrow, M. & Ideker, R.: A volume conductor model of the thorax for the study of defibrillation fields. *IEEE transactions on biomedical engineering* **35** (1988), 981–992.

[37] Clayton, R.; Bernus, O.; Cherry, E.; Dierckx, H.; Fenton, F. H.; Mirabella, L.; Panfilov, A. V.; Sachse, F. B.; Seemann, G. & Zhang, H.: Models of cardiac tissue electrophysiology: progress, challenges and open questions. *Progress in biophysics and molecular biology* **104** (2011), 22–48.

[38] Cohen, D. & Givler, E.: Magnetomyography: Magnetic fields around the human body produced by skeletal muscles. *Applied Physics Letters* **21** (1972), 114–116.

[39] Cole, K. S. & Curtis, H. J.: Electric impedance of the squid giant axon during activity. *The Journal of general physiology* **22** (1939), 649–670.

[40] Colquhoun, D. & Sakmann, B.: From muscle endplate to brain synapses: a short history of synapses and agonist-activated ion channels. *Neuron* **20** (1998), 381–387.

[41] Coombs, J. S.; Eccles, J. C. & Fatt, P.: Excitatory synaptic action in motoneurones. *The Journal of physiology* **130** (1955), 374.

[42] Corrias, A.; Pathmanathan, P.; Gavaghan, D. J. & Buist, M. L.: Modelling tissue electrophysiology with multiple cell types: applications of the extended bidomain framework. *Integrative Biology* **4** (2012), 192–201.

[43] Daube, J. R. & Rubin, D. I.: Needle electromyography. *Muscle & Nerve: Official Journal of the American Association of Electrodiagnostic Medicine* **39** (2009), 244–270.

[44] Day, S. J. & Hulliger, M.: Experimental simulation of cat electromyogram: evidence for algebraic summation of motor-unit action-potential trains. *Journal of Neurophysiology* **86** (2001), 2144–2158.

[45] De Luca, C. J.: The use of surface electromyography in biomechanics. *Journal of applied biomechanics* **13** (1997), 135–163.

[46] De Luca, C. J.: Surface electromyography: Detection and recording. *DelSys Incorporated* **10** (2002), 1–10.

[47] De Luca, C. J.; Adam, A.; Wotiz, R.; Gilmore, L. D. & Nawab, S. H.: Decomposition of surface EMG signals. *Journal of neurophysiology* **96** (2006), 1646–1657.

[48] De Luca, C. J.; Chang, S.-S.; Roy, S. H.; Kline, J. C. & Nawab, S. H.: Decomposition of surface EMG signals from cyclic dynamic contractions. *Journal of neurophysiology* **113** (2015), 1941–1951.

[49] De Luca, C. J. & Erim, Z.: Common drive of motor units in regulation of muscle force. *Trends in neurosciences* **17** (1994), 299–305.

[50] De Luca, C. J. & Forrest, W. J.: An electrode for recording single motor unit activity during strong muscle contractions. *IEEE Transactions on Biomedical Engineering* (1972), 367–372.

[51] Del Vecchio, A. & Farina, D.: Interfacing the neural output of the spinal cord: robust and reliable longitudinal identification of motor neurons in humans. *Journal of neural engineering* **17** (2019), 016003.

[52] Del Vecchio, A.; Holobar, A.; Falla, D.; Felici, F.; Enoka, R. & Farina, D.: Tutorial: Analysis of motor unit discharge characteristics from high-density surface EMG signals. *Journal of Electromyography and Kinesiology* **53** (2020), 102426.

[53] Del Vecchio, A.; Negro, F.; Felici, F. & Farina, D.: Distribution of muscle fibre conduction velocity for representative samples of motor units in the full recruitment range of the tibialis anterior muscle. *Acta Physiologica* **222** (2017), e12930.

[54] Delp, S. L.; Anderson, F. C.; Arnold, A. S.; Loan, P.; Habib, A.; John, C. T.; Guendelman, E. & Thelen, D. G.: OpenSim: open-source software to create and analyze dynamic simulations of movement. *IEEE transactions on biomedical engineering* **54** (2007), 1940–1950.

[55] Di Francesco, D. & Noble, D.: A model of cardiac electrical activity incorporating ionic pumps and concentration changes. *Philosophical Transactions of the Royal Society of London. B, Biological Sciences* **307** (1985), 353–398.

[56] Dideriksen, J. L.; Enoka, R. M. & Farina, D.: Neuromuscular adjustments that constrain submaximal EMG amplitude at task failure of sustained isometric contractions. *Journal of Applied Physiology* **111** (2011), 485–494.

[57] Dimitrova, N. & Dimitrov, G.: Interpretation of EMG changes with fatigue: facts, pitfalls, and fallacies. *Journal of Electromyography and Kinesiology* **13** (2003), 13–36.

[58] Dimitrova, N. A.; Dimitrov, A. G. & Dimitrov, G. V.: Calculation of extracellular potentials produced by an inclined muscle fibre at a rectangular plate electrode. *Medical Engineering & Physics* **21** (1999), 583–588.

[59] Duchateau, J. & Enoka, R. M.: Human motor unit recordings: origins and insight into the integrated motor system. *Brain research* **1409** (2011), 42–61.

[60] Eccles, J. C.: *The physiology of synapses*. Academic Press 2013.

[61] Elia, N.; Nault, T.; McMillan, H. J.; Graham, G. E.; Huang, L. & Cannon, S. C.: Myotonic myopathy with secondary joint and skeletal anomalies from the c.2386C>G, p.L796V mutation in SCN4A. *Frontiers in neurology* **11** (2020), 77.

[62] Enoka, R. M.: *Neuromechanics of human movement*. Human kinetics 2008.

[63] Enoka, R. M.: Physiological validation of the decomposition of surface EMG signals. *Journal of Electromyography and Kinesiology* **46** (2019), 70–83.

[64] Enoka, R. M. & Fuglevand, A. J.: Motor unit physiology: some unresolved issues. *Muscle & Nerve: Official Journal of the American Association of Electrodiagnostic Medicine* **24** (2001), 4–17.

[65] Epstein, B. R. & Foster, K. R.: Anisotropy in the dielectric properties of skeletal muscle. *Medical and Biological Engineering and Computing* **21** (1983), 51, ISSN 1741-0444.

[66] Farina, D.; Cescon, C. & Merletti, R.: Influence of anatomical, physical, and detection-system parameters on surface EMG. *Biological cybernetics* **86** (2002), 445–456.

[67] Farina, D.; Cescon, C.; Negro, F. & Enoka, R. M.: Amplitude cancellation of motor-unit action potentials in the surface electromyogram can be estimated with spike-triggered averaging. *Journal of neurophysiology* **100** (2008), 431–440.

[68] Farina, D. & Merletti, R.: A novel approach for precise simulation of the EMG signal detected by surface electrodes. *IEEE Transactions on Biomedical Engineering* **48** (2001), 637–646.

[69] Farina, D.; Merletti, R. & Enoka, R. M.: The extraction of neural strategies from the surface EMG. *Journal of applied physiology* **96** (2004), 1486–1495.

[70] Farina, D.; Merletti, R. & Enoka, R. M.: The extraction of neural strategies from the surface EMG: an update. *Journal of Applied Physiology* **117** (2014), 1215–1230.

[71] Farina, D.; Merletti, R.; Indino, B. & Graven-Nielsen, T.: Surface EMG crosstalk evaluated from experimental recordings and simulated signals. *Methods of information in medicine* **43** (2004), 30–35.

[72] Farina, D.; Mesin, L. & Martina, S.: Advances in surface electromyographic signal simulation with analytical and numerical descriptions of the volume conductor. *Medical & Biological Engineering & Computing* **42** (2004), 467–476.

[73] Farina, D. & Negro, F.: Accessing the neural drive to muscle and translation to neurorehabilitation technologies. *IEEE Reviews in biomedical engineering* **5** (2012), 3–14.

[74] Farina, D. & Negro, F.: Common synaptic input to motor neurons, motor unit synchronization, and force control. *Exercise and sport sciences reviews* **43** (2015), 23–33.

[75] Farina, D.; Negro, F.; Gazzoni, M. & Enoka, R. M.: Detecting the unique representation of motor-unit action potentials in the surface electromyogram. *Journal of neurophysiology* **100** (2008), 1223–1233.

[76] Farina, D.; Stegeman, D. F. & Merletti, R.: *Biophysics of the Generation of EMG Signals*, John Wiley & Sons, Ltd 2016, chap. 2. pp. 1–24.

[77] Fenici, R.; Brisinda, D. & Meloni, A. M.: Clinical application of magnetocardiography. *Expert review of molecular diagnostics* **5** (2005), 291–313.

[78] Ferreira, A.; Celeste, W. C.; Cheein, F. A.; Bastos-Filho, T. F.; Sarcinelli-Filho, M. & Carelli, R.: Human-machine interfaces based on EMG and EEG applied to robotic systems. *Journal of NeuroEngineering and Rehabilitation* **5** (2008), 1–15.

[79] Forgy, E. W.: Cluster analysis of multivariate data: efficiency versus interpretability of classifications. *biometrics* **21** (1965), 768–769.

[80] Franzone, P. C.; Pavarino, L. F. & Scacchi, S.: Parallel multilevel solvers for the cardiac electro-mechanical coupling. *Applied Numerical Mathematics* **95** (2015), 140–153.

[81] Fuglevand, A. J.; Winter, D. A. & Patla, A. E.: Models of recruitment and rate coding organization in motor unit pools. *Journal of Neurophysiology* **70** (1993), 2470–2488.

[82] Fuglevand, A. J.; Winter, D. A.; Patla, A. E. & Stashuk, D.: Detection of motor unit action potentials with surface electrodes: influence of electrode size and spacing. *Biological cybernetics* **67** (1992), 143–153.

[83] Fuglsang-Frederiksen, A.: The utility of interference pattern analysis. *Muscle & Nerve: Official Journal of the American Association of Electrodiagnostic Medicine* **23** (2000), 18–36.

[84] Gabriel, S.; Lau, R. W. & Gabriel, C.: The dielectric properties of biological tissues: II. measurements in the frequency range 10 hz to 20 ghz. *Physics in Medicine & Biology* **41** (1996), 2251.

[85] Gadsby, D. C.: Ion channels versus ion pumps: the principal difference, in principle. *Nature reviews Molecular cell biology* **10** (2009), 344–352.

[86] Ganapathy, N.; Clark Jr, J. & Wilson, O.: Extracellular potentials from skeletal muscle. *Mathematical biosciences* **83** (1987), 61–96.

[87] Gielen, F. L. H.; Wallinga-de Jonge, W. & Boon, K. L.: Electrical conductivity of skeletal muscle tissue: Experimental results from different muscles in vivo. *Medical and Biological Engineering and Computing* **22** (1984), 569–577, ISSN 1741-0444, URL `https://doi.org/10.1007/BF02443872`.

[88] Glancy, B.; Hartnell, L. M.; Malide, D.; Yu, Z.-X.; Combs, C. A.; Connelly, P. S.; Subramaniam, S. & Balaban, R. S.: Mitochondrial reticulum for cellular energy distribution in muscle. *Nature* **523** (2015), 617–620.

[89] Glaser, V. & Holobar, A.: Motor unit identification from high-density surface electromyograms in repeated dynamic muscle contractions. *IEEE Transactions on Neural Systems and Rehabilitation Engineering* **27** (2018), 66–75.

[90] Gomez-Gil, J.; San-Jose-Gonzalez, I.; Nicolas-Alonso, L. F. & Alonso-Garcia, S.: Steering a tractor by means of an EMG-based human-machine interface. *Sensors* **11** (2011), 7110–7126.

[91] Gordon, A. M.; Homsher, E. & Regnier, M.: Regulation of contraction in striated muscle. *Physiological reviews* **80** (2000), 853–924.

[92] Gordon, A. M.; Huxley, A. F. & Julian, F. J.: The variation in isometric tension with sarcomere length in vertebrate muscle fibres. *The Journal of Physiology* **184** (1966), 170–192.

[93] Griffiths, D. J.: *Introduction to electrodynamics; 4th ed.* Pearson, Boston, MA 2013.

[94] Gurev, V.; Pathmanathan, P.; Fattebert, J.-L.; Wen, H.-F.; Magerlein, J.; Gray, R. A.; Richards, D. F. & Rice, J. J.: A high-resolution computational model of the deforming human heart. *Biomechanics and modeling in mechanobiology* **14** (2015), 829–849.

[95] Gutteling, T. P.; Bonnefond, M.; Clausner, T.; Daligault, S.; Romain, R.; Mitryukovskiy, S.; Fourcault, W.; Josselin, V.; Le Prado, M.; Palacios-Laloy, A. et al.: A new generation of OPM for high dynamic and large bandwidth MEG: the 4He OPMs — first applications in healthy volunteers. *Sensors* **23** (2023), 2801.

[96] Hakansson, C.: Conduction velocity and amplitude of the action potential as related to circumference in the isolated fibre of frog muscle. *Acta Physiologica Scandinavica* **37** (1956), 14–34.

[97] Hämäläinen, M.; Hari, R.; Ilmoniemi, R. J.; Knuutila, J. & Lounasmaa, O. V.: Magnetoencephalography—theory, instrumentation, and applications to noninvasive studies of the working human brain. *Reviews of modern Physics* **65** (1993), 413.

[98] Hämäläinen, M. S. & Ilmoniemi, R. J.: Interpreting magnetic fields of the brain: minimum norm estimates. *Medical & biological engineering & computing* **32** (1994), 35–42.

[99] Hanson, J. & Huxley, H. E.: Structural basis of the cross-striations in muscle. *Nature* **172** (1953), 530–532.

[100] Heckman, C. J. & Enoka, R. M.: Physiology of the motor neuron and the motor unit. In *Handbook of Clinical Neurophysiology*. Elsevier 2004, vol. 4, pp. 119–147.

[101] Heckman, C. J. & Enoka, R. M.: Motor Unit. *Comprehensive Physiology* **2** (2012), 2629–2682.

[102] Heckmatt, J. Z.; Leeman, S. & Dubowitz, V.: Ultrasound imaging in the diagnosis of muscle disease. *The Journal of pediatrics* **101** (1982), 656–660.

[103] Heidari, H.; Zuo, S.; Krasoulis, A. & Nazarpour, K.: CMOS magnetic sensors for wearable magnetomyography. In *2018 40th Annual International Conference of the IEEE Engineering in Medicine and Biology Society (EMBC)*, IEEE 2018, pp. 2116–2119.

[104] Heidlauf, T.; Klotz, T.; Altan, E.; Bleiler, C.; Siebert, T.; Rode, C. & Röhrle, O.: A multi-scale continuum model of skeletal muscle mechanics predicting force enhancement based on actin-titin interaction. *Biomechanics and Modeling in Mechanobiology* **11** (2016), 1424 – 1437.

[105] Heidlauf, T.; Klotz, T.; Rode, C.; Siebert, T. & Röhrle, O.: A continuum-mechanical skeletal muscle model including actin-titin interaction predicts stable contractions on the descending limb of the force-length relation. *PLoS computational biology* **13** (2017), e1005773.

[106] Heidlauf, T. & Röhrle, O.: Modeling the chemoelectromechanical behavior of skeletal muscle using the parallel open-source software library OpenCMISS. *Computational and Mathematical Methods in Medicine* **2013** (2013), 1–14.

[107] Henneman, E.: Comments on the logical basis of muscle control. *The segmental motor system* (1990), 7–10.

[108] Henneman, E. & Olson, C. B.: Relations between structure and function in the design of skeletal muscles. *Journal of neurophysiology* **28** (1965), 581–598.

[109] Henneman, E.; Somjen, G. & Carpenter, D. O.: Functional significance of cell size in spinal motoneurons. *Journal of neurophysiology* **28** (1965), 560–580.

[110] Henriquez, C. S.: Simulating the electrical behavior of cardiac tissue using the bidomain model. *Critical reviews in biomedical engineering* **21** (1993), 1–77.

[111] Herring, S. W.; Grimm, A. F. & Grimm, B. R.: Functional heterogeneity in a multipinnate muscle. *American Journal of Anatomy* **154** (1979), 563–575.

[112] Herzog, W.: The multiple roles of titin in muscle contraction and force production. *Biophysical reviews* (2018), 1–13.

[113] Heskamp, L.; Miller, A. R.; Birkbeck, M. G.; Hall, J.; Schofield, I. S.; Blamire, A. M. & Whittaker, R. G.: In vivo 3D imaging of human motor units in upper and lower limb muscles. *Clinical Neurophysiology* (2022).

[114] Hill, A. V.: The heat of shortening and the dynamic constants of muscle. *Proceedings of the Royal Society of London B* **126** (1938), 136–195.

[115] Hille, B.: Ionic channels in excitable membranes. current problems and biophysical approaches. *Biophysical Journal* **22** (1978), 283–294.

[116] Hines, M. L. & Carnevale, N. T.: Neuron: a tool for neuroscientists. *The neuroscientist* **7** (2001), 123–135.

[117] Hodgkin, A. L. & Huxley, A. F.: Action potentials recorded from inside a nerve fibre. *Nature* **144** (1939), 710–711.

[118] Hodgkin, A. L. & Huxley, A. F.: The components of membrane conductance in the giant axon of loligo. *The Journal of physiology* **116** (1952), 473.

[119] Hodgkin, A. L. & Huxley, A. F.: Currents carried by sodium and potassium ions through the membrane of the giant axon of loligo. *The Journal of physiology* **116** (1952), 449.

[120] Hodgkin, A. L. & Huxley, A. F.: The dual effect of membrane potential on sodium conductance in the giant axon of loligo. *The Journal of physiology* **116** (1952), 497.

[121] Hodgkin, A. L. & Huxley, A. F.: A quantitative description of membrane current and its application to conduction and excitation in nerve. *The Journal of Physiology* **117** (1952), 500–544.

[122] Hodgkin, A. L.; Huxley, A. F. & Katz, B.: Measurement of current-voltage relations in the membrane of the giant axon of loligo. *The Journal of physiology* **116** (1952), 424.

[123] Holobar, A. & Farina, D.: Noninvasive neural interfacing with wearable muscle sensors: combining convolutive blind source separation methods and deep learning techniques for neural decoding. *IEEE Signal Processing Magazine* **38** (2021), 103–118.

[124] Holobar, A.; Minetto, M. A.; Botter, A.; Negro, F. & Farina, D.: Experimental analysis of accuracy in the identification of motor unit spike trains from high-density surface EMG. *IEEE Transactions on Neural Systems and Rehabilitation Engineering* **18** (2010), 221–229.

[125] Holobar, A. & Zazula, D.: Multichannel blind source separation using convolution kernel compensation. *IEEE Transactions on Signal Processing* **55** (2007), 4487–4496.

[126] Hoyer, P. O.: Non-negative matrix factorization with sparseness constraints. *Journal of machine learning research* **5** (2004).

[127] Hug, F.; Avrillon, S.; Ibáñez, J. & Farina, D.: Common synaptic input, synergies and size principle: Control of spinal motor neurons for movement generation. *The Journal of Physiology* **601** (2023), 11–20.

[128] Huijing, P. A.: Muscle as a collagen fiber reinforced composite: a review of force transmission in muscle and whole limb. *Journal of biomechanics* **32** (1999), 329–345.

[129] Hurley, N. & Rickard, S.: Comparing measures of sparsity. *IEEE Transactions on Information Theory* **55** (2009), 4723–4741.

[130] Huxley, A. F.: Muscle structure and theories of contraction. *Progress in biophysics and biophysical chemistry* (1957).

[131] Huxley, A. F. & Niedergerke, R.: Structural changes in muscle during contraction: interference microscopy of living muscle fibres. *Nature* **173** (1954), 971.

[132] Huxley, H. & Hanson, J.: Changes in the cross-striations of muscle during contraction and stretch and their structural interpretation. *Acta Physiol. Scani* **6** (1954), 123.

[133] Huxley, H. E. & Hanson, J.: Changes in the cross-striations of muscle during contraction and stretch and their structural interpretation. *Nature* **173** (1954), 973–976.

[134] Hyvärinen, A. & Oja, E.: Independent component analysis: algorithms and applications. *Neural networks* **13** (2000), 411–430.

[135] Iyer, S. R.; Shah, S. B. & Lovering, R. M.: The neuromuscular junction: Roles in aging and neuromuscular disease. *International Journal of Molecular Sciences* **22** (2021), 8058.

[136] Kandel, E. R.; Schwartz, J. H.; Jessell, T. M.; Siegelbaum, S.; Hudspeth, A. J.; Mack, S. et al.: *Principles of neural science*, vol. 4. McGraw-hill New York 2000.

[137] Kauppinen, P.; Hyttinen, J.; Heinonen, T. & Malmivuo, J.: Detailed model of the thorax as a volume conductor based on the visible human man data. *Journal of medical engineering & technology* **22** (1998), 126–133.

[138] Keener, J. & Sneyd, J.: *Mathematical physiology II: Cellular physiology*, vol. 2. Springer 2009, second edn.

[139] Kirchhoff, G.: Über die Auflösung der Gleichungen, auf welche man bei der Untersuchung der linearen Vertheilung galvanischer Ströme geführt wird. *Annalen der Physik* **148** (1847), 497–508.

[140] Klotz, T.; Gizzi, L. & Röhrle, O.: Investigating the spatial resolution of EMG and MMG based on a systemic multi-scale model. *Biomechanics and Modeling in Mechanobiology* (2022), 1–15.

[141] Klotz, T.; Gizzi, L.; Yavuz, U. & Röhrle, O.: Modelling the electrical activity of skeletal muscle tissue using a multi-domain approach. *Biomechanics and Modeling in Mechanobiology* **19** (2020), 335–349.

[142] Klotz, T.; Lehmann, L.; Negro, F. & Röhrle, O.: High-density magnetomyography is superior to high-density surface electromyography for motor unit decomposition: a simulation study. *Journal of Neural Engineering* **20** (2023), 046022.

[143] Körber, R.; Storm, J.-H.; Seton, H.; Mäkelä, J. P.; Paetau, R.; Parkkonen, L.; Pfeiffer, C.; Riaz, B.; Schneiderman, J. F.; Dong, H. et al.: SQUIDs in biomagnetism: a roadmap towards improved healthcare. *Superconductor Science and Technology* **29** (2016), 113001.

[144] Krizhevsky, A.; Hinton, G. et al.: Learning multiple layers of features from tiny images (2009).

[145] Lafortune, P.; Arís, R.; Vázquez, M. & Houzeaux, G.: Coupled electromechanical model of the heart: parallel finite element formulation. *International journal for numerical methods in biomedical engineering* **28** (2012), 72–86.

[146] Lamminen, A. E.: Magnetic resonance imaging of primary skeletal muscle diseases: patterns of distribution and severity of involvement. *The British journal of radiology* **63** (1990), 946–950.

[147] Lateva, Z. C.; McGill, K. C. & Burgar, C. G.: Anatomical and electrophysiological determinants of the human thenar compound muscle action potential. *Muscle & Nerve: Official Journal of the American Association of Electrodiagnostic Medicine* **19** (1996), 1457–1468.

[148] LeVeque, R. J.: *Finite difference methods for ordinary and partial differential equations: steady-state and time-dependent problems*. SIAM 2007.

[149] Liddell, E. G. T. & Sherrington, C. S.: Recruitment and some other features of reflex inhibition. *Proceedings of the Royal Society of London. Series B, Containing Papers of a Biological Character* **97** (1925), 488–518.

[150] Lieber, R. L.: *Skeletal muscle structure, function, and plasticity*. Lippincott Williams & Wilkins 2002.

[151] Lieber, R. L.: Can we just forget about pennation angle? *Journal of Biomechanics* **132** (2022), 110954.

[152] Liu, Y.; Ning, Y.; He, J.; Li, S.; Zhou, P. & Zhang, Y.: Internal muscle activity imaging from multi-channel surface EMG recordings: a validation study. In *2014 36th Annual International Conference of the IEEE Engineering in Medicine and Biology Society*, IEEE 2014, pp. 3559–3561.

[153] Liu, Y.; Ning, Y.; Li, S.; Zhou, P.; Rymer, W. Z. & Zhang, Y.: Three-dimensional innervation zone imaging from multi-channel surface EMG recordings. *International journal of neural systems* **25** (2015), 1550024.

[154] Llinás, R. R.; Ustinin, M.; Rykunov, S.; Walton, K. D.; Rabello, G. M.; Garcia, J.; Boyko, A. & Sychev, V.: Noninvasive muscle activity imaging using magnetography. *Proceedings of the National Academy of Sciences* **117** (2020), 4942–4947.

[155] Lloyd, C. M.; Halstead, M. D. & Nielsen, P. F.: Cellml: its future, present and past. *Progress in Biophysics and Molecular Biology* **85** (2004), 433 – 450, ISSN 0079-6107, modelling Cellular and Tissue Function.

[156] Lloyd, D. G. & Besier, T. F.: An EMG-driven musculoskeletal model to estimate muscle forces and knee joint moments in vivo. *Journal of biomechanics* **36** (2003), 765–776.

[157] Lloyd, S.: Least squares quantization in PCM. *IEEE transactions on information theory* **28** (1982), 129–137.

[158] Lowery, M. M.; Stoykov, N. S.; Dewald, P. A. & Kuiken, T. A.: Volume conduction in an anatomically based surface EMG model. *IEEE Transactions on Biomedical Engineering* **51** (2004), 2138–2147.

[159] Lowery, M. M.; Stoykov, N. S.; Taflove, A. & Kuiken, T. A.: A multiple-layer finite-element model of the surface EMG signal. *IEEE Transactions on Biomedical Engineering* **49** (2002), 446–454.

[160] MacIntosh, R., B.; Gardiner, F., P. & McComas, J., A.: *Skeletal muscle: Form and function*. Human Kinetics 2006, second edn.

[161] MacKinnon, R.: Potassium channels. *FEBS letters* **555** (2003), 62–65.

[162] Maier, B. & Schulte, M.: Mesh generation and multi-scale simulation of a contracting muscle–tendon complex. *Journal of Computational Science* **59** (2022), 101559.

[163] Malmivuo, J.; Plonsey, R. et al.: *Bioelectromagnetism: principles and applications of bioelectric and biomagnetic fields*. Oxford University Press, USA 1995.

[164] Marquetand, J.; Middelmann, T.; Dax, J.; Baek, S.; Sometti, D.; Grimm, A.; Lerche, H.; Martin, P.; Kronlage, C.; Siegel, M. et al.: Optically pumped magnetometers reveal fasciculations non-invasively. *Clinical Neurophysiology* **132** (2021), 2681–2684.

[165] Maruyama, K.: Connectin, an elastic protein from myofibrils. *The Journal of Biochemistry* **80** (1976), 405–407.

[166] Maruyama, K.; Matsubara, S.; Natori, R.; Nonomura, Y.; Kimura, S.; Ohashi, K.; Murakami, F.; Handa, S. & Eguchi, G.: Connectin, an elastic protein of muscle. *The Journal of Biochemistry* **82** (1977), 317–337.

[167] Matthews, P.: Relationship of firing intervals of human motor units to the trajectory of post-spike after-hyperpolarization and synaptic noise. *The Journal of physiology* **492** (1996), 597–628.

[168] Maxwell, J. C.: On physical lines of force: Part I - The theory of molecular vortices applied to magnetic phenomena. *The London, Edinburgh, and Dublin Philosophical Magazine and Journal of Science* **21** (1861), 161–175.

[169] Maxwell, J. C.: On physical lines of force: Part II - The theory of molecular vortices applied to electric currents. *The London, Edinburgh, and Dublin Philosophical Magazine and Journal of Science* **21** (1861), 338–348.

[170] Maxwell, J. C.: On physical lines of force: Part III - The theory of molecular vortices applied to statical electricity. *The London, Edinburgh, and Dublin Philosophical Magazine and Journal of Science* **23** (1862), 12–24.

[171] Maxwell, J. C.: On physical lines of force: Part IV - The theory of molecular vortices applied to the action of magnetism on polarized light. *The London, Edinburgh, and Dublin Philosophical Magazine and Journal of Science* **23** (1862), 85–95.

[172] McGill, K. C. & Lateva, Z. C.: A model of the muscle-fiber intracellular action potential waveform, including the slow repolarization phase. *IEEE transactions on biomedical engineering* **48** (2001), 1480–1483.

[173] Mercuri, E.; Pichiecchio, A.; Allsop, J.; Messina, S.; Pane, M. & Muntoni, F.: Muscle MRI in inherited neuromuscular disorders: past, present, and future. *Journal of Magnetic Resonance Imaging: An Official Journal of the International Society for Magnetic Resonance in Medicine* **25** (2007), 433–440.

[174] Merletti, R. & Farina, D.: Analysis of intramuscular electromyogram signals. *Philosophical Transactions of the Royal Society A: Mathematical, Physical and Engineering Sciences* **367** (2009), 357–368.

[175] Merletti, R. & Farina, D.: *Surface electromyography: physiology, engineering, and applications*. John Wiley & Sons 2016.

[176] Merletti, R.; Roy, S. H.; Kupa, E.; Roatta, S. & Granata, A.: Modeling of surface myoelectric signals. II. Model-based signal interpretation. *IEEE Transactions on biomedical engineering* **46** (1999), 821–829.

[177] Merletti, R.; Vieira, T. M. & Farina, D.: *Techniques for Information Extraction from the Surface EMG Signal: High-Density Surface EMG*, John Wiley & Sons, Ltd 2016, chap. 5. ISBN 9781119082934, pp. 126–157.

[178] Mesin, L.: Analytical generation model of surface electromyogram for multi-layer volume conductors. *Modelling in Medicine and Biology VI, WIT* **8** (2005), 95–110.

[179] Mesin, L.: Volume conductor models in surface electromyography: Computational techniques. *Computers in Biology and Medicine* **43** (2013), 942 – 952, ISSN 0010-4825.

[180] Mesin, L.: Real time identification of active regions in muscles from high density surface electromyogram. *Computers in biology and medicine* **56** (2015), 37–50.

[181] Mesin, L.; Joubert, M.; Hanekom, T.; Merletti, R. & Farina, D.: A finite element model for describing the effect of muscle shortening on surface EMG. *IEEE Transactions on Biomedical Engineering* **53** (2006), 693–600.

[182] Miller, W. T. & Geselowitz, D. B.: Simulation studies of the electrocardiogram. I. The normal heart. *Circulation Research* **43** (1978), 301–315, ISSN 0009-7330.

[183] Mirvis, D. M. & Goldberger, A. L.: Electrocardiography. *Heart disease* **1** (2001), 82–128.

[184] Monti, R. J.; Roy, R. R.; Hodgson, J. A. & Edgerton, V. R.: Transmission of forces within mammalian skeletal muscles. *Journal of biomechanics* **32** (1999), 371–380.

[185] Mordhorst, M.; Heidlauf, T. & Röhrle, O.: Predicting electromyographic signals under realistic conditions using a multiscale chemo-electro-mechanical finite element model. *Interface Focus* **5** (2015), 1–11.

[186] Muceli, S.; Poppendieck, W.; Holobar, A.; Gandevia, S.; Liebetanz, D. & Farina, D.: Blind identification of the spinal cord output in humans with high-density electrode arrays implanted in muscles. *Science Advances* **8** (2022), eabo5040.

[187] Muceli, S.; Poppendieck, W.; Negro, F.; Yoshida, K.; Hoffmann, K. P.; Butler, J. E.; Gandevia, S. C. & Farina, D.: Accurate and representative decoding of the neural drive to muscles in humans with multi-channel intramuscular thin-film electrodes. *The Journal of physiology* **593** (2015), 3789–3804.

[188] Murzin, D.; Mapps, D. J.; Levada, K.; Belyaev, V.; Omelyanchik, A.; Panina, L. & Rodionova, V.: Ultrasensitive magnetic field sensors for biomedical applications. *Sensors* **20** (2020), 1569.

[189] Nakagawa, S.; Maeda, S. & Tsukihara, T.: Structural and functional studies of gap junction channels. *Current opinion in structural biology* **20** (2010), 423–430.

[190] Nandedkar, S. et al.: Simulation of single muscle fibre action potentials. *Medical and Biological Engineering and Computing* **21** (1983), 158–165.

[191] Naundorf, B.; Wolf, F. & Volgushev, M.: Unique features of action potential initiation in cortical neurons. *Nature* **440** (2006), 1060–1063.

[192] Nawab, S. H.; Chang, S.-S. & De Luca, C. J.: High-yield decomposition of surface EMG signals. *Clinical neurophysiology* **121** (2010), 1602–1615.

[193] Negro, F. & Farina, D.: Decorrelation of cortical inputs and motoneuron output. *Journal of Neurophysiology* **106** (2011), 2688–2697.

[194] Negro, F.; Muceli, S.; Castronovo, A. M.; Holobar, A. & Farina, D.: Multi-channel intramuscular and surface EMG decomposition by convolutive blind source separation. *Journal of neural engineering* **13** (2016), 026027.

[195] Neher, E. & Sakmann, B.: Single-channel currents recorded from membrane of denervated frog muscle fibres. *Nature* **260** (1976), 799–802.

[196] Nernst, W.: Zur Kinetik der in Lösung befindlichen Körper. *Zeitschrift für physikalische Chemie* **2** (1888), 613–637.

[197] Niederer, S. A. & Smith, N. P.: A mathematical model of the slow force response to stretch in rat ventricular myocytes. *Biophysical journal* **92** (2007), 4030–4044.

[198] Niedermeyer, E. & da Silva, F. L.: *Electroencephalography: basic principles, clinical applications, and related fields*. Lippincott Williams & Wilkins 2005.

[199] Nielsen, B. F.; Ruud, T. S.; Lines, G. T. & Tveito, A.: Optimal monodomain approximations of the bidomain equations. *Applied Mathematics and Computation* **184** (2007), 276 – 290, ISSN 0096-3003.

[200] Noble, D.; Garny, A. & Noble, P. J.: How the Hodgkin–Huxley equations inspired the cardiac physiome project. *The Journal of physiology* **590** (2012), 2613–2628.

[201] Noble, D.; Varghese, A.; Kohl, P. & Noble, P.: Improved guinea-pig ventricular cell model incorporating a diadic space, IKr and IKs, and length-and tension-dependent processes. *The Canadian journal of cardiology* **14** (1998), 123–134.

[202] Noda, M.; Shimizu, S.; Tanabe, T.; Takai, T.; Kayano, T.; Ikeda, T.; Takahashi, H.; Nakayama, H.; Kanaoka, Y.; Minamino, N. et al.: Primary structure of electrophorus electricus sodium channel deduced from cdna sequence. *Nature* **312** (1984), 121–127.

[203] de Oliveira, D. S.; Casolo, A.; Balshaw, T. G.; Maeo, S.; Lanza, M. B.; Martin, N. R.; Maffulli, N.; Kinfe, T. M.; Eskofier, B.; Folland, J. P. et al.: Neural decoding from surface high-density EMG signals: influence of anatomy and synchronization on the number of identified motor units. *Journal of Neural Engineering* (2022).

[204] Oostenveld, R.; Fries, P.; Maris, E. & Schoffelen, J.-M.: Fieldtrip: open source software for advanced analysis of MEG, EEG, and invasive electrophysiological data. *Computational intelligence and neuroscience* **2011** (2011).

[205] Osborne, J.; Orton, J.; Alem, O. & Shah, V.: Fully integrated standalone zero field optically pumped magnetometer for biomagnetism. In *Steep dispersion engineering and opto-atomic precision metrology XI*, SPIE 2018, vol. 10548, pp. 89–95.

[206] Oschman, J. L.: Clinical aspects of biological fields: an introduction for health care professionals. *Journal of Bodywork and Movement Therapies* **6** (2002), 117–125.

[207] Parker, K. K. & Wikswo, J.: A model of the magnetic fields created by single motor unit compound action potentials in skeletal muscle. *IEEE transactions on biomedical engineering* **44** (1997), 948–957.

[208] Person, R. & Kudina, L.: Discharge frequency and discharge pattern of human motor units during voluntary contraction of muscle. *Electroencephalography and clinical neurophysiology* **32** (1972), 471–483.

[209] Pillen, S.; Arts, I. M. & Zwarts, M. J.: Muscle ultrasound in neuromuscular disorders. *Muscle & Nerve: Official Journal of the American Association of Electrodiagnostic Medicine* **37** (2008), 679–693.

[210] Pinsky, P. F. & Rinzel, J.: Intrinsic and network rhythmogenesis in a reduced traub model for CA3 neurons. *Journal of computational neuroscience* **1** (1994), 39–60.

[211] Plonsey, R.: The active fiber in a volume conductor. *IEEE transactions on biomedical engineering* (1974), 371–381.

[212] Plonsey, R. & Barr, R. C.: *Bioelectricity: A quantitative approach*. Springer 2007.

[213] Powers, R. K.; El Basiouny, S. M.; Rymer, W. Z. & Heckman, C. J.: Contribution of intrinsic properties and synaptic inputs to motoneuron discharge patterns: a simulation study. *Journal of neurophysiology* **107** (2012), 808–823.

[214] Pullan, A. J.; Buist, M. L. & Cheng, L. K.: *Mathematically modelling the electrical activity of the heart: From cell to body surface and back again*. World Scientific Publishing Company, Singapore 2005.

[215] Qu, Z. & Garfinkel, A.: An advanced algorithm for solving partial differential equation in cardiac conduction. *IEEE Transactions on Biomedical Engineering* **46** (1999), 1166–1168.

[216] Raghavan, M.; Fee, D. & Barkhaus, P. E.: Generation and propagation of the action potential. *Handbook of clinical neurology* **160** (2019), 3–22.

[217] Reincke, M.: Magnetomyographie mit dem SQUID – Magnetomyography with the SQUID. *Biomedical Engineering – Biomedizinische Technik* **38** (1993), 276–281, URL `https://doi.org/10.1515/bmte.1993.38.11.276`.

[218] Rios, E. & Brum, G.: Involvement of dihydropyridine receptors in excitation–contraction coupling in skeletal muscle. *Nature* **325** (1987), 717–720.

[219] Roeleveld, K.; Blok, J.; Stegeman, D. & Van Oosterom, A.: Volume conduction models for surface EMG; confrontation with measurements. *Journal of Electromyography and Kinesiology* **7** (1997), 221–232.

[220] Roeleveld, K.; Stegeman, D.; Vingerhoets, H. & Oosterom, A. v.: Motor unit potential contribution to surface electromyography. *Acta physiologica scandinavica* **160** (1997), 175–183.

[221] Röhrle, O.; Davidson, J. B. & Pullan, A. J.: A physiologically based, multi-scale model of skeletal muscle structure and function. *Frontiers in Physiology* **3** (2012), 1–14.

[222] Röhrle, O.; Yavuz, U.; Klotz, T.; Negro, F. & Heidlauf, T.: Multiscale modelling of the neuromuscular system: coupling neurophysiology and skeletal muscle mechanics. *Wiley Interdisciplinary Reviews: Systems Biology and Medicine* (2019).

[223] Rosenfalck, P.: Intra- and extracellular potential fields of active nerve and muscle fibres. *Acta Phisiologica Scandinavica* **321** (1969).

[224] Rossi, A. E. & Dirksen, R. T.: Sarcoplasmic reticulum: the dynamic calcium governor of muscle. *Muscle & Nerve: Official Journal of the American Association of Electrodiagnostic Medicine* **33** (2006), 715–731.

[225] Roth, B. J. & Wikswo Jr, J. P.: The magnetic field of a single axon. a comparison of theory and experiment. *Biophysical journal* **48** (1985), 93–109.

[226] Rubin, D. I.: Chapter 17 - normal and abnormal spontaneous activity. In Levin, K. H. & Chauvel, P. (eds.): *Clinical Neurophysiology: Basis and Technical Aspects*. Elsevier 2019, vol. 160 of *Handbook of Clinical Neurology*, pp. 257–279.

[227] Rush, S.; Abildskov, J. & McFee, R.: Resistivity of body tissues at low frequencies. *Circulation research* **12** (1963), 40–50.

[228] Rush, S. & Driscoll, D. A.: EEG electrode sensitivity – an application of reciprocity. *IEEE transactions on biomedical engineering* (1969), 15–22.

[229] Saad, Y. & Schultz, M. H.: GMRES: A generalized minimal residual algorithm for solving nonsymmetric linear systems. *SIAM Journal on Scientific and Statistical Computing* **7** (1986), 856–869.

[230] Saini, H.; Klotz, T. & Röhrle, O.: Modelling motor units in 3D: influence on muscle contraction and joint force via a proof of concept simulation. *Biomechanics and Modeling in Mechanobiology* **22** (2023), 593–610.

[231] Sander, T.; Jodko-Władzińska, A.; Hartwig, S.; Brühl, R. & Middelmann, T.: Optically pumped magnetometers enable a new level of biomagnetic measurements. *Advanced Optical Technologies* **9** (2020), 247–251.

[232] Sandow, A.: Excitation-contraction coupling in muscular response. *The Yale journal of biology and medicine* **25** (1952), 176.

[233] Schirhagl, R.; Chang, K.; Loretz, M. & Degen, C. L.: Nitrogen-vacancy centers in diamond: nanoscale sensors for physics and biology. *Annu. Rev. Phys. Chem* **65** (2014), 83–105.

[234] Schmid, L.; Klotz, T.; Siebert, T. & Röhrle, O.: Characterization of electromechanical delay based on a biophysical multi-scale skeletal muscle model. *Frontiers in Physiology* **10** (2019), 1 – 13.

[235] Sherrington, C. S.: Remarks on some aspects of reflex inhibition. *Proceedings of the Royal Society of London. Series B, Containing Papers of a Biological Character* **97** (1925), 519–545.

[236] Sherrington, C. S.: Ferrier lecture: Some functional problems attaching to convergence. *Proceedings of the royal society of London. Series B, Containing Papers of a Biological Character* **105** (1929), 332–362.

[237] Shorten, P. R.; O'Callaghan, P.; Davidson, J. B. & Soboleva, T. K.: A mathematical model of fatigue in skeletal muscle force contraction. *Journal of muscle research and cell motility* **28** (2007), 293–313.

[238] Sigworth, F. J. & Neher, E.: Single Na+ channel currents observed in cultured rat muscle cells. *Nature* **287** (1980), 447–449.

[239] Skou, J. C.: The identification of the sodium–potassium pump (Nobel lecture). *Angewandte Chemie International Edition* **37** (1998), 2320–2328.

[240] Solomonow, M.; Baratta, R.; Bernardi, M.; Zhou, B.; Lu, Y.; Zhu, M. & Acierno, S.: Surface and wire EMG crosstalk in neighbouring muscles. *Journal of Electromyography and Kinesiology* **4** (1994), 131–142.

[241] Stålberg, E. & Fawcett, P.: Macro EMG in healthy subjects of different ages. *Journal of Neurology, Neurosurgery & Psychiatry* **45** (1982), 870–878.

[242] Stegeman, D. F.; Blok, J. H.; Hermens, H. J. & Roeleveld, K.: Surface EMG models: properties and applications. *Journal of Electromyography and Kinesiology* **10** (2000), 313–326.

[243] Strang, G.: On the construction and comparison of difference schemes. *SIAM journal on numerical analysis* **5** (1968), 506–517.

[244] Street, S. F.: Lateral transmission of tension in frog myofibers: a myofibrillar network and transverse cytoskeletal connections are possible transmitters. *Journal of cellular physiology* **114** (1983), 346–364.

[245] Sundnes, J.; Lines, G. T. & Tveito, A.: An operator splitting method for solving the bidomain equations coupled to a volume conductor model for the torso. *Mathematical Biosciences* **194** (2005), 233–248.

[246] Sundnes, J.; Nielsen, B. F.; Mardal, K.; Cai, X.; Lines, G. T. & Tveito, A.: On the computational complexity of the bidomain and the monodomain models of electrophysiology. *Annals of Biomedical Engineering* **34** (2006), 1088–1097.

[247] Supek, S. & Aine, C. J.: *Magnetoencephalography*. Springer 2016.

[248] Talib, I.; Sundaraj, K.; Lam, C. K.; Hussain, J.; Ali, M. et al.: A review on crosstalk in myographic signals. *European journal of applied physiology* **119** (2019), 9–28.

[249] Tatum IV, W. O.: *Handbook of EEG interpretation*. Springer Publishing Company 2021.

[250] Taylor, C. A.; Kopicko, B. H.; Negro, F. & Thompson, C. K.: Sex differences in the detection of motor unit action potentials identified using high-density surface electromyography. *Journal of Electromyography and Kinesiology* **65** (2022), 102675.

[251] Thompson, R. F.: *The brain: An introduction to neuroscience.* WH Freeman/Times Books/Henry Holt & Co 1985.

[252] Trayanova, N.; Constantino, J.; Ashihara, T. & Plank, G.: Modeling defibrillation of the heart: approaches and insights. *IEEE reviews in biomedical engineering* **4** (2011), 89–102.

[253] Trayanova, N.; Plank, G. & Rodríguez, B.: What have we learned from mathematical models of defibrillation and postshock arrhythmogenesis? Application of bidomain simulations. *Heart Rhythm* **3** (2006), 1232–1235.

[254] Tung, L.: *A bi-domain model for describing ischemic myocardial DC potentials.* Dissertation, Massachusetts Institute of Technology (1978).

[255] Van Den Doel, K.; Ascher, U. M. & Pai, D. K.: Source localization in electromyography using the inverse potential problem. *Inverse Problems* **27** (2011), 025008.

[256] Van Egeraat, J.; Friedman, R. & Wikswo Jr, J.: Magnetic field of a single muscle fiber. first measurements and a core conductor model. *Biophysical journal* **57** (1990), 663–667.

[257] Vorwerk, J.; Cho, J.-H.; Rampp, S.; Hamer, H.; Knösche, T. R. & Wolters, C. H.: A guideline for head volume conductor modeling in EEG and MEG. *NeuroImage* **100** (2014), 590–607.

[258] Vujaklija, I.: Novel control strategies for upper limb prosthetics. In *International Conference on NeuroRehabilitation*, Springer 2018, pp. 171–174.

[259] Wallinga, W.; Meijer, S. L.; Alberink, M. J.; Vliek, M.; Wienk, E. D. & Ypey, D. L.: Modelling action potentials and membrane currents of mammalian skeletal muscle fibres in coherence with potassium concentration changes in the T-tubular system. *European Biophysics Journal* **28** (1999), 317–329.

[260] Wang, K.; McClure, J. & Tu, A.: Titin: major myofibrillar components of striated muscle. *Proceedings of the National Academy of Sciences* **76** (1979), 3698–3702.

[261] Wang, X.-J.: Calcium coding and adaptive temporal computation in cortical pyramidal neurons. *Journal of Neurophysiology* (1998).

[262] Waxman, S. G.: Determinants of conduction velocity in myelinated nerve fibers. *Muscle & Nerve: Official Journal of the American Association of Electrodiagnostic Medicine* **3** (1980), 141–150.

[263] Whiteley, J. P.: An efficient numerical technique for the solution of the monodomain and bidomain equations. *IEEE Transactions on Biomedical Engineering* **53** (2006), 2139–2147.

[264] Woosley, J. K.; Roth, B. J. & Wikswo Jr, J. P.: The magnetic field of a single axon: A volume conductor model. *Mathematical Biosciences* **76** (1985), 1–36.

[265] Yu, F. H. & Catterall, W. A.: Overview of the voltage-gated sodium channel family. *Genome biology* **4** (2003), 1–7.

[266] Zajac, F. E.: Muscle and tendon: properties, models, scaling, and application to biomechanics and motor control. *Critical Reviews in Biomedical Engineering* **17** (1989), 359–411.

[267] Zhang, C.; Zhang, J.; Widmann, M.; Benke, M.; Kübler, M.; Dasari, D.; Klotz, T.; Gizzi, L.; Röhrle, O.; Brenner, P. et al.: Optimizing NV magnetometry for magnetoneurography and magnetomyography applications. *Frontiers in Neuroscience* **16** (2022), 2340.

[268] Zhang, C.; Zhang, J.; Widmann, M.; Benke, M.; Kübler, M.; Dasari, D.; Klotz, T.; Gizzi, L.; Röhrle, O.; Brenner, P. et al.: Optimizing nv magnetometry for magnetoneurography and magnetomyography applications. *Frontiers in Neuroscience* **16** (2022).

[269] Zienkiewicz, O. C.; Taylor, R. L. & Zhu, J. Z.: *The finite element method: its basis and fundamentals*. Elsevier 2005.

[270] Zuo, S.; Heidari, H.; Farina, D. & Nazarpour, K.: Miniaturized magnetic sensors for implantable magnetomyography. *Advanced Materials Technologies* **5** (2020), 2000185.

[271] Zuo, S.; Nazarpour, K.; Böhnert, T.; Paz, E.; Freitas, P.; Ferreira, R. & Heidari, H.: Integrated pico-tesla resolution magnetoresistive sensors for miniaturised magnetomyography. In *2020 42nd Annual International Conference of the IEEE Engineering in Medicine & Biology Society (EMBC)*, IEEE 2020, pp. 3415–3419.

[272] Zuo, S.; Nazarpour, K.; Farina, D.; Broser, P. & Heidari, H.: Modelling and analysis of magnetic fields from skeletal muscle for valuable physiological measurements. *arXiv preprint arXiv:2104.02036* (2021).

[273] Zuo, S.; Schmalz, J.; Özden, M.-Ö.; Gerken, M.; Su, J.; Niekiel, F.; Lofink, F.; Nazarpour, K. & Heidari, H.: Ultrasensitive magnetoelectric sensing system for pico-tesla magnetomyography. *IEEE Transactions on Biomedical Circuits and Systems* **14** (2020), 971–984.